CIRCULATION AND DYNAMICS ON THE NORTHEASTERN CHUKCHI SEA SHELF

By

Ying-Chih Fang, M.S.

A Dissertation Submitted in Partial Fulfillment of the Requirements

for the Degree of

Doctor of Philosophy

in

Oceanography

University of Alaska Fairbanks

December 2017

APPROVED:

Thomas J. Weingartner, Committee Chair
Peter Winsor, Committee Member
Zygmunt Kowalik, Committee Member
Andrew McDonnell, Committee Member
William J. Williams, Committee Member
Mark A. Johnson, Chair
    Department of Oceanography
S. Bradley Moran, Dean
    College of Fisheries and Ocean Sciences
Michael Castellini, *Dean of Graduate School*

Abstract

The circulation on the northeastern Chukchi Sea shelf is controlled by the poleward pressure gradient between the Pacific and Arctic Oceans. Local winds modulate the upper ocean and can rapidly alter the flow field. Present understanding of the circulation is largely based on subsurface measurements, but the response of near-surface currents to the slowly-varying secular pressure gradient and rapidly-varying local winds has not been addressed. I analyzed surface current data, extending more ~150 km offshore in the northeastern Chukchi Sea, collected from shore-based high-frequency radar systems (HFR) during the open water season. I find three wind-induced circulation regimes. Two of these are related to strong northeasterly winds when wind speeds approach or exceed 6 m s^{-1} and the third results from infrequent northwesterly winds at $>$~6 m s^{-1}. I find two dynamically different regions separated along ~71.5°N associated with hydrographic changes. North of 71.5°N the water column is strongly stratified due to cold and dilute ice meltwaters, whereas the water column to the south is much less stratified. These differences are reflected in the current response to the winds. I also adapted and refined an HFR data processing technique and developed an economical way to assess HFR-derived data quality, which is beneficial when using HFR data collected from networks having suboptimal coverage.

I investigated the poorly understood circulation around Hanna Shoal. North of the Shoal there is a zonal gradient in the thermohaline and flow fields. The eastern side of the Shoal is strongly stratified year-round and vertically sheared unlike the western side, where the flow is steadily northeastward over the water column. Dense bottom waters flow clockwise around Hanna Shoal, but zonal convergence is implied in the upper water column north of the Shoal. The circulation is influenced by the distribution of late summer sea ice and by clockwise-propagating topographic waves.

Dedication Page

To Dr. Tswen-Yung Tang

As my friend, teacher, and advisor, you should be here. Our last goodbye was never said. I hope one day I will see you on the other side of the ocean. We can watch the New York Yankees' game with Tom together, drinking the great Alaskan Amber.

Table of Content

List of Figures

List of Tables

List of Appendices

Acknowledgements

I am so fortunate to have had Tom Weingartner as an advisor for my PhD life at UAF. Not only does he have a heart made of baseball fever like me, but also a concentrated and passionate mind for the physical oceanography. This is something I need to develop more deeply in the future, and I am thankful I can work with him so closely. Committee members Peter Winsor, Zygmunt Kowalik, Bill Williams, and Andrew McDonnell contributed valuable input deepening my understanding of the ocean. I want to especially thank Peter Winsor for his unique insights when I began my research at UAF. The question Peter asked that day significantly awakened something inside my mind. In terms of baseball terminology, I would say this led me to a change of mindset from amateur to professional.

Other faculty members in the physical oceanography group, Mark Johnson, Seth Danielson, and Harper Simmons, always had an open door and willingness to share their knowledge with me. I want to thank Harper as the first person I met from CFOS, extending hospitality when I arrived in the middle of the Alaskan winter. I am also indebted to Rachel Potter and Hank Statscewich. Working in the field with them is a luxury because you have such experienced and intellectual people help you solve problems, which they never failed. I want to thank Liz Dobbins, Cayman Irvine, Chase Stoudt, Kate Hedstrom, Jim Kelly, and Brita Irving for their preparation and effort on data sets and fieldwork. This teamwork broadened my mind and facilitated my research.

I want to thank my office mate Dmitry Brazhnikov (Dima) for his patience sharing an office with me for the past six years. I learned so much from Dima, and it would be impossible for me to accomplish the number of tasks he did. One is lucky when both their advisor and office mate are much smarter than they are. Along with Dima, Jonathan Whitefield (Jona) should also be acknowledged. Without Jona, I may have been grounded in Fairbanks for a long time before I witnessed gorgeous Alaska. I want to thank Jona for his hospitality on many holidays, which made me feel so warm and welcome. Other graduate students Madeline Merck, Hanne Skattor, Jenna Walker, Sookmi Moon, Heather McEachen, Charlotte Whitefield, Steven Savard, Jen Questel, Tanja Schollmeier, Alex Ravelo, Kim Powell, and Imme Rutzen provided valuable feedback. I want to thank Kofan Lu letting me exchange thoughts using my familiar dialect and appreciate that she shared her educational experience with me.

General Introduction

Since Lieutenant Matthew F. Maury of the U.S. Navy wrote his *Physical Geography of The Sea* in 1855 with global maps of winds and sea surface drifts (Maury 1855); and U.S. Navy Commodore Matthew C. Perry and his crew mapped the *KuroSiwo* (nowadays Kuroshio) during his U.S.-Japan expedition in 1854 (Hayes 2001), oceanographers have striven to improve knowledge of the ocean circulation and its relationship to the winds. Although Maury had pointed out that there was a northward flow through Bering Strait, he did not realize this northward flow was propelled by a sea level height difference between the Pacific and Arctic Oceans (e.g., Stigebrandt 1984; Peacock and Laxon 2004), nor was he aware that local winds have a substantial influence on the regional circulation regime (Coachman et al. 1975). This dissertation addresses how the time-varying northward flow from Bering Strait is modified as it proceeds across the Chukchi Sea shelf. My investigation focuses on the circulation structure and its response to atmospheric forcing in the northeast Chukchi Sea, including the comparatively poorly surveyed region surrounding Hanna Shoal.

The Chukchi Sea is comprised of a large, shallow ($\leq$~50 m) continental shelf extending ~800 km meridional from Bering Strait with a similar zonal width along its northern edge. From long-term measurements, the Pacific inflow through Bering Strait is ~1 Sv (e.g., Woodgate et al. 2012). These northward-flowing Pacific waters exit the Chukchi shelf into the deep Arctic Ocean through three major pathways (Figure 0.1). Numerical simulations (Winsor and Chapman 2004; Spall 2007) and observations indicate that one pathway flows along the Alaskan coast (e.g., Paquette and Bourke 1974) and exits the shelf through Barrow Canyon (e.g., Mountain et al. 1976; Aagaard and Roach 1990), another branch flows through Herald Canyon (Woodgate et al. 2005; Pickart et al. 2010), and the third branch flows through the Central Channel (e.g., Weingartner et al. 2005) between Herald and Hanna shoals. The shallow water column and low zooplankton grazing rate (e.g., Sakshaug 2004) suggest that much of transported nutrients and particulate organic carbon advected with the Pacific inflow accumulates on the sea floor, where it sustains a rich benthic ecosystem (e.g., Grebmeier et al. 1988, 2006).

The annually recurring and seasonally-persistent sea ice cover largely modulates the Chukchi shelf by interacting with the local circulation system. During summer and fall, the three

flow pathways establish ice edge embayments (Martin and Drucker 1997; Weingartner et al. 2013; Wood et al. 2015). Moreover, formation of sea ice and wind-induced divergent ice movement make the Chukchi shelf an important location for the production of cold, saline, dense shelf waters essential in the maintenance of the Arctic cold halocline (e.g., Aagaard et al. 1981; Winsor and Björk 2000). The shelf sea ice also serves as an important habitat for marine mammals from which they forage upon the rich benthic food resources (e.g., Moore and Huntington 2008; Schonberg et al. 2014).

In response to greenhouse gas warming, ongoing sea ice reduction (e.g., Frey et al. 2015) is altering the Chukchi Sea to a new state in terms of many environmental parameters (Wood et al. 2015) such as wind fluctuations, sea ice persistence, and current pathways. These variations correspond to shifting patterns of biodiversity (Grebmeier 2012) and diminishing foraging habitats (Dunton et al. 2014). Additionally, the seasonal retreat and advance of sea ice varies interannually, which results in complicated regional biological responses (e.g., Day et al. 2013). The phasing and magnitude of the summer sea ice retreat appears to control how much near-surface cold, dilute meltwaters remain on the shelf through summer and fall (e.g., Weingartner et al. 2017) and greatly influences water column stratification. As will be shown in this dissertation, these interannual variations in sea ice fundamentally affect the dynamics controlling the local circulation.

In 2009, high-frequency (4–5 MHz) radar (HFR) systems were deployed on the Arctic Alaskan coast to study near-shore (≤~150 km) surface currents (~2 m depth, see Stewart and Joy 1974) during the open water seasons in the Chukchi Sea. This technology was pioneered first by Crombie (1955) who realized that reflected radar-emitted electromagnetic waves from the sea surface can be used to infer the phase propagation speeds of surface gravity waves based on the Doppler shift. Theoretical derivations and field tests of HFR verified the relationship between surface currents and the received Doppler shifted signals (Barrick et al. 1974; Stewart and Joy 1974; Barrick 1978). HFR subsequently evolved into a national wide surface current observing network with more than 100 operational HFR systems (Harlan et al. 2010) and continues to expand internationally. Drifting floats (e.g., Davis 1985) and satellite imagery (e.g., Emery et al. 1992) also provide near-shore surface currents but lack the temporal and spatial resolution of the HFR measurements. Such measurements are particularly important on the Chukchi Sea shelf

because the mean Pacific-Arctic pressure gradient that forces water northward over the shelf (and northeastward in the northeastern Chukchi Sea) is opposed by the mean northeasterly winds. Moored instruments have documented the subsurface current structure over portions of the Chukchi shelf (Weingartner et al. 2005; Woodgate et al. 2005). These show that the subsurface flow is a result of geostrophic adjustment to the rapidly varying (in time) pressure field established by wind stress convergence and divergence in conjunction with the more slowly-varying Pacific-Arctic pressure gradient. Subsurface sensors, however, are incapable of measuring the surface currents. Dynamically, the upper ocean currents respond to both pressure fields as well as the vertically divergent surface wind stress. Thus the question: Does the surface current field in the Chukchi Sea differ from the subsurface currents? HFR systems provide the opportunity to examine the time- and space-varying kinematical and dynamical structure of the surface circulation.

Successful application of HFR to the Chukchi shelf is somewhat problematic because the coastal locations of the HFR sites were dictated by power grid availability, and so the resultant radar coverage was not optimal from the sampling perspective. This problem led to a permanent data gap in the Chukchi HFR network and is the motivation of the first chapter. To address this issue I tested the applicability of a gap-filling procedure based on the optimal interpolation (OI) technique developed by Kim et al. (2007, 2008) to the Chukchi HFR network. My test focused on quality assessment of the resultant currents and an analysis of the errors associated with the technique. One result of this research was that it yielded a relatively simple and economical way to assess HFR-derived data quality, especially for those HFR networks lacking optimal site locations.

The second chapter applies the OI method to surface current observations from 2010–2014. The Chukchi Sea is a very dynamic environment, producing many different current patterns that change rapidly. Therefore a straightforward interpretation of the data becomes complicated with large, highly variable data sets. As a result, a novel data mining approach, Self-Organizing Maps (SOM) (Kohonen 2001), was used to analyze surface current data and study the co-variability between currents and winds. My application of the SOM technique yielded four circulation regimes. Two of these are quasi-steady and depend upon the strength of the northeasterly winds. A third is related to less frequently occurring northwesterly winds, while

the fourth is a transitional surface circulation pattern that arises in response to strengthening northeasterly winds. I found that there is a wind speed threshold for northeasterly or northwesterly winds which, once exceeded, results in changes to the local circulation regime, and I also address spatial variations in the surface current field and potential dynamic causes for these variations.

In the third chapter I analyzed subsurface current observations derived from 23 moorings that collected data from 2011–2014 near Hanna Shoal on the northeastern Chukchi shelf. This area of the shelf is of particular importance to the regional marine ecosystem and supports enhanced biological productivity (Grebmeier et al. 2015). Moreover, the shallow bathymetry can result in sea ice grounding atop the Shoal during winter (e.g., Grantz and Eittreim 1979). The grounded ice accumulates additional sea ice that drifts onto the Chukchi shelf from the Arctic basin. Consequently a considerable volume of thick, deformed ice accumulates throughout winter and then persists into summer or fall, well after ice has retreated elsewhere on the shelf (Weingartner et al. 2013, 2017; Wood et al. 2015). In winter the stagnant ice can permit latent heat polynya formation over or in the lee of the Shoal, which augments the winter production of cold, saline waters. In summer, the ice mass is a source of meltwaters to the shelf. The vertical juxtaposition of dense, saline winter waters with dilute summer meltwaters has a profound effect on the stratification of the shelf and the formation of fronts. I employed a number of time series analysis techniques to study the temporal and spatial variations of currents around Hanna Shoal proper and their response to winds. These patterns appear to be controlled fundamentally by interannual variations in sea ice retreat. Geographically, there is a west-east gradient in the thermohaline properties and flow fields on Hanna Shoal. My analyses suggest flow convergence on the northern side of Hanna Shoal, which may be important for shelf-basin exchange. Additionally, I have discussed the first documented topographic wave signal at the eastern side of Hanna Shoal. All together, these findings provide more insights of the physical oceanography on this portion of the Chukchi shelf and are essential for the future investigation in this area.
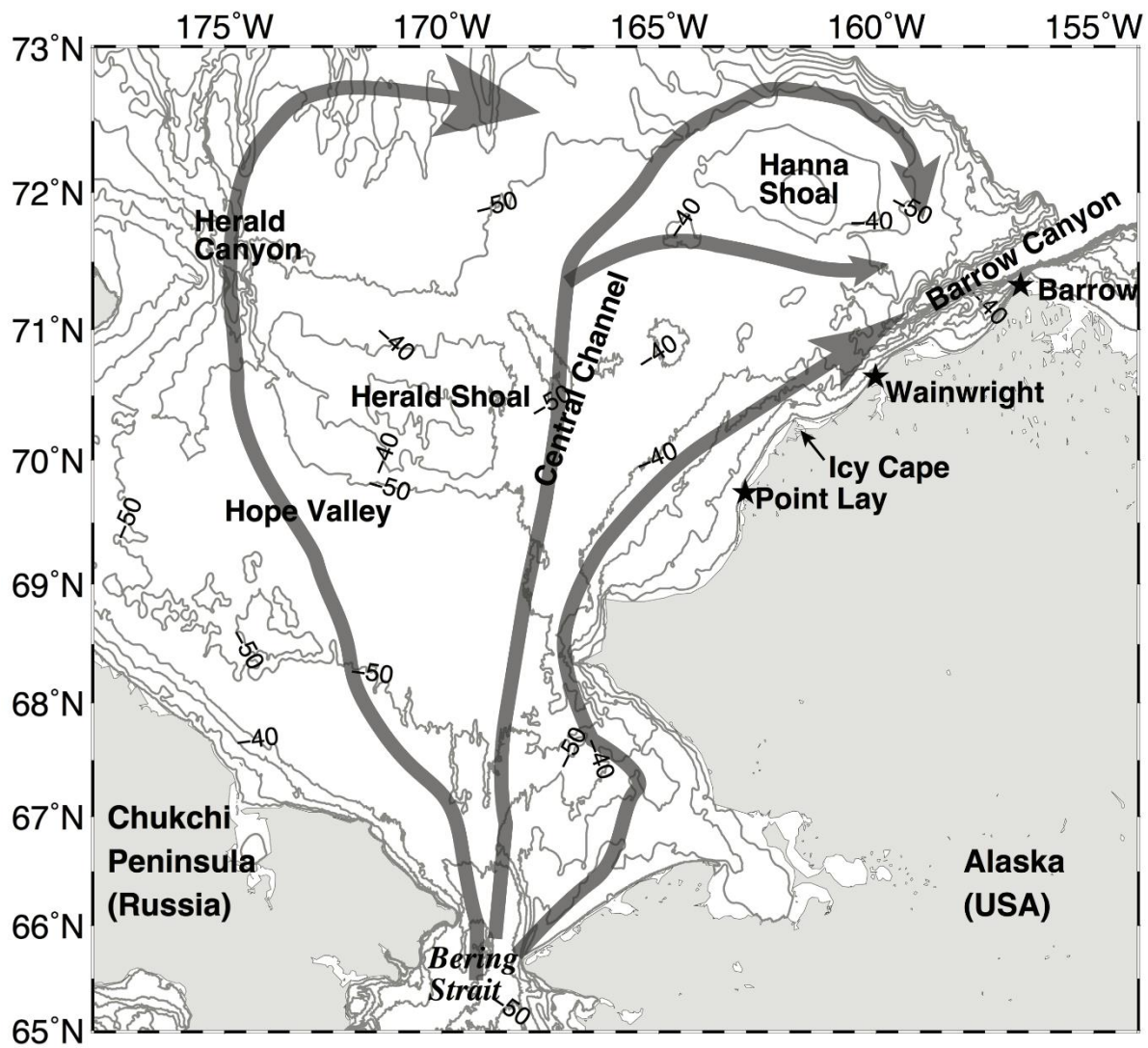
Figure 0.1. Map of the Chukchi Sea with place names. Gray arrows show schematic pathways of Pacific waters. Bathymetric contours are drawn from 10–100 m at 10-m intervals.

CHAPTER 1: Quality Assessment of HF Radar–Derived Surface Currents Using Optimal

Interpolation[1]

1.1 Abstract

We investigate the applicability of the optimal interpolation (OI) method proposed by Kim et al. for estimating ocean surface currents from high-frequency radar (HFR) in the northeastern Chukchi Sea, where HFR siting is dictated by power availability rather than optimal locations. Although the OI technique improves data coverage when compared to the conventional unweighted least-squares-fit (UWLS) method, biased solutions can emerge. We find the quality of the HFR velocity estimates derived by OI is controlled by three factors: 1) the number of available incorporating radials (AR), 2) the ratio of the incorporating radials from multiple contributing site locations (ROR or radar geometry), and 3) the positive definiteness (condition number; CN) of the correlation matrix. Operationally, ROR does not require knowledge of the angle covariance matrix used to compute the geometric dilution of precision (GDOP) in the UWLS method and can be computed before site selection to optimize coverage or after data processing to assess data quality when applying the OI method. The Kim et al. method is extended to examine sensitivities to data gaps in the radial distribution and the effects on OI estimates.

1.2 Introduction

Ocean surface currents can be mapped over broad areas from a shore-based high-frequency radar (HFR) array. In real-time applications, HFRs can support search and rescue missions, identify oil spill trajectories, and guide adaptive sampling. Each radar receives Doppler-shifted signals Bragg-scattered from surface gravity waves one half the wavelength of the transmitted radar wave (Crombie 1955). Because it is induced by the current upon which the surface gravity waves propagate, this Doppler shift is used to calculate surface velocity. The

---

velocity is then projected onto a spoke pattern originating from each HFR field site, resulting in a map of one-dimensional surface current measurements advancing or retreating from each site. Such quantities are referred to as the radial velocity components, **r,** or radials, where $\mathbf{r}(\mathbf{x}, t) = \mathbf{u}(\mathbf{x}, t) \times \hat{\mathbf{x}}_r$. The surface current vector $\mathbf{u}(\mathbf{x}, t) = (u, v)$ represents the east-west (u) and north-south (v) velocity components; $\mathbf{x} = (x, y)$ is the corresponding coordinate system; t is the time step when **r** is measured; and $\hat{\mathbf{x}}_r$ is a unit vector aligned from **x** to the location of the HFR. For a direction-finding HFR, such as the SeaSonde system manufactured by CODAR Ocean Sensors, **r** are measured in angular sectors divided by concentric rings originating from the HFR (Lipa and Barrick 1983; Gurgel 1994). Multiple HFR are required to resolve the two-dimensional **u**, estimated by incorporating all **r** within a specified search radius (d_o) surrounding **x**. Several methods have been designed to resolve **u** from HFR measurements. Among them, the unweighted least-squares-fit (UWLS) method is widely used throughout the HFR community and is the default method applied by SeaSonde processing software.

One quality assessment commonly used with UWLS method is the geometric dilution of precision error (GDOP) (Chapman et al. 1997, Barrick 2006). GDOP is computed by inverting the angle covariance matrix and is a function of the number of measurements available and the distance between HFR. For two 5 MHz SeaSonde systems having a range of ~180 km, the GDOP threshold excludes $\hat{\mathbf{x}}_r$ with intersecting angles between **r** of < 15°. Utilizing GDOP, optimal HFR site spacing is found to be ~76 km. If HFR spacing is non-optimal, the distribution of **u** will be reduced. One goal of this paper is to evaluate **u** under such circumstances.

In 2010 and 2011, three 5 MHz (25 kHz bandwidth) SeaSonde systems were deployed along the northwest Alaskan coast in the villages of Barrow, Wainwright, and Point Lay to map surface currents during the late July – early November ice-free season in the northeastern Chukchi Sea (Figure 1.1). This HFR array provided near real-time measurements of surface currents and yielded unprecedented data coverage in this region (henceforth, the radar mask).

The Chukchi HFR sites had limitations in that these were the only locations along this coast with an electrical grid. Thus optimal site spacing was not possible, and the HFR placement was dictated by power availability. The distance between each HFR site was ~150 km, nearly twice the optimal site spacing. Moreover, the coastline geometry of Icy Cape and Point Franklin

8

blocked signal propagation. In aggregate these limitations resulted in the radar mask being split into two regions separated by a persistent data gap north of Icy Cape (Figure 1.1).

Spurious **u** are often found near the boundary of the radar mask (Figure 1.1, orange circles) and are denoted by large velocities, veer relative to neighboring **u**, and occur in regions of high GDOP. Additionally, **r** may be noisy due to environmental conditions or ionospheric interference. Nightly reflections of the HFR signal from the ionosphere lower the signal-to-noise ratio in radar spectral returns at ranges of more than 90 km, thus reducing the effective range of each system (Teague 2001). Figure 1.2 shows the average HFR data returns per hour of day by examining return spectra following Fang et al. (2011). Data returns diminish for ~5 hours daily, typically between 0700 – 1100 UTC. Ionospheric interference is persistent along high-latitude coasts and is also encountered at lower-latitude HFR sites.

The UWLS method assumes infinite signal and unit error variances, such that each of the **r** incorporated into the estimate of **u** are treated identically. Thus, this approach is highly sensitive to outliers. To mitigate the influence of noise and enhance confidence in velocity estimates within the radar mask, we investigate the applicability of the optimal interpolation (OI) method (Kim et al. 2007, 2008) to the Chukchi Sea HFR array. Comparing OI and UWLS estimated **u**, we found that the magnitudes of the current vectors are similar in their spatial distributions, but in some portions of the radar mask, the directions of the UWLS- and OI-derived vectors differed noticeably from one another. We explore the reasons for these differences.

OI has been implemented in Southern California and the Mid-Atlantic Bight (Kim et al. 2007, 2008; Kohut et al. 2012). Kohut et al. (2012) evaluated the OI and UWLS methods by comparing **u** with *in situ* data. Their results, and those of Kim et al. (2008), indicate that OI-derived currents reduce noise and yield fewer spurious vector solutions than those obtained from the UWLS method. However, Kohut et al. (2012) only evaluated specific grid points within the radar mask, which, while showing favorable results, did not reveal potential limitations of the OI method.

This study is an attempt to better quantify the limitations of the OI method that, when understood, enhance the ability to analyze HFR datasets. Using a series of simulations designed

9

to assess the capabilities of the OI method, diagnose parameter selections, and provide insight on how to better interpret radar-estimated **u,** we find that the ratio of contributing **r** from each HFR site can serve as a proxy for the estimated data quality and can be used to optimize HFR site selection.

The paper is arranged as follows: Background information on HFR data acquisition and processing is discussed in Section 1.3. A brief review of the OI method developed by Kim et al. (2007, 2008) and its implementation are given in Section 1.4. Section 1.5 provides an assessment of the OI method. A discussion and summary complete the paper.

1.3 Ocean surface current observations in the northeastern Chukchi Sea

The shallow (~50 m) Chukchi Sea connects the Arctic and Pacific oceans via Bering Strait. The shelf circulation is forced by the large-scale pressure gradient between these two basins and is nominally northward and guided by the bathymetry (Winsor and Chapman 2004; Weingartner et al. 2005). Within the radar mask, flow typically includes the swift (~0.5–1.0 m s^{-1}) Alaskan Coastal Current (ACC), which is a coastal jet flowing northeastward within ~40 km of the coast between Wainwright and Barrow (Paquette and Bourke 1974). Over the shelf south of Hanna Shoal, flow is weaker and broader and transports central shelf waters eastward toward Wainwright and the head of Barrow Canyon (Figure 1.1). On average, the flow between Barrow Canyon and Hanna Shoal is very weak. Wind-forced reversals of the ACC and shelf flow are very common and may last for several days to weeks (Weingartner et al. 1999; Weingartner et al. 2005).

Our SeaSonde systems collected **r** at 30 minute intervals over an effective depth of ~2 m (Stewart and Joy 1974) and had a resolution in range and bearing of 6 km and 5°, respectively. All spectra acquired in a three-hour window were averaged to produce an hourly **r** file. Antennas were calibrated using a beam pattern measurement to improve the direction finding capability of the receive antenna in the local environment (Barrick and Lipa 1986). Subsequent to acquisition, cross spectra were visually inspected to ensure software parameters were optimized for locating Bragg peaks at each site throughout the field season. The **r** were further quality controlled by removing **r** >150 cm s^{-1}, **x** with less than 10% coverage, and velocities exceeding three standard

deviations from the temporal mean of each **x**. HFR_Progs (https://cencalarchive.org/~cocmpmb/COCMP-wiki/) was used to distribute **r** onto uniform grid points (Figure 1.3). If multiple contributing sites provide at least three available **r** in the d_o, these **r** are then used to estimate **u** through the UWLS and OI methods at each **x**. Every hour, ninety minutes of **r** before and after the cardinal hour are averaged to produce a map of **u** by each method. For the UWLS method, d_o is defined as 12 km; whereas the d_o for the OI method is 35 km, with this choice discussed in Section 1.4. In the UWLS procedure, choosing a d_o too large results in **r** far from the grid point of interest having a large influence on the estimated **u**. In the OI method **r** are weighted with respect to their distance from the grid point of the resulting **u** and thus utilize a larger d_o. These weighting schemes are a key difference between the two methods.

HFR data from 2010 (September–October) and 2011 (August – October) are used in this paper with the main analysis based on the former. The 2011 data are used to compute related parameters of the OI method for comparison purposes.

1.4 Optimal interpolation

1.4.1 Objective analysis

For HFR data, **u** and **r** have the following relationship:

$$\mathbf{r} = \mathbf{g}^T \mathbf{u} + \mathbf{n} \tag{1}$$

where **g** is the angle matrix ($\mathbf{g}(\mathbf{x}) = [\cos q \; \sin q]$, with q the bearing at **x** measured counterclockwise from east), and **n** is the error matrix. In the UWLS method, $\left(\mathbf{g}^T \mathbf{g}\right)^{-1}$ is the inverse of the angle covariance matrix, where superscripts "*T*" and "*-1*" denote the matrix transpose and inverse, respectively. The norm of $\left(\mathbf{g}^T \mathbf{g}\right)^{-1}$ (calculated within the HFR_Progs toolbox) is the GDOP. Based on the Gauss-Markov theorem, unknown **u** with minimum variance from observation **r** can be written as:

$$\mathbf{u} = \mathrm{cov}_{dm}^T \, \mathrm{cov}_{dd}^{-1} \, \mathbf{r} \tag{2}$$

11

where cov_{dm} is the covariance matrix between the $\mathbf{u}$ and $\mathbf{r}$, and cov_{dd} represents the covariance matrix among $\mathbf{r}$. Assuming that $\mathbf{r}$ and $\mathbf{n}$ and $\mathbf{u}$ and $\mathbf{n}$ are uncorrelated implies that:

$$(\text{cov}_{dm})_{ik} = \left\langle \mathbf{r}_i \mathbf{u}_k^T \right\rangle \tag{3}$$

$$(\text{cov}_{dd})_{ij} = \left\langle \mathbf{r}_i \mathbf{r}_j^T \right\rangle + \left\langle \mathbf{n}_i \mathbf{n}_j^T \right\rangle \tag{4}$$

where i and j represent the different grid points of $\mathbf{r}$; k indicates the grid point of $\mathbf{u}$; $\left\langle \mathbf{n}_i \mathbf{n}_j^T \right\rangle$ denotes the error covariance matrix; and $\langle \times \rangle$ is the expected value operator. The error covariance matrix is assumed to be:

$$\left\langle \mathbf{n}_i \mathbf{n}_j^T \right\rangle = S_r^2 \mathbf{I} \tag{5}$$

where $\mathbf{I}$ is the identity matrix, and S_r^2 is the noise variance of $\mathbf{r}$. From (1), (3), and (4) can be written as:

$$(\text{cov}_{dm})_{ik} = \mathbf{g}_i^T \left\langle \mathbf{u}_i \mathbf{u}_k^T \right\rangle \tag{6}$$

$$(\text{cov}_{dd})_{ij} = \mathbf{g}_i^T \left\langle \mathbf{u}_i \mathbf{u}_j^T \right\rangle \mathbf{g}_j + S_r^2 \mathbf{I} \tag{7}$$

Kim et al. (2007) express the covariance matrix for $\mathbf{u}$ in terms of the correlation and variance:

$$\left\langle \mathbf{u}_i \mathbf{u}_k^T \right\rangle = S_s^2(\mathbf{x}_k) \mathbf{I} r(\mathsf{D} \mathbf{x}_{ik}) \tag{8}$$

$$\left\langle \mathbf{u}_i \mathbf{u}_j^T \right\rangle = S_s^2(\mathbf{x}_k) \mathbf{I} r(\mathsf{D} \mathbf{x}_{ij}) \tag{9}$$

where $S_s^2(\mathbf{x}_k)$ is the signal variance of $\mathbf{u}$ at the grid points $\mathbf{x}_k$; $r(\mathsf{D} \mathbf{x}_{ik})$ is the spatial correlation function between $\mathbf{x}_i$ (the grid points of $\mathbf{r}_i$) and $\mathbf{x}_k$ (the grid points of $\mathbf{u}_k$); and D is the distance between these grid points. Note that (9) is similar to (8) and is the spatial correlation function for grid points of $\mathbf{r}$ at $\mathbf{x}_i$ and $\mathbf{x}_j$. Kim et al. (2008) define the spatial correlation function to be:

$$r(\mathrm{D}\mathbf{x}) = \exp\left(-\sqrt{\left(\frac{\mathrm{D}x}{l_x}\right)^2 + \left(\frac{\mathrm{D}y}{l_y}\right)^2}\right) \tag{10}$$

where l_x and l_y are the decorrelation length scales in the x and y directions, respectively. These length scales are discussed in the following section.

1.4.2 Setting the parameters of OI

1) Signal and error variances

The covariance matrices require *a priori* knowledge of s_s^2 and s_r^2. Following Kim et al. (2008) and Kohut et al. (2012), we determine these parameters by calculating standard deviations of the measured **r**. For the measured **r** from Barrow, Wainwright, and Point Lay HFR in 2010, the standard deviations are 21.68 cm s^{-1}, 17.87 cm s^{-1}, and 6.39 cm s^{-1}, respectively, with an average value of ~15 cm s^{-1}. We doubled the standard deviation to ensure it was not underestimated, resulting in s_s^2 equal to 900 cm^2 s^{-2}. An examination of other assumed s_s^2 values (e.g., 200, 500, 1500 cm^2 s^{-2}) indicated that the OI results were largely insensitive to our choices.

The error variance (s_r^2) is attributed to measurement uncertainties. Liu et al. (2010) found the root-mean square (RMS) difference ranged from 6 – 10 cm s^{-1} for hourly **r** for 5 MHz SeaSonde systems. Lipa (2003) found that the RMS difference converged to 10 cm s^{-1}, although that estimate was based on 25 MHz systems. We chose an RMS difference of 10 cm s^{-1} as a reasonable estimate of the measurement uncertainties for our sites and set s_r^2 to 100 cm^2 s^{-2} in (5). This estimate is three times larger than that of Kim et al. (2008) who used OI on 25 MHz systems. The larger error variance leads to smoother estimates, suppresses noise, and is chosen as reasonable in our study domain.

2) Decorrelation length scale and search radius

Kim et al. (2008) recommend the decorrelation length scale be within a factor of four of the spatial resolution of **u**. Following Kim et al. (2007), we find the range of l_x to be 21 - 71 km in 2010 and 18 - 42 km in 2011, while the ranges for l_y are 10 - 15 km and 9 - 11 km. When compared with l_y, the larger values of l_x are due to the ACC. Differences between years could be due to differences in the temporal span (2011 had a longer data set) and/or because the ACC was more coherent in 2011 than in 2010 (Weingartner et al. 2013). The spatial correlation structure was examined across the ACC near Wainwright by decomposing the radar-estimated **u** (by the UWLS method) into along-shore (56°T) and cross-shore (326°T) velocity components for a 100-km long transect. Results indicate that the e-folding scale of the cross-shore velocity component is larger than the along-shore scale, so the larger l_x found here is expected.

The values of l_x or l_y should not be so large as to include **r** far from the **u** grid point because too large a value may over-smooth and blur small scale variations. Kim et al. (2008) suggested that the calculated decorrelation length scale from the HFR data should be treated as an upper bound. Kohut et al. (2012) showed that the OI estimates were insensitive to changes in the decorrelation length scales. In this analysis l_x and l_y were defined as 12 km (twice the spatial resolution) and the same as d_o used in the UWLS method (Figure 1.1). We will show that this choice still captures the general circulation pattern of surface currents as detected by the UWLS method. The d_o in OI sets the smallest spatial weighting far from **x** and is defined as $d_o =$ 35 km. Hence for OI, the spatial correlation weight function decreases to 0.24 at 12 km and 0.05 at 35 km.

1.4.3 Implementing OI

The OI algorithm (provided by Dr. Sung Yong Kim) works in conjunction with the HFR_Progs toolbox. The first step of the algorithm loads **r** and its corresponding bearing. These bearings comprise the angle matrix, **g**, and the given s_s^2 and s_r^2 variances are constructed as given by (7 - 9). Then the distance ($D\mathbf{x}_{ij}$) between grid points of $\mathbf{r}_{ij}$, the distance ($D\mathbf{x}_{ik}$) between grid points of different $\mathbf{r}_i$, and the grid point ($\mathbf{x}_k$) of the estimated $\mathbf{u}_k$ are calculated and used in (8) and (9) to compute the local spatial correlation function. Afterwards the data-model and data-

data covariance matrices, (6) and (7), are computed. Finally, the OI estimated **u** is retrieved from (2).

1.4.4 An example of OI estimated surface currents and their relationship with GDOP

Before introducing the OI estimated **u**, we present a map of **u** estimated by the UWLS method using 35 km for d_o (Figure 1.4; chosen at the same hour as in Figure 1.1). Although the data gap north of Icy Cape is filled, vector magnitudes in this region are amplified, and the GDOP value is high (~3). This amplification is a typical example of GDOP instability. Vectors are also magnified along the edge of the radar mask due to the equal weighting of **r**. Treating **r** measured 35 km and 5 km away from the grid for **u** with the same weight is likely unreasonable.

For the same dataset, an example of OI estimated **u** is shown in Figure 1.5. The OI estimated **u** fill the gap north of Icy Cape and capture nearly identical features as that in Figure 1.1. For example, the eddy-like current field northwest of Point Lay is very similar in both methods. However, the amplified vectors seen in Figure 1.1 and Figure 1.4 are not present in the OI estimates of Figure 1.5. This is especially true along the boundary of the radar mask because the OI method tapers the solutions toward zero when the number of **r** at a given $\mathbf{x}_k$ is insufficient to estimate $\mathbf{u}_k$ (Kim et al. 2008). Although located in a region of high GDOP, these vectors are not amplified. This suggests that GDOP may not be applicable to the OI method. Instead, we compute the condition number (CN) of $\mathrm{cov}_{dm}^{T}\,\mathrm{cov}_{dd}^{-1}$ (see section 1.5), which is a measure of the sensitivity of the inverse of a matrix and reflects how much variation will be brought to **u** from small variations in **r**. In Figure 1.5, the radar mask is split into two relatively low CN zones (< 2), with high CN zones (> 2) found north of Icy Cape and in the outer edges of the radar mask. In aggregate the locations of the tapered vectors within the spatial structure of CN suggest that CN is the OI analog to GDOP used in the UWLS method. Note that the computed CN results from the matrix containing both angles and the correlation function, whereas GDOP is solely from the angle matrix. We will show later that CN is one of the controlling factors for OI estimate quality.

Nevertheless, there are notable differences between the two methods. For example, all surface currents are southwestward in the UWLS estimate north of 72°N, whereas sheared flows are evident in the OI estimate. If the OI method is used to process HFR data, it is worth

determining if such features are reliable. Kim et al. (2008) illustrated the uncertainties of the OI estimates in terms of error ellipses. However, we will show that large and small error ellipses may appear in the same location, thus making interpretation difficult. To examine the source of such discrepancies, we investigate the limitation of (2) using a series of test simulations in Section 1.5.

1.5 Error analysis

1.5.1 Unidirectional flow field

1) Uniformly eastward current

The first test scenario considers a simple flow field of spatially uniform, time-invariant eastward currents of $u = 10$ cm s^{-1} and $v = 0$ cm s^{-1}. This flow field is converted to $\mathbf{r}$ based on (1) for each of the radial velocity grid points (Figure 1.3). The resulting $\mathbf{r}$ are then used to estimate $\mathbf{u}$ via the UWLS method (with d_o set to 35 km for comparison) and the OI method described in Section 1.4. Results, shown in Figure 1.6a, indicate that the OI-resolved $\mathbf{u}$ are well-determined over most of the radar mask; however veered vectors, with reduced magnitudes, are found along the boundary of the radar mask and along the baselines between radar sites. The UWLS-resolved $\mathbf{u}$ are all well-determined and unbiased. In other words, in particular regions the OI method produces currents containing north-south velocity components even though the flow is purely eastward. North of the Barrow HFR site (~157ºW, 72ºN, hereafter referred to as region B), there is a region where the OI estimated $\mathbf{u}$ are very weak (Figure 1.6b-Figure 1.6c). This region is unique because just west of it the OI estimated $\mathbf{u}$ are very nearly eastward. We examine this region in more detail in the following section.

2) Uniformly northward current

In this second scenario the input flow field has constant and spatially uniform northward currents ($u = 0$ cm s^{-1} and $v = 10$ cm s^{-1}). Following the same procedure as before, the OI-resolved $\mathbf{u}$ are shown in Figure 1.7a. Again, the resulting $\mathbf{u}$ by the OI method are all reasonable near the center of the radar mask. However, near the boundary of the radar mask and along the

16

radar baselines the OI method tends to generate east-west velocity components. In contrast, Figure 1.6c, which contained very weak **u** for the constant east-west flow case, now has a good estimate (Figure 1.7c). Region B is representative of similar regions within the radar mask. Its main characteristic is that it is near the boundary of the radar mask, outside of the limit of **r** coverage by the Wainwright radar; however, **u** are derived in this region due to the large d_o. Note that the UWLS method provides perfect estimates, even in regions of high GDOP. This suggests UWLS is an unbiased estimator in this modeled flow where **n** = 0. However, the estimated **u** in region B from the two modeled flows show distinctly different results indicating OI is a biased estimator due to weighting of **r** in d_o.

In region B, the majority of the incorporated **r** are from the Barrow HFR and oriented in an approximately north-south direction. For eastward currents, **r** cannot be properly resolved because $\mathbf{u} \times \hat{\mathbf{x}}_r \sim 0$. Although there are those that can be resolved within d_o, they are far away from the grid point of the estimated **u**. Therefore, these **r** have small weight with the result being a biased estimate of **u**. Conversely, for northward currents, **r** can be properly resolved in the OI d_o and produces a valid result. This suggests that in the case of OI, if the majority of the incorporated **r** are from a single HFR site, significant bias errors will be found in estimated **u**.

Similar experiments were conducted using $(u, v) = (10, 10)$, $(u, v) = (8, 6)$, $(u, v) = (-8, 6)$, $(u, v) = (1, 10)$, and $(u, v) = (10, 1)$. The results show similar patterns of large bias errors in regions where **r** is poorly resolved. Therefore, if one interprets the OI estimates by mapping the uncertainty ellipses, large and small ellipses may appear in the same location. Such discrepancies are an outcome of applying unidirectional flow fields where **r** may be only partially resolved. Generalizing, we next apply a varying flow field to study the source of uncertainties in the OI method.

1.5.2 Multidirectional flow field

1) Double-gyre system

We next examine a temporally- and spatially-varying flow field motivated by Shadden et al. (2005). This flow consists of a double-gyre system similar to the observed surface current

patterns (Figure 1.1, Figure 1.5). We also incorporate a low frequency time variation such that the flow field involves the two gyres propagating southward at ~0.3 m s^{-1} across the northeastern Chukchi Sea. The streamfunction for this test flow field is:

$$\psi(x,y,t) = A\sin(K\pi f)\sin[K\pi(y - 71 + 0.02t)/4] + 3A\sin(10^{-4}\pi xy + t) \qquad (11)$$

where

$$f(x,t) = a[(x + 169)/6.5]^2 + b[(x + 169)/6.5] \qquad (12)$$

$$a(t) = E\sin(Wt) \text{ and } b(t) = 1 - 2E\sin(Wt) \qquad (13)$$

Parameters are t (an arbitrary integer), $E = 0.55$, $W = 2\pi/20$, $K = 1$ (scale factor), and $A = 50$. The velocity field $\mathbf{u_m} = (u_m, v_m)$ is then given by:

$$u_m(x,y,t) = -\frac{\partial\psi}{\partial y} \text{ and } v_m(x,y,t) = \frac{\partial\psi}{\partial x} \qquad (14)$$

Here u_m and v_m are computed for every grid point of $\mathbf{r}$ by (1) and then converted to their radial velocity components ($\mathbf{r_m}$). Note in the following analysis that these grid points mimic the coverage of the 2010 HFR observations, and the flagged locations indicated by the gaps in Figure 1.3 have no data. The entire simulated velocity field lasts for 205 hourly time steps, or ~8 days of HFR measurements. $\mathbf{r_m}$ are used to estimate $\mathbf{u}$ using the OI method. We note that the estimated $\mathbf{u}$ are computed for an ideal situation insofar as the grid points of $\mathbf{r_m}$ for each of the three HFR have continuous data for the 205-hour span, except for the flagged grid points. When modeled and OI-derived $\mathbf{u}$ are plotted together, disparities become evident (Figure 1.8). In the regions farthest offshore, north of Icy Cape and in the HFR baselines, the resultant $\mathbf{u}$ differ in direction and magnitude. To examine the possibility that the OI method may over-smooth small-scale features, we also modeled a flow field having small-scale spatial variations by setting $K = 3$ in (11) (Figure 1.8d). This small-scale flow field contains eddies of ~30 km radius in comparison to the test eddies with ~120 km radius. The results indicate that spatial variations on this scale are still captured by the OI technique.

2) Statistical metrics

The performance, or skill, of the OI method is based on quantitative agreement between the modeled ($\mathbf{u_m}$) and resulting currents ($\mathbf{u}$). Utilizing the test field described by (11) – (14) and following Willmott (1981), Warner et al. (2005), and Liu et al. (2010), skill (on a [0 - 1] scale) is:

$$Skill = \frac{1}{2}(SU + SV) \tag{15}$$

where

$$SU = 1 - \frac{\sum_{t=1}^{205} \left| u_{t,m} - u_{t,o} \right|^2}{\sum_{t=1}^{205} \left(\left| u_{t,m} - \bar{u}_{t,o} \right| + \left| u_{t,o} - \bar{u}_{t,o} \right| \right)^2} \tag{16}$$

$$SV = 1 - \frac{\sum_{t=1}^{205} \left| v_{t,m} - v_{t,o} \right|^2}{\sum_{t=1}^{205} \left(\left| v_{t,m} - \bar{v}_{t,o} \right| + \left| v_{t,o} - \bar{v}_{t,o} \right| \right)^2} \tag{17}$$

Subscript m and o represent the modeled and the OI estimated flow, respectively, and the overbar indicates an average of the 205 time steps. SU and SV represent the agreement between the known field and OI estimate for the two velocity components. A skill = 1 indicates perfect agreement, and skill = 0 indicates no agreement.

We also compute the complex correlation function for the two vector fields and the phase angle following (Kundu 1976; Shay et al. 2007):

$$\phi = \tan^{-1} \frac{\sum_{t=1}^{205} \left(u_{t,o} v_{t,m} - v_{t,o} u_{t,m} \right)}{\sum_{t=1}^{205} \left(u_{t,o} u_{t,m} + v_{t,o} v_{t,m} \right)} \tag{18}$$

where f is the average angular difference between the estimated vector and the modeled vector. A positive f is the average cyclonic rotation of the modeled current with respect to the estimated current, and a negative f is the average anti-cyclonic rotation.

3) Performance of OI

The spatial distribution of the skill of the OI estimates (Figure 1.9) shows areas of high confidence (skill $\geq$0.7). We chose a skill $\geq$0.7 as being reliable because the associated phase shifts, as discussed below, are also small. Of interest is that the skill in the gap north of Icy Cape is quite low (<0.4), suggesting that such areas cannot be reliably estimated by OI. Low-skill regions also circumscribe the high-skill interior. A majority of the low-skill regions coincide with the flagged grid points during the QA/QC process (Figure 1.3). This implies that these regions are incorporating relatively few **r** and/or that the **r** mostly originate from the same HFR site and thus yield large biases.

In the interior of the radar mask where the skill $\geq$0.7, phase shifts (Figure 1.10) are quite small, ~2° (the difference in magnitude between the modeled and estimated vectors is <0.1%). However, phase shifts as large as 20° (accompanied by a reduction of ~6% in vector magnitude) occur along the baselines and boundary of the radar mask. This result explains the weak currents and shear found in OI estimated currents (Figure 1.5). In summary, OI appears to be a robust estimator for a variable flow field in the interior of the radar mask although it is limited along the radar mask baselines and boundary.

4) Factors controlling OI performance

The number of available incorporating **r** (AR), within a three-hour averaging period, from all HFR in d_o is examined for every grid point of **u** (Figure 1.11). The largest AR values are found near the HFR in Wainwright and Point Lay and lower AR occur farther offshore from these HFR. When comparing Figure 1.11 with Figure 1.9, the area with high skill ($\geq$0.7) does not match that with high AR. If AR is the dominant factor influencing the skill of OI estimates, then Figure 1.9 should have a distribution similar to the high AR distribution, however higher AR values are found nearshore and decrease as one moves offshore, unlike skill that remains high even in offshore regions, indicating that AR alone is not the sole factor influencing OI estimates.

In this regard, the number of **r** from each individual HFR plays an important role. We define the ratio of overlapping radial velocities (ROR) as:

$$\mathrm{ROR}_{d_o} = \frac{\mathrm{NR}_1}{\mathrm{NR}_2} \tag{19}$$

where $\mathrm{NR}_{i,\,i=1,2}$ is the number of available incorporating $\mathbf{r}$ in d_o from each radar, with $i = 1$ and 2 being the primary and secondary $\mathbf{r}$ contributor, respectively. For example, for a three-hour averaging period for d_o at $\mathbf{x}$, there are 60 $\mathbf{r}$ from Wainwright, 20 from Barrow, and 15 from Point Lay, then ROR at $\mathbf{x}$ is $60/20 = 3$. ROR is related to geometric radial coverage and, ideally, should be close to 1. An ROR much greater than one means the incorporating $\mathbf{r}$ are primarily from one radar site. ROR is useful in ascertaining potential bias errors, which can be represented by the contribution of available incorporating $\mathbf{r}$ in d_o. For cases where $i > 2$, we argue that the role of the ith HFR is insignificant here, but can be beneficial to condition $\mathrm{cov}_{dm}^T\,\mathrm{cov}_{dd}^{-1}$ as discussed below.

The spatial distribution of ROR at each grid point is shown in Figure 1.12. Two regions with relatively low ROR (<4) are encircled by areas with high ROR (>7), similar to the spatial distribution of skill (i.e., regions with high ROR correspond with locations of low skill OI estimates). This suggests that ROR is more important than AR in the OI method and helps explain the discrepancies in the unidirectional flow cases. ROR is high in regions where $\mathbf{r}$ is predominantly from a single radar site and high bias errors are found. Consequently, near the observation gap north of Icy Cape, where AR has a modest value ($\sim$400), the skill is low and does not necessarily correspond to the AR score. Regions with low ROR tend to be properly resolved with reduced bias errors suggesting ROR is a better proxy than AR for interpreting data quality.

It is interesting to examine the response of OI estimates in areas with low AR and low ROR. Although low ROR appears to provide a better index of data quality, the fundamental basis of OI is the correlation function (10). If the correlation function fails to describe the relationship between $\mathbf{r}$ in circumstances when AR and ROR are low, the correlation function will be poorly represented in (8) and (9). Since this function is used in forming the linear estimates of $\mathbf{u}$ based on $\mathbf{r}$ by (2), we need to understand the sensitivity of the OI method to the correlation structure, which depends upon AR and ROR.

OI is a linear estimation method, in which $\text{cov}_{dm}^{T}\,\text{cov}_{dd}^{-1}$ is the mathematical operator that estimates **u** from **r**. In objective analysis, $\text{cov}_{dm}^{T}\,\text{cov}_{dd}^{-1}$ represents the correlation matrix in which the positive definiteness is described by fitting an analytical correlation function (10). If the current field is difficult to describe analytically, correlation estimates that do not yield positive definite matrices will be sensitive to small variations in the analysis parameters and can result in erratic estimates (Carter and Robinson 1987). This sensitivity can be measured by computing the CN of the correlation matrix, indicating how much the error is magnified upon converting **r** to **u** (Arfken et al. 2005). Even small variations in **r** may lead to large changes in **u** if CN is large. Recall that CN results from the matrix containing both angles and the correlation function, whereas GDOP is solely from the angle matrix. Hence, as mentioned in Section 1.4, we suggest that CN is the OI analog to GDOP, preferred in the UWLS method.

We computed the CN of $\text{cov}_{dm}^{T}\,\text{cov}_{dd}^{-1}$ and plotted its spatial distribution at each grid point for which there is a corresponding OI estimate (Figure 1.13). Grid points with relatively high CN (>5) encircle the outer edge of the radar mask and those with low CN (<2) (centered around ~164ºW, 70.5ºN and 160ºW, 71.5ºN), similar to the spatial distribution of skill (>0.7) and phase shift (<2º) (Figure 1.9, Figure 1.10). A comparison of the CN map with the ROR pattern indicates that high CN areas match areas with high ROR. When we encounter regions of low CN that coincide with high ROR skill may be low, indicating that while $\text{cov}_{dm}^{T}\,\text{cov}_{dd}^{-1}$ may be well conditioned, the estimator is dependent on the contribution of the incorporating **r**.

The spatial patterns of AR, ROR, and CN suggest a relationship among these factors. The correlation between ROR vs. AR is -0.01 and not significantly different from 0. However, the correlation between CN and AR is -0.39 and that between CN and ROR is 0.58, with both results significant at the 95% level (Figure 1.14). Therefore, CN is a function of both AR and ROR. In most HFR operations, data gaps are unavoidable, and as gaps occur the AR and ROR patterns will change, modifying the structure of the correlation matrix and affecting current estimates. Our analysis shows that AR, ROR, and CN interact with each other during data processing and effect the accuracy of OI estimates.

AR is based on the HFR data, while CN is based on the correlation matrix. However, prior to HFR set up and operation, these two factors are unknown. ROR is a result of the radar

22

geometry due to HFR siting, which can be examined beforehand. Once d_o is decided, the ROR pattern can be determined for the OI estimated currents. This may be crucial for site planning or short-term deployments of HFR (Barrick et al. 2012). Thus we suggest that ROR serve as a planning tool in assessing potential errors in OI.

5) Sensitivities to random gaps

The previous analysis is based on noise- and gap-free conditions, which is not realistic in most HFR operations. Kim et al. (2008) show that the OI method can effectively smooth noise and provide more precise solutions than the UWLS method, true for Gauss-Markov estimators (Wunsch 2006). Kim et al. (2008) did not examine the sensitivity of OI to data with temporal gaps. We consider a simple condition in which the signal-to-noise ratio of the returned radar signal is below 6 dB (the default threshold in SeaSonde processing software). In this case, the spectra will be flagged as an outlier and produce a gap in $\mathbf{r}$. The following effort seeks to understand the consequences of observation gaps on the quality of OI estimates.

We apply the Monte Carlo method on nine selected grid points (Figure 1.15) chosen to represent areas in the interior (IS, IN), edge (ESW, ENW, ENE1, ENE2, EN), and central (C1, C2) portions of the radar mask. To derive statistically independent comparisons, the d_o for each of the chosen grid points do not overlap. Using the double-gyre flow field, 10–90% of the grid points in d_o are randomly assigned as gaps for all time steps. Note that the remaining $\mathbf{r}$ are still noise free. We then form skill estimates following (15–17), with this procedure repeated 100 times to form 95% confidence intervals on the estimated mean. The presence of gaps also means that the structure of $\mathrm{cov}_{dm}^{T}\,\mathrm{cov}_{dd}^{-1}$ may be changed, so we compute the CN after each iteration.

Variation in the skill of OI estimates and the CN of $\mathrm{cov}_{dm}^{T}\,\mathrm{cov}_{dd}^{-1}$ are shown in Figure 1.16. The interior grid points (IS, IN) are very resilient to gaps, even when only 10% of the data occurs in the d_o. This result further underscores the importance of high AR and low ROR, for it enables $\mathbf{u}$ in regions with densely overlapping $\mathbf{r}$ to be well resolved. It also suggests that velocity estimates can be properly resolved based on *a priori* statistics even though there may be many data gaps in such regions. For grid points initially having low skill in the gap-free simulations (e.g., ESW, C2, ENE1, ENE2, and EN), adding gaps further erodes the skill. When gaps of 60%

23

or more occur in d_o, the skill values are all below 0.2 in areas with low AR and high ROR. Therefore, increasing the number of gaps in these regions implies that the available **r** tends to originate from the same HFR site and results in bias. For example for ENW, skill drops substantially as the number of gaps increase. Consequently, in cases where there are random gaps, high AR and low ROR are required for reliable OI estimates. This result also highlights that site spacing of the HFR array plays an important role in estimating surface currents using the OI method. If the spacing between HFR sites is not optimal, better data coverage can be improved using the OI method but in certain regions may introduce significant bias errors into the resulting current estimates.

1.6 Discussion and summary

We have assessed the performance of the OI method on a HFR dataset from the Chukchi Sea with site spacing farther than optimal. The focus of the study was on the feasibility of OI under these circumstances and to investigate the applicability of the OI method. Our results offer suggestions and a simple tool to diagnose the performance of the OI method for the broader HFR community. Three factors influence the OI derived data quality: 1) the number of available incorporating **r** (AR) for calculating **u**, 2) the ratio of the incorporating **r** from overlapping HFR sites used in calculating **u** (ROR or radar geometry), and 3) the positive definiteness (condition number; CN) of the correlation matrix, which can be regarded as the equivalent measure as GDOP for UWLS. For operational purposes, the potential performance of the OI method can be evaluated by examining ROR patterns and may be of value in choosing HFR sites. Our idealized experiments show that the OI method is a robust technique in dealing with flow variability and that it provides current estimates with smaller variance than the conventional UWLS method. Regions within the radar mask with high AR and low ROR **u** can be reliably constructed with the OI method even though there may be gaps in the radial data. However, careful attention needs to be paid if the AR is limited because this may result in a high CN and an ill-conditioned correlation matrix, which will amplify errors. If the incorporating **r** are mainly contributed by a single radar site (high ROR), significant bias errors can arise.

This study does not take into account the influence of random noise, which can be widespread and sporadic, although one common situation considered here is the diurnal

interference of the ionosphere. Since this interference is widespread, we have conducted Monte Carlo experiments by adding random noise with varying magnitude on each $\mathbf{r}$ in d_o. The result (not shown) indicates that the skill of OI estimates drops as the magnitude of noise increases. A similar pattern is found if $\mathbf{u}$ are estimated through the UWLS method. Therefore, if the noise source is widespread and comparable to the signal strength, both the UWLS and OI methods lose the ability to make accurate estimates.

The main departure of the OI method from the UWLS method is the use of larger d_o and weighted radials to produce smoother currents and greater data coverage in the resultant current map. We find the major source of erroneous estimates using the OI method depends on ROR, which is a direct function of HFR siting. Before applying the OI method to HFR data, we recommend an analytical flow field (such as that described in section 1.5) with multidirectional patterns to create a map of estimated skill, as this will assist in identifying regions of possible erroneous estimates. Conveniently, ROR can be computed before site installation to highlight locations of substantial bias errors. ROR can also be computed in real-time data processing, to provide a tracking criterion for how bias errors may be introduced into the OI surface current estimates.

1.7 Acknowledgments
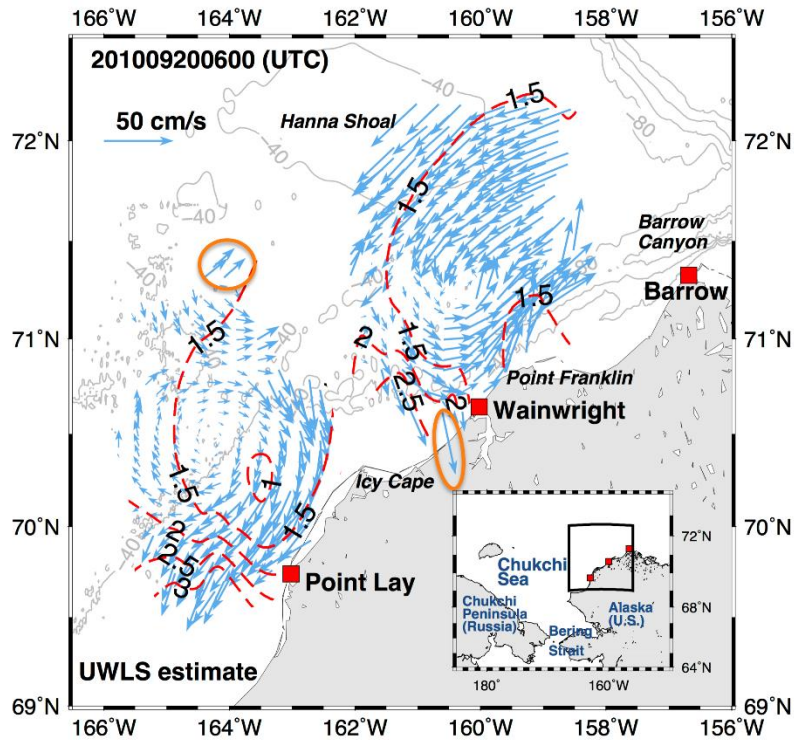
Figure 1.1. Surface currents from September 20, 2010 at 06:00 UTC mapped by the Chukchi Sea HFR array (red squares) using the UWLS method. Orange circles highlight current solutions with high GDOP (red dashed contours). Gray contours indicate bathymetry at 40 m intervals. For clarity, only subsampled vectors are shown.
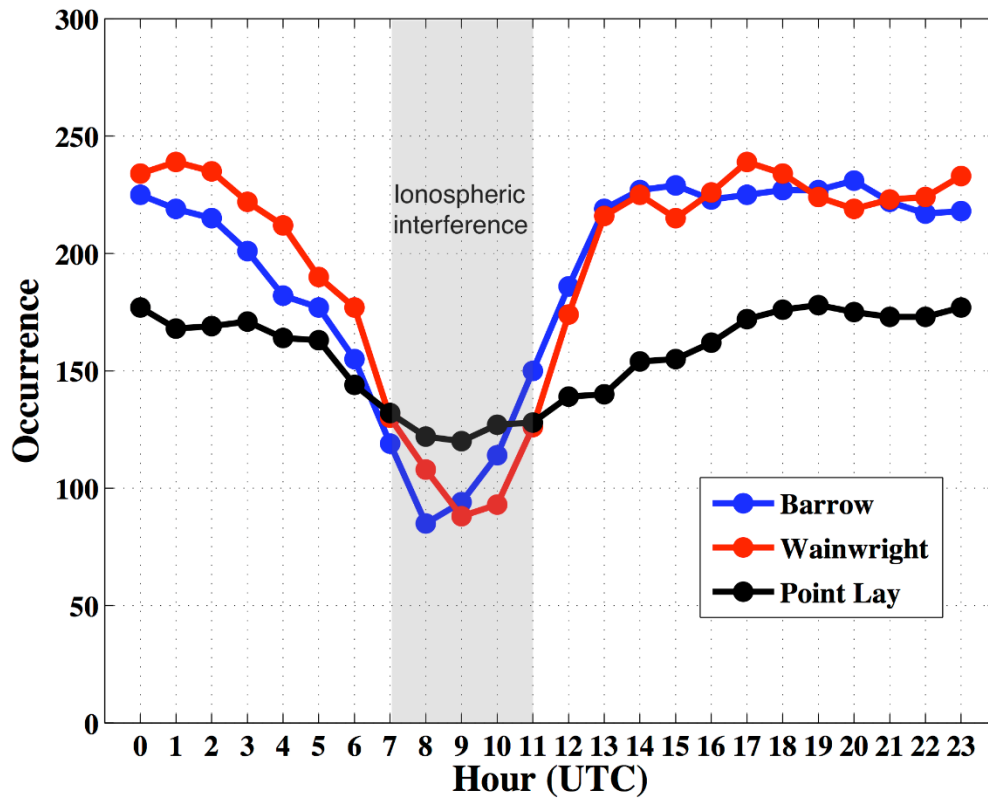
Figure 1.2. Average number of 2010 HFR data returns per hour of day for Barrow (blue), Wainwright (red), and Point Lay (black). Shaded area indicates the period of ionospheric interference. Similar results were found for 2011.
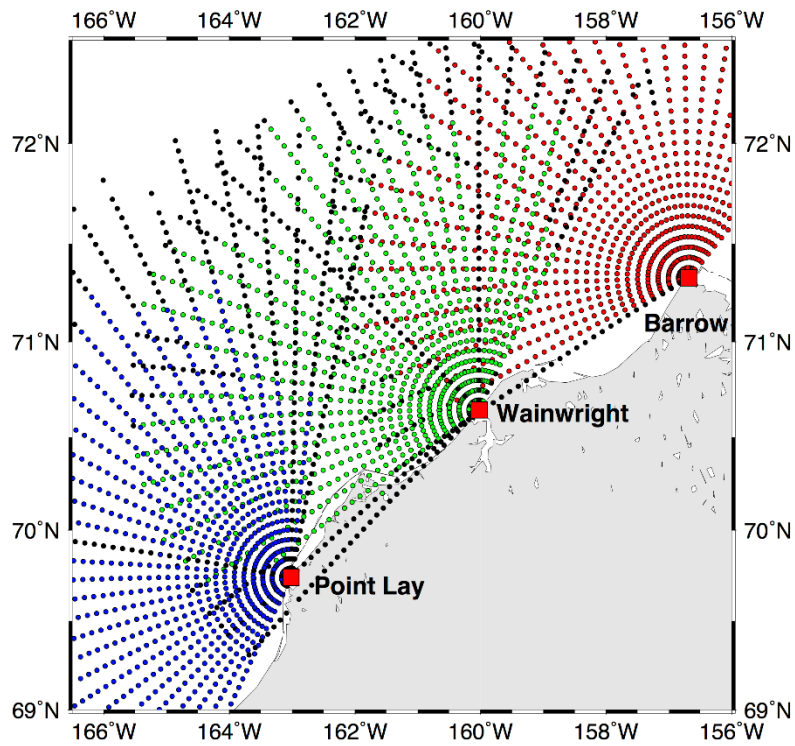
Figure 1.3. Grid points of radial velocities measured by the HFR in Barrow (red), Wainwright (green), and Point Lay (blue) during the 2010 operating season. Black dots indicate grid points that were removed from the dataset during the initial QA/QC process.
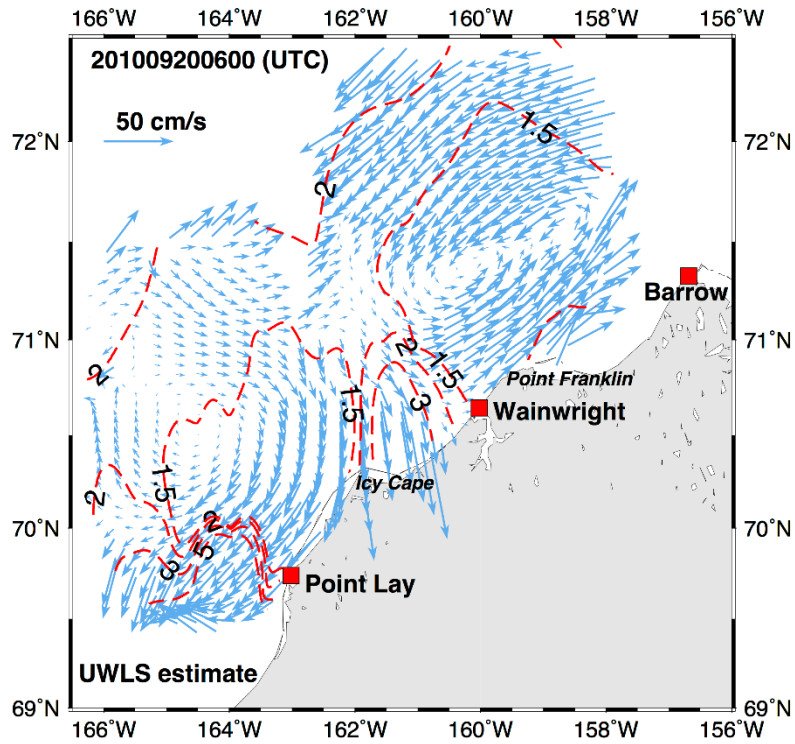
Figure 1.4. Same as Figure 1.1 but using 35 km for search radius. Red dashed contours show corresponding GDOP. For clarity, only subsampled vectors are shown.
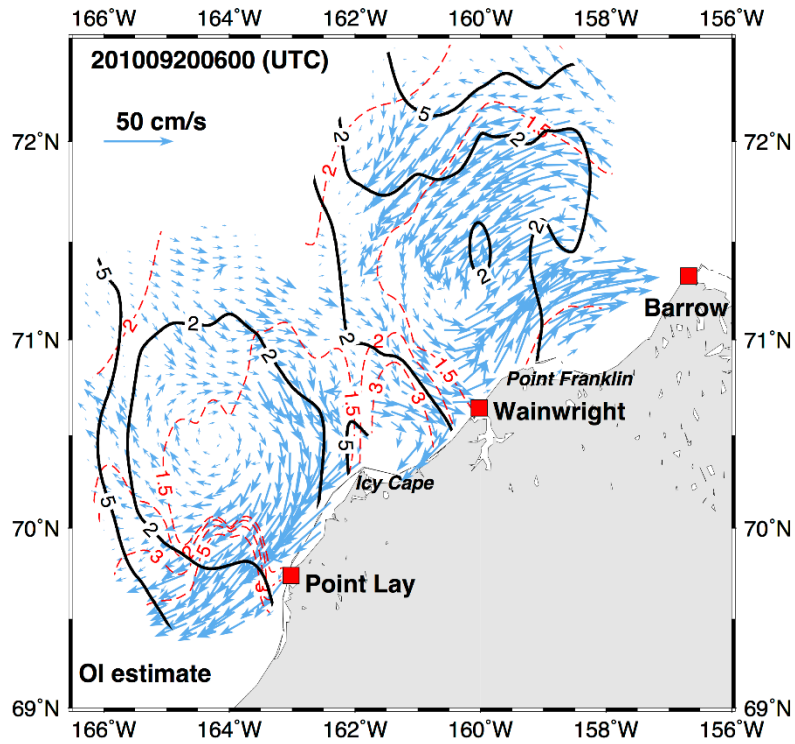
Figure 1.5. Surface currents from September 20, 2010 at 06:00 UTC mapped by the Chukchi Sea HFR array (red squares) calculated using the OI method. Red dashed contours show GDOP computed using the UWLS method with 35-km search radius. Black contours indicate the CN of $\text{cov}_{dm}^{T}\,\text{cov}_{dd}^{-1}$ (see text). For clarity, only subsampled vectors are shown.
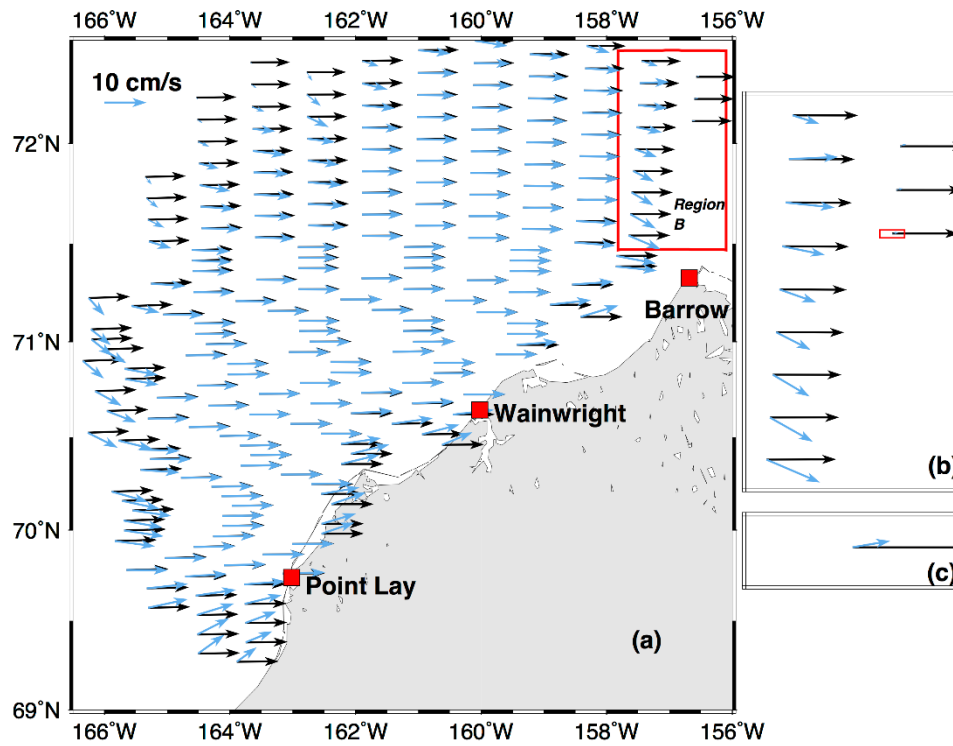
Figure 1.6. (a) An example of the OI (blue) and UWLS (black) estimated surface currents derived from modeled uniformly eastward currents. OI and UWLS vectors are overlapped. For clarity, only subsampled vectors are shown. Red squares represent locations of HFR. The red rectangle highlights region B. (b) An enlargement of region B. The red rectangle highlights the area presented in (c). (c) An enlargement to show the detail of the red rectangle area in (b).
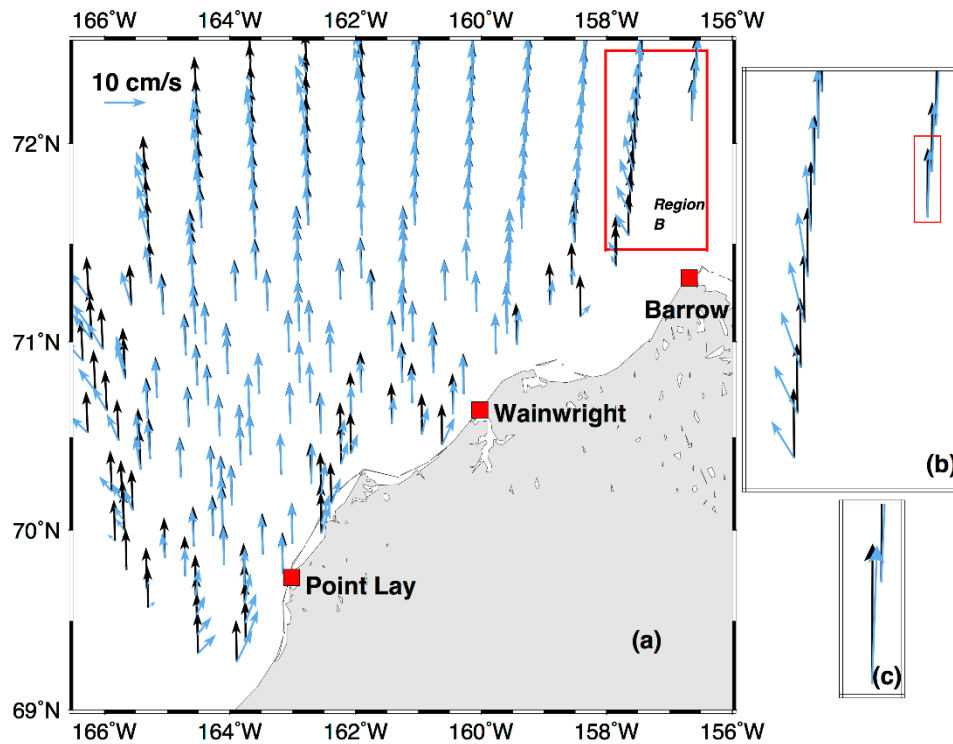
Figure 1.7. (a) An example of the OI (blue) and UWLS (black) estimated surface currents derived from modeled uniformly northward currents. OI and UWLS vectors are overlapped. For clarity, only subsampled vectors are shown. Red squares represent locations of HFR. The red rectangle highlights region B. (b) An enlargement of region B. The red rectangle highlights the area presented in (c). (c) An enlargement to show the detail of the red rectangle area in (b).
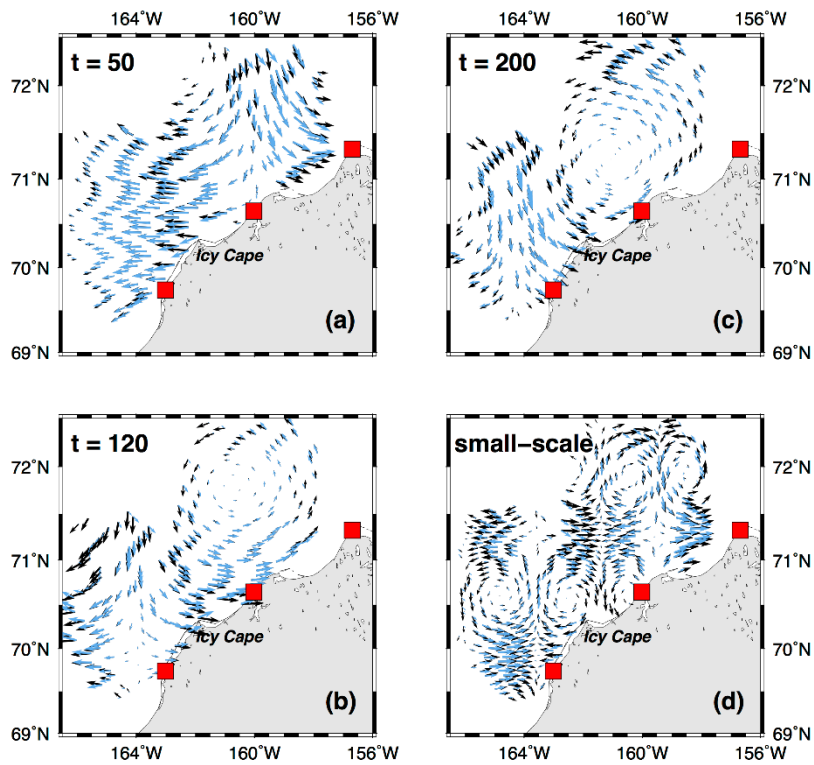
Figure 1.8. (a)-(c) Modeled flow field based on (11)–(14) at three time steps. (d) An example of small-scale modeled flow field by changing the scale factor *K* from 1 to 3 in (11). Blue and black vectors are OI estimated and original modeled currents, respectively. OI and model vectors are overlapped. For clarity, only subsampled vectors are shown. Red squares represent locations of HFR.
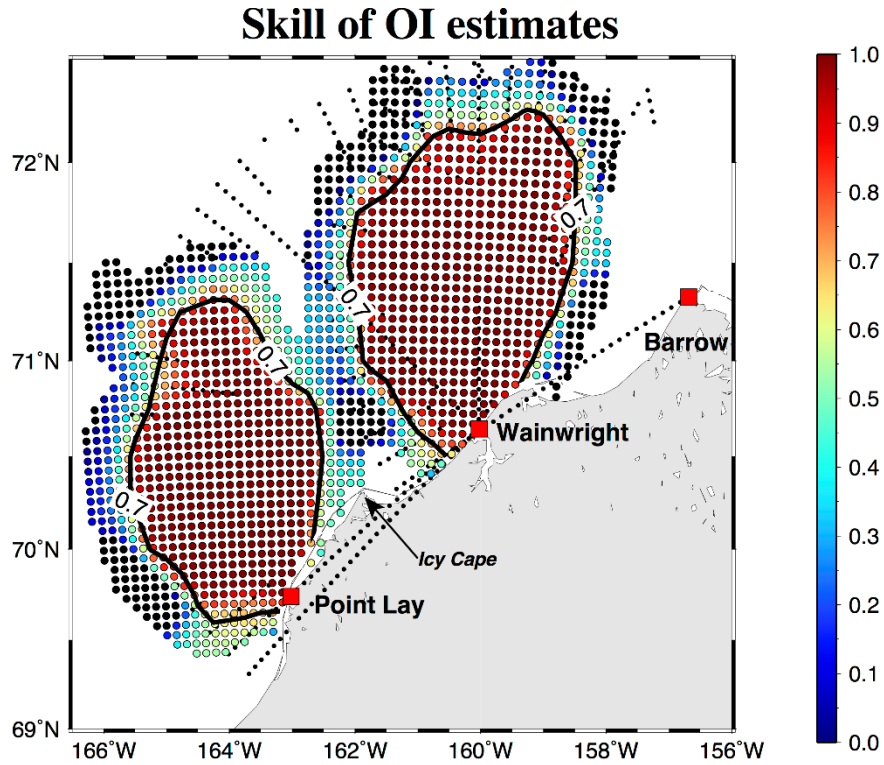
Figure 1.9. Spatial distribution of skill (color shaded) of OI estimates. Small black dots indicate locations of quality flagged radial velocity measurements. The black contour denotes the 0.7 skill level. Red squares are the locations of HFR.
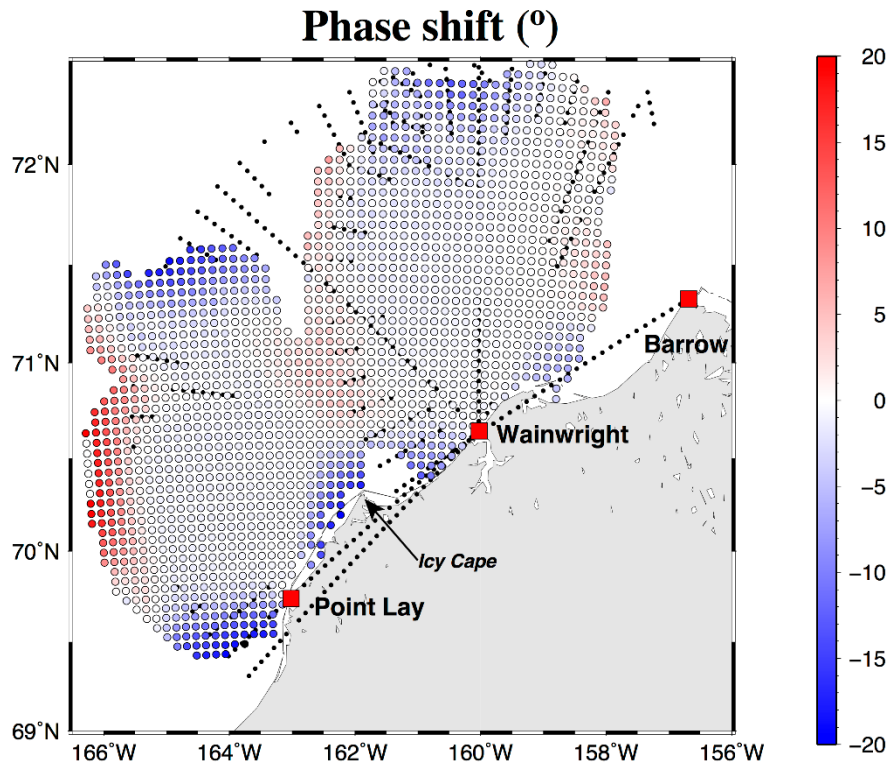
Figure 1.10. Spatial distribution of phase shift (color shaded and in degrees) of OI estimates. Positive values mean counterclockwise rotation of the modeled current with respect to the OI estimated current. Small black dots indicate locations of quality flagged radial velocity measurements. Red squares are the locations of HFR.
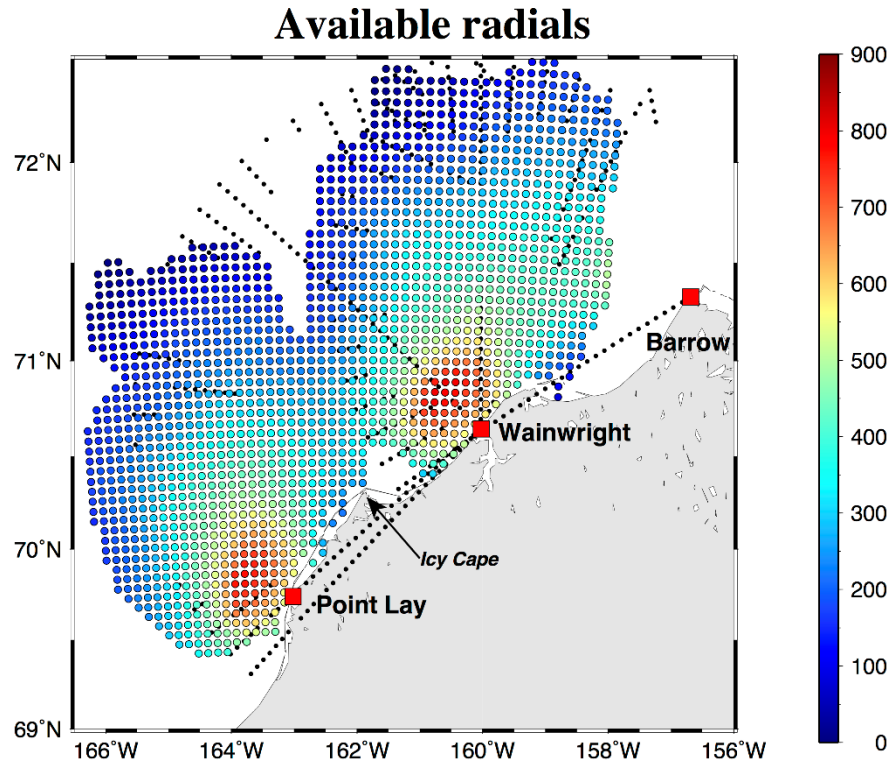
Figure 1.11. Spatial distribution of the available number of incorporating radial velocities (AR; color shaded) for each OI grid point. Small black dots indicate locations of quality flagged radial velocity measurements. Red squares are the locations of HFR.

Ratio of overlapping radials
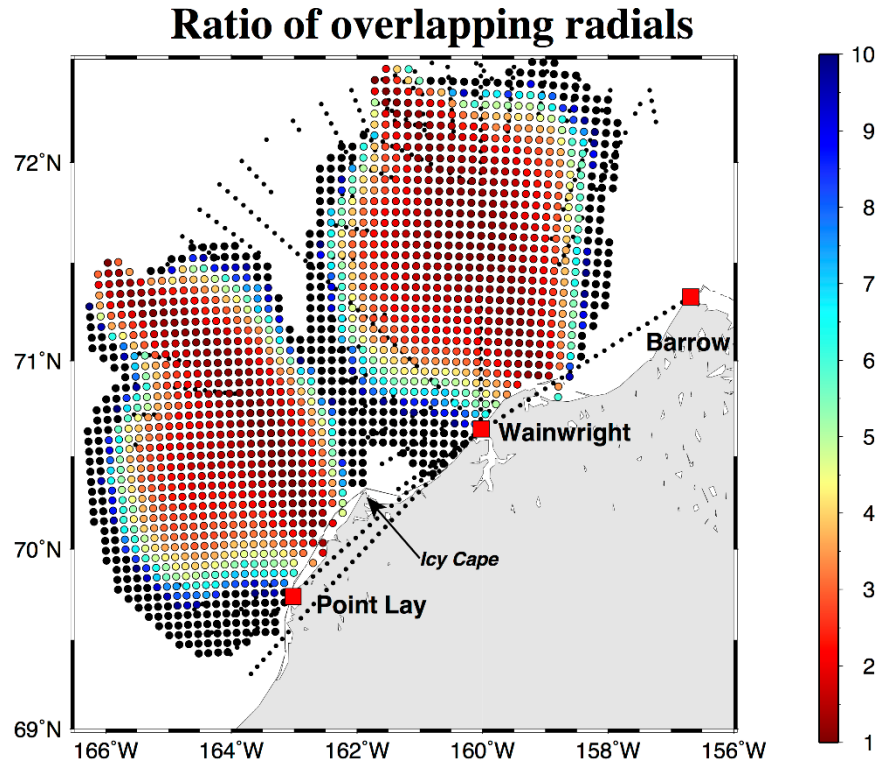
Figure 1.12. Spatial distribution of ratio of overlapping radial velocities (ROR; color shaded) for each OI grid point. Small black dots indicate locations of quality flagged radial velocity measurements. Red squares are the locations of HFR.
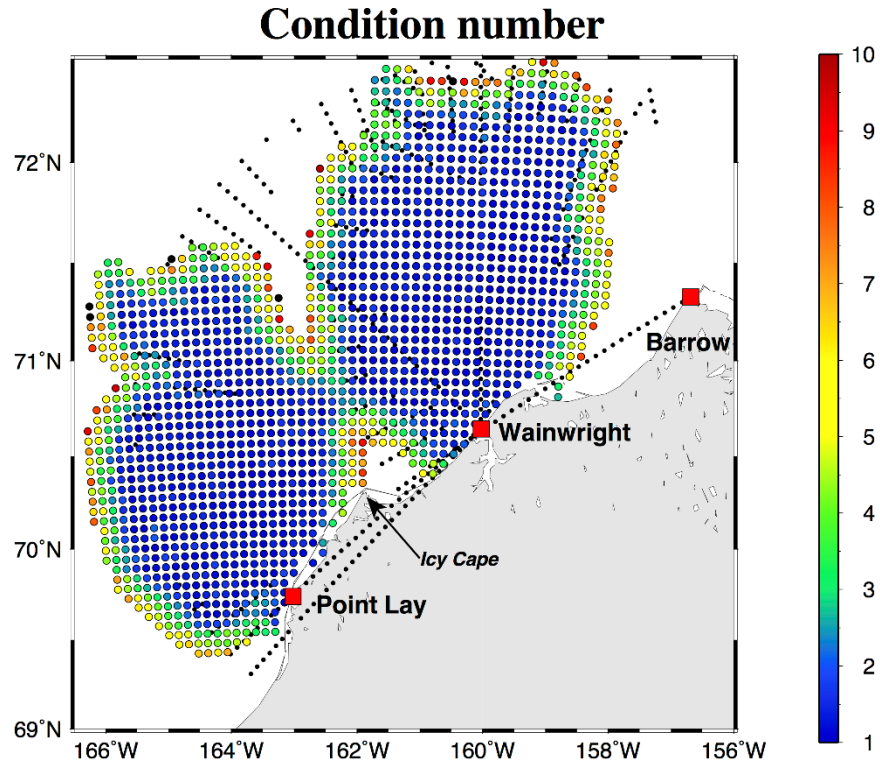
Figure 1.13. The spatial distribution of condition number (CN; color shaded) of $\mathrm{cov}_{dm}^{T}\,\mathrm{cov}_{dd}^{-1}$ at each grid point of the OI estimates. Small black dots indicate locations of quality flagged radial velocity measurements. Red squares are the locations of HFR.
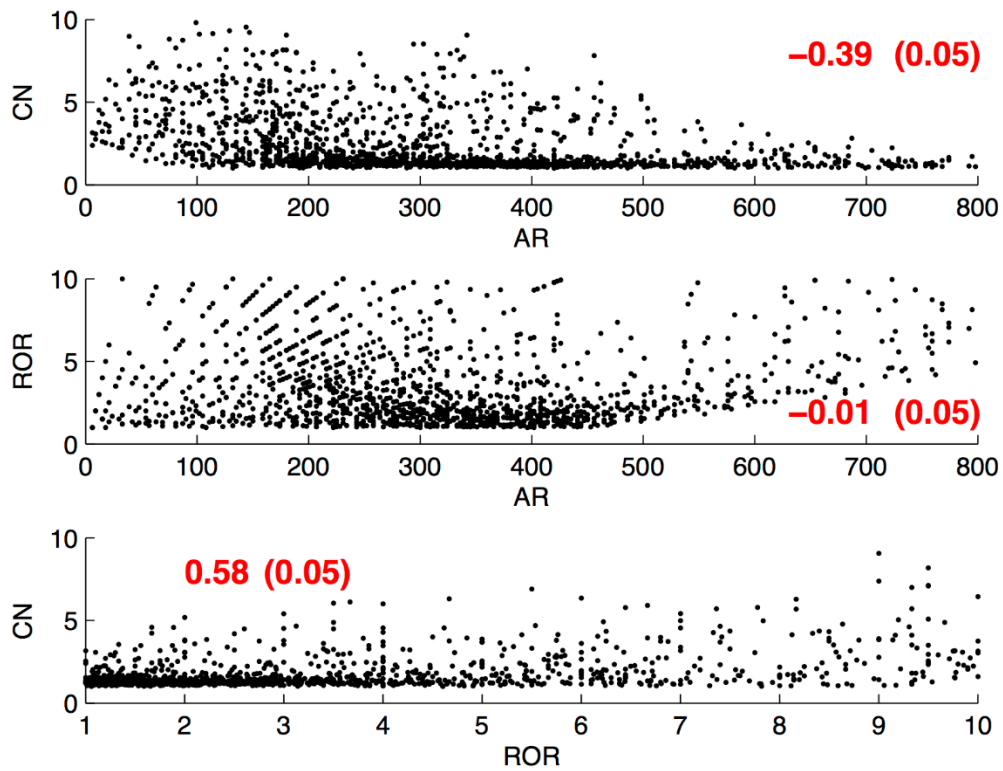
Figure 1.14. Scatter plots of CN versus AR (upper panel), ROR versus AR (middle panel), and CN versus ROR (bottom panel) for the double-gyre system (see Figure 1.11–13). The corresponding correlation coefficient is shown in red, and the number in parenthesis refers to the 95% significant level. Note the x and y axes have different scales.
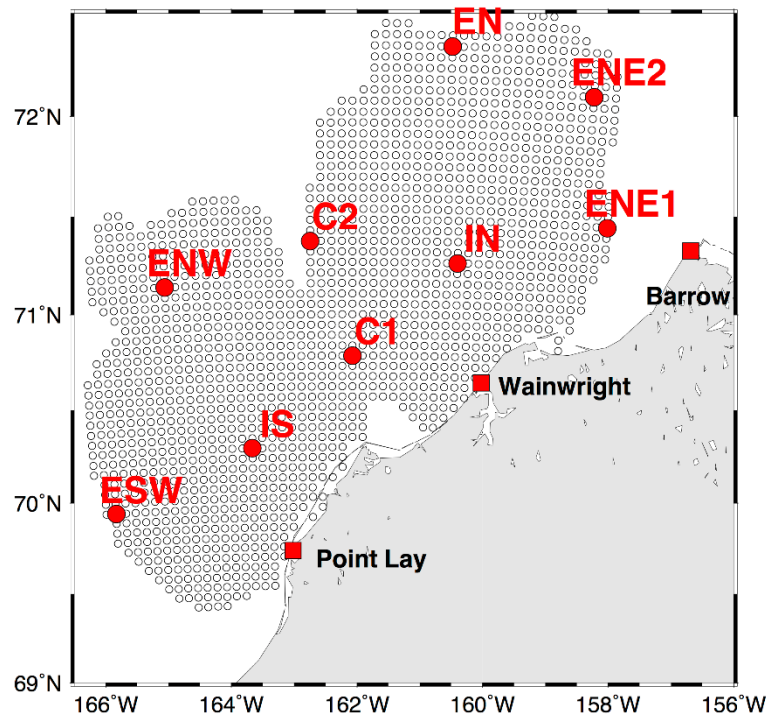
Figure 1.15. Gray circles are grid points for OI estimates. Red dots, enlarged for clarity, indicate locations of grid points for the gap sensitivity experiment. Red squares are the locations of HFR.
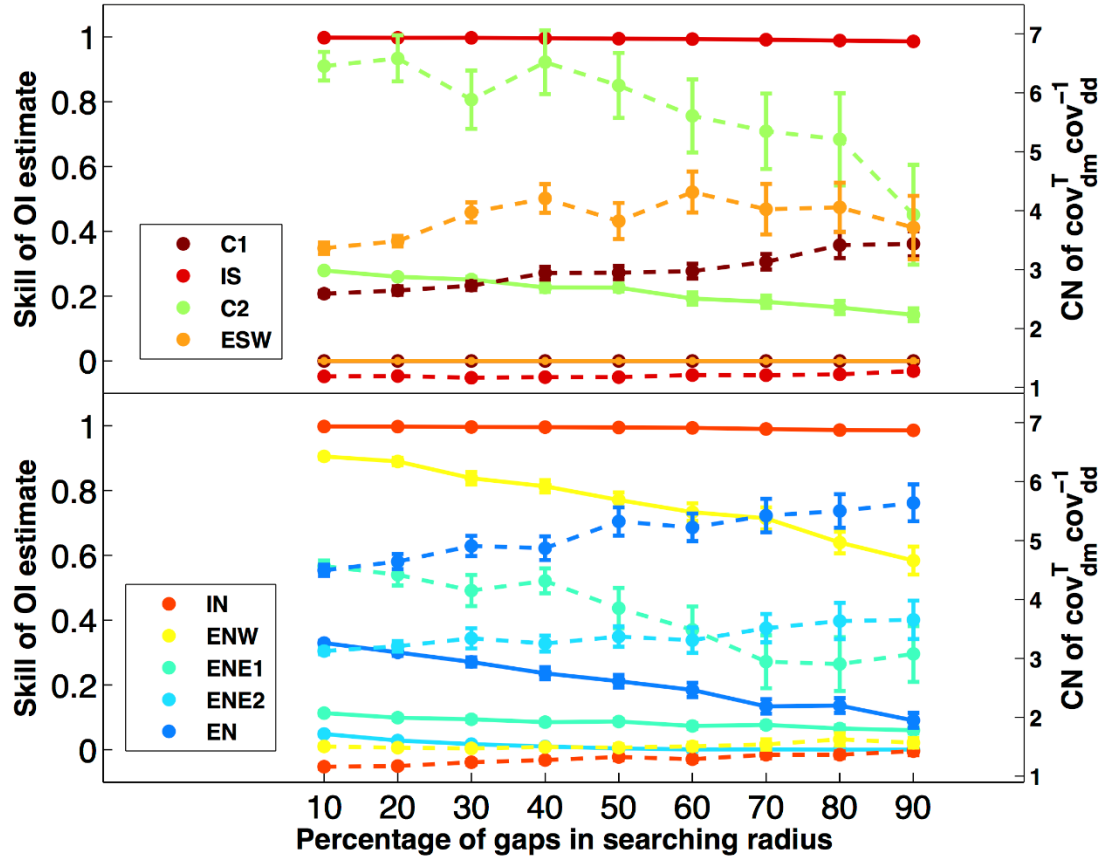
Figure 1.16. Variation in OI estimate skill (solid lines) and the condition number of $\mathrm{cov}_{dm}^{T}\,\mathrm{cov}_{dd}^{-1}$ (dashed lines) for varying gap percentages in the search radius. Vertical bars indicate the 95% confidence interval. Note that the skill lines for C1 and ESW are overlapped.

1.8 References

Arfken, G. B., H. Weber, and F. Harris, 2005: Mathematical Methods for Physicists 6th ED. Elsevier Academic Press, 1200 pp.

Barrick, D., and B. Lipa, 1986: Validation of HF radar measurements. *Ocean. Eng. IEEE J.*, **11**, 304–309.

Barrick, D., 2006: Geometrical Dilution of Statistical Accuracy (GDOSA) in Multi-Static HF Radar Networks. http://www.codar.com/images/about/2006Barrick_GDOSA.pdf

Barrick, D., V. Fernandez, M. I. Ferrer, C. Whelan, and Ø. Breivik, 2012: A short-term predictive system for surface currents from a rapidly deployed coastal HF radar network. *Ocean Dyn.*, **62**, 725–740, doi:10.1007/s10236-012-0521-0. http://link.springer.com/10.1007/s10236-012-0521-0.

Carter, E. F., and A. R. Robinson, 1987: Analysis Models for the Estimation of Oceanic Fields. *J. Atmos. Ocean. Technol.*, **4**, 49–74, doi:10.1175/1520-0426(1987)004<0049:AMFTEO>2.0.CO;2. http://dx.doi.org/10.1175/1520-0426(1987)004<0049:AMFTEO>2.0.CO.

Chapman, R. D., L. K. Shay, H. C. Graber, J. B. Edson, A. Karachintsev, C. L. Trump, and D. B. Ross, 1997: On the accuracy of HF radar surface current measurements: Intercomparisons with ship-based sensors. *J. Geophys. Res.*, **102**, 18737–18748, doi:10.1029/97JC00049. http://dx.doi.org/10.1029/97JC00049.

Crombie, D. D., 1955: Doppler spectrum of sea echo at 13.56 Mc./s. *Nature*, **175**, 681–682.

Fang, Y. C., J. Wang, Y. J. Yang., J. C. Mau, K. H. Thia, and M. J. Huang, 2011: Preliminary results of CODAR surface current observations northeast of Taiwan. *2011 International Workshop on Operating System for Marine Environment Monitoring and Forecasting*, Kaohsiung, Taiwan, 59-77.

Gurgel, K.-W., 1994: Shipborne measurement of surface current fields by HF radar. *OCEANS'94.'Oceans Engineering for Today's Technology and Tomorrow's Preservation.'Proceedings*, Vol. 3 of, IEEE, III–23.

Kim, S. Y., E. Terrill, and B. Cornuelle, 2007: Objectively mapping HF radar-derived surface current data using measured and idealized data covariance matrices. *J. Geophys. Res.*, **112**, C06021, doi:10.1029/2006JC003756. http://doi.wiley.com/10.1029/2006JC003756 (Accessed September 12, 2013).

——, E. J. Terrill, and B. D. Cornuelle, 2008: Mapping surface currents from HF radar radial velocity measurements using optimal interpolation. *J. Geophys. Res.*, **113**, C10023, doi:10.1029/2007JC004244. http://doi.wiley.com/10.1029/2007JC004244 (Accessed September 12, 2013).

Kohut, J., H. Roarty, E. Randall-Goodwin, S. Glenn, and C. S. Lichtenwalner, 2012: Evaluation of two algorithms for a network of coastal HF radars in the Mid-Atlantic Bight. *Ocean Dyn.*, **62**, 953–968, doi:10.1007/s10236-012-0533-9. http://link.springer.com/10.1007/s10236-012-0533-9 (Accessed September 12, 2013).

Kundu, P. K., 1976: Ekman Veering Observed near the Ocean Bottom. *J. Phys. Oceanogr.*, **6**, 238–242, doi:10.1175/1520-0485(1976)006<0238:EVONTO>2.0.CO;2. http://dx.doi.org/10.1175/1520-0485(1976)006<0238:EVONTO>2.0.CO.

Lipa, B., and D. Barrick, 1983: Least-squares methods for the extraction of surface currents from CODAR crossed-loop data: Application at ARSLOE. *Ocean. Eng. IEEE J.*, **8**, 226–253.

Lipa, B., 2003: Uncertainties in SeaSonde current velocities. *Proceedings of the IEE/OES Seventh Working Conference on Current Measurement Technology*, 95–100.

Liu, Y., R. H. Weisberg, C. R. Merz, S. Lichtenwalner, and G. J. Kirkpatrick, 2010: HF Radar Performance in a Low-Energy Environment: CODAR SeaSonde Experience on the West Florida Shelf*. *J. Atmos. Ocean. Technol.*, **27**, 1689–1710, doi:10.1175/2010JTECHO720.1. http://journals.ametsoc.org/doi/abs/10.1175/2010JTECHO720.1 (Accessed April 8, 2014).

Paquette, R. G., and R. H. Bourke, 1974: Observations on the coastal current of arctic Alaska. *J. Mar. Res.*, **32**, 195-207.

Shadden, S. C., F. Lekien, and J. E. Marsden, 2005: Definition and properties of Lagrangian coherent structures from finite-time Lyapunov exponents in two-dimensional aperiodic flows. *Phys. D Nonlinear Phenom.*, **212**, 271–304, doi:10.1016/j.physd.2005.10.007. http://linkinghub.elsevier.com/retrieve/pii/S0167278905004446 (Accessed August 7, 2013).

Shay, L. K., J. Martinez-Pedraja, T. M. Cook, B. K. Haus, and R. H. Weisberg, 2007: High-Frequency Radar Mapping of Surface Currents Using WERA. *J. Atmos. Ocean. Technol.*, **24**, 484–503, doi:10.1175/JTECH1985.1. http://journals.ametsoc.org/doi/abs/10.1175/JTECH1985.1 (Accessed March 29, 2014).

Stewart, R. H., and J. W. Joy, 1974: HF radio measurements of surface currents. *Deep Sea Res.*, **21**, 1039–1049.

Teague, C, 2001: Ionospheric Effects on Coastal Radar Systems. *Radiowave Oceanography the First International Workshop*, H.C. Graber and J. D. Paduan (ed.), 56-61.

Warner, J. C., W. R. Geyer, and J. A. Lerczak, 2005: Numerical modeling of an estuary: A comprehensive skill assessment. *J. Geophys. Res.*, **110**, C05001, doi:10.1029/2004JC002691. http://dx.doi.org/10.1029/2004JC002691.

Weingartner, T., S. Danielson, Y. Sasaki, V. Pavlov, and M. Kulakov, 1999: The Siberian Coastal Current: A wind- and buoyancy-forced Arctic coastal current. *J. Geophys. Res.*, **104**(C12),29697–29713, doi:10.1029/1999JC900161.

Weingartner, T., K. Aagaard, R. Woodgate, S. Danielson, Y. Sasaki, and D. Cavalieri, 2005: Circulation on the north central Chukchi Sea shelf. *Deep Sea Res. Part II Top. Stud. Oceanogr.*, **52**, 3150–3174, doi:10.1016/j.dsr2.2005.10.015. http://linkinghub.elsevier.com/retrieve/pii/S0967064505002158 (Accessed September 20, 2013).

Weingartner, T., P. Winsor, R. Potter, H. Statscewich, E. Dobbins, 2013: Application of High Frequency Radar to Potential Hydrocarbon Development Areas in the Northeast Chukchi Sea. *Final Report*, Contract No: M09AC15207, OCS Study BOEM 2012-079. www.data.boem.gov/PI/PDFImages/ESPIS/5/5266.pdf

Willmott, C. J., 1981: On the validation of models. *Phys. Geogr.*, **2**, 184–194.

Winsor, P., and D. C. Chapman, 2004: Pathways of Pacific water across the Chukchi Sea: A numerical model study. *J. Geophys. Res.*, **109**, C03002, doi:10.1029/2003JC001962. http://dx.doi.org/10.1029/2003JC001962.

Wunsch, C, 2006: Discrete Inverse and State Estimation Problems, Cambridge Univ. Press, 371 pp.

1.9 Appendices

Appendix 1.1. Permission from co-author Rachel Potter to include manuscript in the dissertation.

UNIVERSITY
of ALASKA

Ying Chih Fang <yfang2@alaska.edu>

Permission to use manuscripts in my dissertation

Rachel Potter <rapotter@alaska.edu>
To: Ying Chih Fang <yfang2@alaska.edu>

Wed, Oct 25, 2017 at 1:38 PM

Dear, Fang,

You certainly have my permission to include *Quality Assessment of HF Radar-Derived Surface Currents Using Optimal Interpolation* and *Surface Current Patterns in the Northeastern Chukchi Sea and Their Response to Wind Forcing* in your dissertation.

Thank you,
Rachel

_____

Rachel Potter
University of Alaska Fairbanks
College of Fisheries and Ocean Sciences
PO Box 757220
Fairbanks, AK 99775-7220
907-474-5709 (Phone)
http://www.uaf.edu/cfos/
http://www.chukchicurrents.com

[Quoted text hidden]

Appendix 1.2. Permission from co-author Hank Statscewich to include manuscript in the dissertation.

UNIVERSITY
of ALASKA

Ying Chih Fang <yfang2@alaska.edu>

Permission to use manuscripts in my dissertation

Hank Statscewich <hstatscewich@alaska.edu>   Wed, Oct 25, 2017 at 1:38 PM
To: Ying Chih Fang <yfang2@alaska.edu>
Cc: Rachel Potter <rapotter@alaska.edu>

Fang,
You have my permission to include these two papers as a part of your dissertation. Congratulations on completing your Ph.D!
Hank

On Wed, Oct 25, 2017 at 1:27 PM, Ying Chih Fang <yfang2@alaska.edu> wrote:
Hello Rachel and Hank,

You both are co-authors on two manuscripts that I want to include in my dissertation to fulfill the requirements of a PhD in Oceanography from the University of Alaska Fairbanks.

The first one is titled "QUALITY ASSESSMENT OF HF RADAR-DERIVED SURFACE CURRENTS USING OPTIMAL INTERPOLATION"; and the second one is titled "SURFACE CURRENT PATTERNS IN THE NORTHEASTERN CHUKCHI SEA AND THEIR RESPONSE TO WIND FORCING".

Please reply to this email and indicate whether you grant permission to include these 2 papers.

Thank you very much,
Fang
--

Ying-Chih Fang 方盈智

Graduate Student (Oceanography)

College of Fisheries and Ocean Sciences (CFOS)

University of Alaska Fairbanks

Fairbanks, Alaska, USA

E-mail: yfang2@alaska.edu

CHAPTER 2**:** Surface Current Patterns in the Northeastern Chukchi Sea and Their Response to Wind Forcing[2]

2.1 Abstract

We measured northeastern Chukchi Sea surface currents using high-frequency radar systems (HFR) during the ice-free periods of August to October from 2010–2014. We analyzed these data, along with regional winds, using Self-Organizing Maps (SOM) to develop a set of surface current-wind patterns. Temporal changes in the SOM patterns consist predominantly of two patterns comprising northeastward and southwestward surface currents. A third pattern represents a transitional stage established during the onset of strong northeasterly winds. These patterns are analogous to the first two eigenmodes of an empirical orthogonal function analysis of the HFR data. The first principal component (PC1) is significantly correlated (~0.8) to that of the winds and is directly related to the time series of SOM-derived patterns. The sign of PC1 changes when the speed of local northeasterly winds exceeds ~6 m s^{-1}, at which point the northeastward surface currents reverse to the southwest. This finding agrees with previous models and observations that suggest this wind threshold is needed to overcome the pressure gradient between the Pacific and Arctic Oceans. The transitional stage is characterized by alongshore currents bifurcating in the vicinity of Icy Cape and wind-driven Ekman currents north of 71.5°N. Its development is a manifestation of interactions amongst the poleward pressure gradient, wind stress, and geostrophic flow due to the coastal setdown.

2.2 Introduction

The Chukchi Sea is the gateway between the Pacific and Arctic Oceans. This vast marginal sea, though shallow in depth (~50 m), is prominent in shaping the thermohaline structure and freshwater budget of the western Arctic Ocean. The annual mean transport of Pacific water into the Chukchi Sea through Bering Strait is ~0.8 Sv (Woodgate et al. 2005; Roach et al. 1995) and was more recently reported as ~1.1 Sv (Woodgate et al. 2012), resulting

49

in a poleward flux of heat and freshwater that affects sea ice distributions (Woodgate et al. 2006; Shimada et al. 2006; Wood et al. 2015; Steele et al. 2008) and supplies ~30% of the freshwater input to the Arctic Ocean (Serreze et al. 2006). Although the northward transport is forced by the steric height difference between the Bering Sea and Arctic Ocean due to interbasin salinity differences (Stigebrandt 1984; Aagaard et al. 2006), the flow field varies due to atmospheric forcing (Woodgate et al. 2012; Danielson et al. 2014).

As Pacific waters flow northward through Bering Strait and across the Chukchi Sea, observations (Weingartner et al. 1998, 2005, 2013a; Pickart et al. 2010; Woodgate et al. 2005; Pickart et al. 2016; Paquette and Bourke 1981) and numerical models (Winsor and Chapman 2004; Spall 2007) indicate that the throughflow is bathymetrically steered along three major pathways (Figure 2.1). One branch follows Hope Valley and flows northward through Herald Canyon; another flows through the Central Channel between Herald and Hanna Shoals; and the third flows along the Alaskan coast and into Barrow Canyon where it becomes swift (~50 cm s^{-1}) and narrow (~40 km) (Winsor and Chapman 2004; Spall 2007; Itoh et al. 2013; Gong and Pickart 2015; Weingartner et al. 2017b). During summer and early fall, the coastal branch includes buoyant, nutrient poor Alaskan Coastal Water, carried by the Alaskan Coastal Current (ACC) (Paquette and Bourke 1974). Itoh et al. (2013) used long-term mooring observations at the mouth of Barrow Canyon and found the greatest heat and freshwater fluxes occur from August to October.

Owing to the shallowness of the Chukchi shelf, wind forcing substantially influences the circulation pathways. On average, each branch flows poleward, whereas the mean wind field over the Chukchi shelf is from the east-northeast (Weingartner et al. 2013a) and opposes the mean flow. Local winds are highly correlated with the flow field on the Chukchi shelf (Weingartner et al. 2005; Itoh et al. 2013), except in Herald Canyon (Woodgate et al. 2005). Winsor and Chapman (2004) used a barotropic model to examine the sensitivity of shelf flow under changing winds and found that when northeasterly winds exceeded ~6 m s^{-1}, the coastal current near Barrow reversed to the southwest. Similar reversals were observed using subsurface moorings and ship-borne surveys (Mountain et al. 1976; Aagaard and Roach 1990; Johnson 1989; Okkonen et al. 2009; Weingartner et al. 1998; Hirano et al. 2016); however subsurface measurements do not capture the upper few meters and so may not be representative of the

50

surface current field. Therefore, surface current observations are essential to evaluate the flow imposed by wind forcing, especially when considering the potential transport of surface-trapped dissolved and suspended materials. In particular, surface currents may be important in the distribution of fish larvae (Wyllie-Echeverria et al. 1992; Geoffroy et al. 2016) and zooplankton (Questel et al. 2013).

This study focuses on synoptic surface current measurements collected in the northeastern Chukchi Sea using shore-based high-frequency radar systems (HFR) deployed along the Alaskan coast in the villages of Barrow, Wainwright, and Point Lay during the open-water seasons of 2010–2014 (Figure 2.1). The HFR measurements have a resolution of 6 km and a range of ~150 km from the coast. We investigate the relationship between surface currents and winds using Self-Organizing Maps (SOM) (Kohonen 2001) to extract surface current patterns paired with wind fields.

The paper is arranged as follows. The HFR and North American Regional Reanalysis (NARR) data acquisition and processing are discussed in Section 2.3, followed by an overview and methodology of the SOM analysis. Section 2.4 presents the SOM-derived patterns, including their temporal evolutions in response to the winds. Surface current patterns from conventional empirical orthogonal function (EOF) analysis are also discussed. These results, along with mean circulation patterns, spatial correlations, and hydrographic observations, suggest differing dynamical environments north and south of ~71.5°N. Section 2.5 discusses the results with the aid of the regional hydrographic setting, and Section 2.6 summarizes the paper.

2.3 Data and Method

2.3.1 Surface currents

A three-HFR network monitored surface currents (~2 m depth, Stewart and Joy, 1974) in the northeastern Chukchi Sea (Figure 2.1a) using 5-MHz SeaSonde systems. This frequency requires the presence of surface gravity waves with wavelengths of ~30 m (Barrick 1978; Paduan and Washburn 2013) and thus sufficient ice-free waters and winds to generate such waves. The SeaSonde records the reflected Bragg scatter from the waves, after which, assuming deep-water wave theory, one uses the Doppler-shifted radar return to calculate surface current speeds

advancing toward or retreating from the radar. The HFR network presented herein is unique in that it is operated in a polar environment where waters are ice-covered ~8 months of the year. Sea ice presence varies from year-to-year and contaminates the radar signals. Therefore, we only considered the time period from 1 August to 31 October of each year, when little or no sea ice was present within the radar mask. The HFR site locations were dictated by grid power availability, which necessitated that our sites be more broadly separated (~150 km) than optimal (~75 km). Thus, the resultant radar coverage comprises two domains: a southern mask (Point Lay and Wainwright overlap) and a northern mask (Barrow and Wainwright overlap). The coverage leaves a persistent gap along ~162.5°W (Figure 2.1a). Although data from 2010–2014 were analyzed, we primarily present results from 2012 when spatial coverage was most extensive.

One-dimensional radial surface currents, $\vec{r}$, from each HFR were used to estimate two-dimensional surface currents, $\vec{u}$, following the optimal interpolation (OI) scheme of Kim et al. (2007, 2008). Fang et al. (2015) investigated the performance of the OI method applied to the Chukchi HFR network. They used analytical streamfunctions to simulate spatially and temporally varying currents and found that for derived $\vec{u}$ with a normalized skill ≥0.7 (0–1 scale), errors were ~2° angle shift and <0.1% magnitude variation. They found that the most important quality control factor for the estimated $\vec{u}$ is the contribution of radial velocities from different HFR, which is defined as the ratio of overlapping $\vec{r}$ (ROR). The higher the ROR, the more biased the estimate of $\vec{u}$, by as much as ~20° in angle shift with a corresponding ~6% change in magnitude.

The $\vec{u}$ were computed every cardinal hour, and the ROR at each grid point was determined. Fang et al. (2015) show that areas with ≥0.7 skill closely coincide to those with ROR <~5, thus grid points with ROR ≥5 were discarded. In addition, if the number of contributing $\vec{r}$ in the search radius (35 km) of the grid point was <20, the OI-output $\vec{u}$ at the grid point was flagged. The threshold 20 was used to prevent $\vec{u}$ from being calculated using a small number of $\vec{r}$, which can result in erroneous current estimates. For the OI scheme we employed criterion based on the cosine angle of paired $\vec{r}$ (Chavanne et al. 2007) to avoid estimates along the radar baseline where $\vec{u}$ cannot be properly resolved. If the angle between paired $\vec{r}$ was not between 30–120°, the grid point was excluded from the analysis. This range was chosen in

conjunction with other quality control factors reported in Fang et al. (2015) to allow optimal determination of $\vec{u}$.

Data gaps can degrade filtering quality and cause spectral leakage that dampens filtered results, so after some experimentation, gaps in the $\vec{u}$ time series for each year were filled with zeros following Chavanne et al. (2007). Grid points containing $\geq 60\%$ temporal coverage (Figure 2.1a) were then filtered with a 9th order 40-h cutoff low-pass Butterworth filter to remove high frequency signals (tidal and inertial motions).

2.3.2 Winds

Wind velocities were extracted from the NARR 10-m surface field (Mesinger et al. 2006), at ~35 km grid-spacing every 3 hours, for the same period as the HFR data and then linearly interpolated to hourly intervals and filtered as described above. Quantitative comparisons between the NARR winds and those measured at the Barrow and Wainwright airports were conducted in Weingartner et al. (2013b), who determined that NARR winds are a reliable proxy for observed winds. A domain covering the radar mask (Figure 2.1a) is used for the SOM and EOF analyses with 162.1°W, 71.2°N (red triangle in Figure 2.1a) chosen as representative of winds in the study area.

2.3.3 SOM analysis

SOM is a tool capable of capturing detailed synoptic variability in a data set through time with multiple variables. Richardson et al. (2003) and Liu and Weisberg (2005) provide excellent background on the application of SOM to oceanographic data. Liu et al. (2006) investigated SOM sensitivities to varying parameter choices and discussed its performance compared with EOF analysis. Ideally, the major circulation features derived from both methods should be consistent with one another. However, Liu et al. (2006) showed that EOFs failed to extract predefined patterns from synthetic data, whereas SOM completed the task perfectly. The advantage of using SOM, a nonlinear approach, compared with EOFs for HFR currents is the capability to extract detailed patterns from synoptic data sets Mau et al. (2007) and to identify when they occur in time. As will be shown, higher order EOF eigenmodes may not correctly capture complicated patterns.

We used the SOM Toolbox for our analysis (http://www.cis.hut.fi/somtoolbox/; v. 2.0) and followed the parameters discussed in Liu et al. (2006). As shown by Liu et al. (2007), Mihanović et al. (2011), and Vilibić et al. (2016), SOM is capable of incorporating two different data sets (e.g., HFR and wind data) to resolve associated patterns. Gap-filling approaches have been developed for HFR data (Kaplan and Lekien 2007; Fredj et al. 2016), but these tend to produce spurious results during periods of sparse data returns. Therefore, we replace HFR data gaps with zeros rather than using gap-filling approaches. This procedure makes the linear initialization of SOM numerically valid, so that the first two eigenmodes of the data matrix can be determined (Kohonen 2001). Beckers and Rixen (2003) found that introducing zeros into the raw data matrix can increase the variance of dominant modes and reduce errant interpolations.

The resultant number of patterns produced by SOM has to be chosen *a priori* and is subjective. The larger this number, the more temporal variability will be extracted from the data, while a smaller number of patterns tends to compress information yielding less temporal variability (Liu et al. 2006). After experimentation, we found that twelve patterns are optimal for our data in that unique circulation features and data gaps can be isolated.

Twelve patterns were derived each year for 2010–2014. Although winds, radar coverage, and data gaps differed from year-to-year, we were able to categorize similar patterns into four major flow regimes (see Section 2.4.1). SOM patterns were visually confirmed with the data time series in each year to verify SOM performance. There was a pattern in all years made up of weak or negligible currents. We show that this weak current pattern correlates with a decrease in data returns (see Section 2.4.2) and can be treated as an error analog that facilitates our interpretation of resultant time series.

2.3.4 EOF analysis

EOF analysis provides another perspective of surface current responses to winds. We will show that the first eigenmode and its principal component (PC1) corroborate the SOM-derived patterns. Due to data gaps, a direct EOF computation for $\vec{u}$ was not possible; therefore, a field reconstructed approach called data interpolating empirical orthogonal functions (DINEOF) (Beckers and Rixen 2003; Taylor et al. 2013) was used to fill data gaps. (In August 2010 and

2013, there were too many $\vec{u}$ gaps for effective use of the DINEOF approach, so the 1 September to 31 October period was used.) Reconstructed $\vec{u}$ and wind time series for each year were then used individually for the EOF analysis following Kaihatu et al. (1998), resulting in two covariance matrices per year. Each EOF analysis yielded a corresponding PC, which we used to diagnose the flow fields. The resultant eigenvalue spectrum was evaluated according to North's significance test (North et al. 1982).

2.3.5 Hydrography

We used temperature and salinity data collected by a SeaBird 49 FastCAT CTD housed in a towed Acrobat system to highlight different hydrographic environments north and south of ~71.5°N. One transect started from the western flank of Hanna Shoal and ran southeastward for ~200 km to offshore Point Franklin, while a second began west of Wainwright near ~164°W and ran ~200 km northeastward to the northern edge of Hanna Shoal (Figure 2.1a). The Acrobat-CTD sampled water depths of up to ~45 m with horizontal and vertical resolutions of ~250 m and ~0.5 m, respectively. Details on instrumentation, data acquisition, and processing are given by Martini et al. (2016).

2.3.6 Subsurface currents

An ADCP mooring near the head of Barrow Canyon (BC2; nominal 52.3 m depth) monitored transport through Barrow Canyon and was maintained from 2010–2015 (Figure 2.1a). These data allow us to compare flow behaviors throughout the water column. We used hourly time series of estimated alongcanyon transports following Weingartner et al. (2017b) and vertically averaged velocities to examine subsurface to surface current variations. Data processing of BC2 is found in Weingartner et al. (2017b).

2.4 Results

2.4.1 SOM-derived Patterns

All twelve SOM-derived patterns for 2012 data with paired wind conditions are presented in the supporting information (see Figure A2.1 and Table A2.1 in Appendix 2.1). To simplify the

presentation, we condense the twelve into four representative flow regimes (Figure 2.2a-d), along with polar histograms of accompanying wind conditions. The northeastward-flowing regime is the most common pattern (Figure 2.2a) and defined on the basis of northeastward flow inshore or near the 40 m isobath in the southern mask and in Barrow Canyon in the northern mask. For this regime the flow is coastally-intensified with speeds >30 cm s^{-1} in the canyon and within ~70 km of the coast in the southern mask. Currents are weak over the central shelf (<20 cm s^{-1}) and even weaker (~5 cm s^{-1}) north of 71.5°N. The northeastward-flowing regime occurred ~53% of the time, and ~76% of the winds associated with this pattern have a southerly component. Less than 10% of the winds are northeasterly with wind speeds <~6 m s^{-1}, suggesting that under these wind conditions the flow is forced primarily by the poleward pressure gradient. Velocity measurements from the BC2 mooring indicate the subsurface flow is also primarily northeastward under these conditions. Coincident southwestward subsurface currents are remnant from flow transitions that have not been fully completed and lag the surface flow. Weingartner et al. (2017b) suggest an adjustment time scale of ~1 day for the vertically-averaged flow in Barrow Canyon.

The second most common circulation feature is the reversal regime (Figure 2.2b), which occurred ~11% of the time and whose structure is nearly opposite the northeastward-flowing regime. It consists of southwestward flow nearshore and westward flow farther offshore. The wind histogram shows ~60% of the associated winds are northeasterly at >6 m s^{-1} with ~10% of occurrences associated with northerly winds with speeds >6 m s^{-1}. Reversal regime currents are stronger than those for the other circulation patterns, with current speeds >30 cm s^{-1} in Barrow Canyon and inshore of the 40 m isobath offshore of Point Lay. Currents north of 71.5°N and east of Hanna Shoal are also swifter (~15 cm s^{-1}) for this regime compared to the northeastward-flowing regime. Southwestward surface flow at BC2 predominates during the reversal regime. The occurrence of subsurface northeastward currents during the reversal regime is again due to

the adjustment time from surface to depth. This result indicates that, at the head of Barrow Canyon, the flow structure is coherent vertically during the two most common surface circulation patterns but that the vertical shear may be substantial during flow transitions.

The third regime occurred ~16% of the time and is denoted as the northwesterly wind regime (Figure 2.2c). For this pattern ~90% of the winds are northwesterly, with more than half of the wind events having speeds >6 m s^{-1}. This regime appears to result from interactions between the poleward pressure gradient (northeastward flow) and wind-induced Ekman transport (southward flow). The flow field appears to be spatially variable depending on which driving force dominates. For example, when winds initially shift to the northwesterly quadrant, the resultant Ekman transport may not be large enough to overcome the background pressure gradient. We have found cases where the currents south of 71.5°N are east-northeastward (similar to those seen in the northeastward-flowing regime) but southward north of 71.5°N. This flow pattern develops under evolving northwesterly winds and may last longer than a day. As northwesterly winds persist, the Ekman currents gradually overwhelm the poleward pressure gradient, so that currents are southward at ~10–15 cm s^{-1} over much of the radar mask, with stronger flows (~20 cm s^{-1}) inshore of the 40 m isobath and southeast of Hanna Shoal.

Subsurface flows observed at BC2 indicate predominately northeastward currents, indicating that the flow was vertically sheared over much of the canyon, except near Point Franklin where the surface flow was still northeastward. This finding implies that the subsurface flow over the central shelf must have been onshore in order to feed the transport in Barrow Canyon. This current pattern differs from the reversal regime, during which both the subsurface and surface flows were southwestward.

The fourth regime is the divergent mode (Figure 2.2d). North of 71.5°N, currents are ~10 cm s^{-1} and westward. South of this latitude, a recirculation is suggested, which includes cyclonic flow near the head of Barrow Canyon and an anticyclonic circulation at ~164°W, 70.5°N. The recirculation includes northeastward currents near the head of Barrow Canyon and southwestward currents in the southern mask between Icy Cape and Point Lay. Approximately 80% of the winds concurrent with the divergent mode are northeasterly, and ~70% of these winds have speeds >6 m s^{-1}, similar to those of the reversal regime; however, the subsurface and surface flow at BC2 is still northeastward, in contrast to the reversal regime. We will demonstrate that the divergent mode is a transitional stage between the northeastward-flowing and reversal regimes, as northeasterly winds begin to overcome the poleward pressure gradient.

As previously mentioned in Section 2.3.3, SOM patterns vary slightly over the years; however, the regime descriptions above apply to all years. For example, the reversal regimes of 2010, 2011, 2013, and 2014 are all analogous to our description for the reversal regime in 2012. We find that the location of southwestward flow, offshore westward flow, and subsurface currents observed at BC2 approximate to the 2012 results. Similar agreements apply to the other three flow regimes.

Histograms show the monthly distribution of the four flow regimes for all years (Figure 2.3). The results indicate that the northwesterly wind regime was rare, consistent with the regional mean winds being predominantly from the east-northeast. The northeastward-flowing and reversal regimes occurred ~43% and ~27% of the time, respectively. In general, as the frequency of the northeastward-flowing regime increases the frequency of the reversal pattern decreases, and vice-versa. The divergent mode appeared ~7% of the time overall with durations varying from several hours to a maximum of ~5 days.

The remaining pattern, not included in our categorization, consists of variable and weak (~1 cm s^{-1}) currents which are unreliable and occurred during periods of sparse data returns due to equipment maintenance, ice, ionospheric interference, and/or low winds. Collectively these conditions occurred ~14% of the time during 2012 and were aggregated into a pattern for data gaps referred to as G.

2.4.2 The role of winds: SOM perspective

To illustrate how surface currents change under varying wind conditions, time series of the SOM regimes from August through October 2012, along with wind vectors, are presented in Figure 2.4. (The original time series of all 12 SOM-derived patterns are presented in Figure A2.2.) The gray line in Figure 2.4 tracks the normalized data return and facilitates interpretation of regimes associated with data gaps. For example, Pattern G occurred from 11 to 14 August when data returns were very low. Low data returns also occurred from 10 to 14 October due to diurnal ionospheric interference (Teague 2001).

The wind field from 4–28 August was mainly southwesterly-southerly, and the northeastward-flowing regime persisted through most of the month. It was also present during

the southerly wind events of 1–3, 6–7, and 20–28 October and occurred from 1–3 August and from 18–22 September when weak ($\leq$4 m s^{-1}) winds from varying directions prevailed, consistent with our notion that weak winds are insufficient to overcome the poleward pressure gradient force.

After 28 August, southerly winds relaxed, and the winds became northeasterly and increased to a maximum of 10 m s^{-1} on 31 August. During this wind transition, the circulation shifted briefly into the divergent mode before the reversal regime was established. Reversal regimes consistently occurred during and/or shortly after pulses of strong (~10 m s^{-1}) northerly and/or northeasterly winds (e.g., 16–17, 22–23, and 27–29 September and 30–31 October). The divergent mode accompanied each transition from the northeastward-flowing regime to the reversal pattern, appearing as the northeasterly winds increased to relatively high magnitudes. Based on the wind time series and the EOF analysis of Section 2.4, we find that the divergent mode occurred when northeasterly winds reached ~6 m s^{-1}. Hence, the divergent mode appears to be a transition between these two regimes; a point we will return to in Section 2.5.

The northwesterly wind regime (Figure 2.2c) occurs primarily during periods when winds are veering from northwesterly to westerly or vice versa (e.g., 8–18 October) and/or during wind transitions involving westerlies (14–15 September). These results suggest that strong (>6 m s^{-1}) and sustained northwesterly winds (>1 day) are required to initiate this regime. We did not observe this pattern in 2011 and 2013, however, because northwesterly winds seldom occurred. When present, these events were short-lived (<1 day) in comparison to the >3 day events registered in 2012.

2.4.3 The role of winds: EOF perspective

The bulk of the SOM patterns are the northeastward-flowing and reversal regimes, which suggests that these should be linked to the leading EOFs (Mau et al. 2007). In this section, we use EOFs and SOM patterns to corroborate one another. Table 2.1 summarizes the EOF results in terms of the variance explained by the first (Mode 1) and second eigenmodes (Mode 2), the number of significant eigenmodes, and the correlation between PC1 of the currents and the winds. Mode 1 of the currents and winds account for at least 50% of the total variance, and the

correlation between each variable's PC1 is significant. Mode 1 of the 2012 surface currents (Figure 2.5a) shows a pattern similar to the reversal regime derived from SOM (Figure 2.2b), which, when multiplied by its negative weight in the time domain, is analogous to the northeastward-flowing regime (Figure 2.2a). Mode 1 of the winds depicts northeasterlies (Figure 2.5c), and its negative weight describes southwesterly winds. The structures of Mode 1 in other years were similar to those in 2012, except in 2010 when Mode 1 for the winds was aligned in the east-west direction.

Mode 2 of the currents, which accounts for 9% to 17% (depending upon year) of the surface current variance, is characterized by southward flows and onshore currents that appear to bifurcate somewhere between Icy Cape and Wainwright (Figure 2.5b). Meanwhile, Mode 2 of the winds portrays northwesterlies (Figure 2.5d) and explains 19% to 34% of the variance across years. The structure of Mode 2 of the currents and winds in other years is comparable to those from 2012. The correlation between the principal components of Mode 2 (PC2) of the currents and the winds is only statistically significant for 2012 and 2014; however, as discussed later, we suspect that this relationship may not be meaningful.

Figure 2.6 shows the relationship between currents and winds in terms of wind speed and direction, PC1 of currents and winds, and the circulation regimes for the 2012 data. PC1 of currents and winds are normalized individually, and both are referenced to the reversal regime and northeasterly winds. PC1 values for the currents (winds) approaching unity indicate a flow field similar to that of Mode 1 (Figure 2.5a). In August, PC1 of the currents and winds were both generally negative (i.e., northeastward flow), consistent with the SOM results.

Northeasterly and northerly winds, as well as the divergent mode and reversal regime, were more frequent in September and October than in August. As a consequence positive PC1 values for both the currents and winds were also more frequent. For example, the winds were northeasterly at ~6 m s^{-1} throughout 10–13 September, when the pattern corresponded to the divergent mode (indicated by a red arrow, Figure 2.6). During this period, the current PC1 was ~0.1, indicating the flow field had not yet fully reversed, consistent with the SOM analysis. Therefore, the EOF analysis corroborates the SOM conclusion that northeasterly winds ≥6 m s^{-1}

60

are critical in shifting the surface circulation through the divergent mode and toward the reversal regime.

We examined four selected periods (labeled T1–T4, Figure 2.6) in September that consisted of reversal regimes. Periods T1–T3 had northeasterly winds >6 m s^{-1} (i.e., the wind PC1 had values >0.5). Each event was preceded by periods of weaker winds from varying directions. The current PC1 evolved similarly as its values changed from negative to positive. The temporal evolution of PC1 during each of these periods suggests that the reversals lagged the winds by 6–9 hours. Period T4 also corresponded to the reversal regime, when winds were northerly with speeds >~6 m s^{-1}. Each of these reversals coincided with southwestward or upcanyon transports of ~1 Sv as measured by BC2 (Weingartner et al. 2017b).

The PC1 values for the currents fluctuate when the northwesterly wind regime is present (e.g., 9–18 October) but are comparatively small (≤±0.2). The northwesterly wind regime events are not well-described by the evolution of PC1 because their overall flow behaviors are different from those associated with Mode 1.

Unlike the good correspondence between the evolution of PC1 and the SOM-flow regimes, we do not find a direct relationship between PC2 and the flow regimes. For example, high positive PC2 (~0.8) for winds and currents were found in August, but the observed winds and flow fields were predominately southerly and northeastward, respectively. We suspect that EOF Mode 2 of winds and currents is a consequence of the orthogonality requirement of the EOFs computation and thus a limitation of EOFs. Our results suggest that higher order eigenmodes should be interpreted cautiously for data sets containing large variability.

2.4.4 Mean circulation patterns

We formed composite circulation maps for periods when the HFR data recorded downcanyon (northeastward) and upcanyon (southwestward) flow events for 2010–2014 (Figure 2.7). The classifications were defined by average flow conditions derived from twelve HFR grids (Figure 2.1b) near the head of Barrow Canyon. For the downcanyon condition flow is defined to be toward 56°T±4°, while for the upcanyon condition it is toward 236°T±4°, with 56°T the approximate axis of Barrow Canyon. Mean downcanyon and upcanyon patterns observed by

HFR are comparable with the SOM-derived northeastward-flowing and reversal regimes, respectively.

For the 5-year period, we found 868 hourly surface current observations satisfying our downcanyon criterion. The polar histogram indicates that ~75% of the time the downcanyon pattern occurs under variable wind directions at moderate wind speeds (≤6 m s^{-1}). Approximately 25% of the winds were northeasterly (203–246°T), with only 5% of those >6 m s^{-1}. These strong northeasterlies are the catalyst for a reversal to upcanyon flow, and thus indicate when the flow field lagged the wind. The downcanyon average suggests four distinct flow regions (Figure 2.7a; labeled 1–4) under mean winds of ~1 m s^{-1} westward (~264°T). Region 1 lies north of 71.5°N on the eastern flank of Hanna Shoal, and here the mean currents are weak (a few cm s^{-1}) and directionally variable. The flow in Region 2 is generally eastward with mean currents 5–10 cm s^{-1}, consistent with results from moorings, ship-borne surveys, and models (Weingartner et al. 2005; Gong and Pickart 2015; Winsor and Chapman 2004; Spall 2007). In the northwestern part of Region 2 the flow is southeastward, suggestive of flow moving eastward from the Central Channel across the shelf south of Hanna Shoal. Region 3 encompasses the head of Barrow Canyon, where mean currents are northeastward and swift (~30 cm s^{-1}). The mean currents in Region 4, which covers the southern portion of the southern radar mask, are northeastward at ~10 cm s^{-1}. The downcanyon average suggests convergence of the nearshore flow with that from the central shelf near 70.8°N, 162.5°W, with current speeds increasing as these flows converge.

Observations consistent with the upcanyon criterion were fewer, with only 368 hourly values. Mean winds for the upcanyon composite (Figure 2.7b) were ~7 m s^{-1} toward ~236°T, consistent with the reversal regime. Winds were ~70% northeasterly, ~6% northerly, and ~11% easterly. Overall the currents are stronger than those of the downcanyon average. Surface currents in Region 1 are westward at ~9 cm s^{-1}, diminishing northward, while currents in Region 2 are westward or northwestward at 15–20 cm s^{-1}, which could carry canyon waters toward the south side of Hanna Shoal and across the central shelf. Currents near Barrow Canyon (Region 3) are particularly strong, with a mean of ~50 cm s^{-1} to the southwest (~240°T). The flow in Region 4 is also southwestward (~240°T) but with speeds of ~20 cm s^{-1}.

The composites indicate that the down- and upcanyon flow structures in Regions 2 and 3 are mirror images of each other; however, Regions 1 and 4 are quite different from one another. For the upcanyon case, in Region 1 the flow is westward and oriented ~35° to the right of the wind. For the downcanyon case the surface currents are weak and variable. We show later that the surface flow in Region 1 is consistent with Ekman dynamics.

For the Region 4 downcanyon case, the mean current speed is maximum (~25 cm s^{-1}) over the 40 m isobath and not statistically different ($p<0.05$) from the speed over the 30 m isobaths, but in the upcanyon case, the mean speeds along these isobaths are significantly different from one another. It is maximum (~38 cm s^{-1}) over the 30 m isobath and monotonically decreases offshore with the flow being ~32 cm s^{-1} over the 40 m isobath. These differences imply an asymmetry in the alongshore transport, with more transport carried by the inner shelf flow during upcanyon events compared to downcanyon cases. In the upcanyon case, the alongshore winds cause a sea level setdown and an alongshore southwestward flow established by the cross-shore pressure gradient. This gradient should be greatest within ~50 km of the coast, which is the e-folding scale for the 140 km barotropic radius of deformation (for a shelf depth of 40 m). In the downcanyon mean the winds are weak and directed offshore, in which case the mean flow is largely forced by the poleward pressure field and appears strongest over the 40 m isobath. This suggestion is consistent with the convergence in modeled streamlines shown by Winsor and Chapman (2004) and Spall (2007) for the same region.

2.4.5 Spatial correlation structure

In this section we use the complex correlation function (Kundu and Allen 1976) to examine the spatial correlation structure of the down- and upcanyon flows using the DINEOF reconstructed data. The calculations use two reference grid points. The first, at 71.2°N, 160°W, is chosen to examine relationships between flow near Barrow Canyon and those elsewhere. The second grid point, at 72°N, 160°W, is over Hanna Shoal.

Based on the sample number (1148 for downcanyon; 249 for upcanyon) and estimated integral time scale (~40 hour) from the 2012 DINEOF field, the 95% significance levels for the down- and upcanyon correlations are 0.36 and 0.71, respectively. The correlation field using the

Barrow Canyon grid point is similar for both flows (Figures 2.8a-b), with correlations high in the canyon and across the southern mask but much smaller north of 71.5°N. The correlated regions are quite large. For example, the largest distance between grid points with correlations ≥0.8 is ~170 km for the downcanyon case and ~300 km for the upcanyon.

Using the Hanna Shoal grid point, the well-correlated region is limited to the area north of 71.5°N for the downcanyon case (Figure 2.8c). The length scale of the strongest correlation is only ~30 km, as expected given that the contributing currents are weak and variable in this region (Figure 2.7a). For the upcanyon case (Figure 2.8d), the spatial correlation structure is again significant and mainly confined to the region north of 71.5°N over a length scale of ~120 km. In aggregate, the SOM and the mean and correlation fields indicate that the shelf circulation north of 71.5°N is dynamically different from the shelf to the south.

2.5 Discussion

Our analyses have revealed two major surface circulation regimes related to the local winds. The northeastward-flowing regime transports water from along the coast and the central shelf into Barrow Canyon and toward the Arctic Ocean. During summer and early fall, this surface transport involves warm, low-salinity coastal waters and somewhat more saline waters from the central shelf. The reversal regime transports waters up the canyon and across the Chukchi shelf, suggesting upwelling within the canyon and along the west coast of Alaska. We also identified the divergent mode, a transitional flow field established as northeasterly winds intensify, which eventually evolves into the reversal regime. This mode includes divergence in the nearshore currents between Icy Cape and Wainwright, with one branch leading into Barrow Canyon and the other proceeding southwestward. In addition, we found that the currents north of 71.5°N (Region 1 in Figure 2.7) are distinctly different from the currents south of this latitude. We explore these findings in greater detail in the following paragraphs.

In summer and fall, a portion of the Bering Strait inflow is carried eastward from the Central Channel and merges with ACC waters as they approach Barrow Canyon. This eastward flow is represented in circulation models forced solely by the poleward pressure gradient (Winsor and Chapman 2004; Spall 2007), in prior observations (Weingartner et al. 2005, 2013a),

and is largely consistent with the northeastward-flowing regime (Figure 2.2a) and observed downcanyon mean (Figure 2.7a). The models also indicate that some of the Central Channel transport flows geostrophically around the north side of Hanna Shoal. Along the east side of the shoal the modeled flow is southward before turning eastward into the head of Barrow Canyon. This southward flow is much weaker than that on the western side because the isobaths diverge on the northeast side of the Shoal. However, the modeled southward flow is not captured by the SOM, nor is it evident in the vertically-averaged mean flows estimated from moorings on the shelf east of Hanna Shoal (Weingartner et al. 2017a).

We believe that one cause in the differences in surface circulation north and south of 71.5°N lies with the shelf hydrographic structure. Figure 2.9 shows vertical sections of potential temperature (θ) and salinity (S) along Legs 1 and 2 (Figure 2.1) from September 2013. In both sections waters deeper than ~20 m were cold (<-1°C) and salty (≥32.5) winter waters. North of 71.5°N a ~15-m deep surface layer contained cool (0°C) and fresh (salinity ~26–29) meltwaters underlain by a thin but strong pycnocline. South of 71.5°N the stratification was weaker and the surface waters were warmer (3–5°C), moderately salty (salinity ~31), and derived from Bering Sea summer waters. The front delineating these surface water masses was centered near 71.5°N. Similar fronts around this latitude are apparent in sections shown by Lu et al. (2015) and (Weingartner et al. 2017a). The latter find that the shelf north of 71.5°N and east of Hanna Shoal supports a counterclockwise baroclinic geostrophic flow component that opposes the modeled barotropic flow around the Shoal. These opposing pressure tendencies result in weak geostrophic flow.

We suggest that the strong stratification north of 71.5°N in conjunction with weak geostrophic flow suggests that the surface currents in this region are largely governed by Ekman dynamics, with the Ekman layer presumably confined to the upper 15 m. For the upcanyon case, the mean winds were ~7 m s^{-1} toward ~236°T, which would impel a mean flow in the upper 15 m of ~6 cm s^{-1} toward 326°T. The observed flow (within the upper 2 m) averaged 9 cm s^{-1} toward 270°T (i.e., ~34° to the right of the wind). As discussed in Dzwonkowski et al. (2011), baroclinic shear and stratification inhibit deepening of the surface boundary layer and reduce its interaction with the bottom boundary layer, resulting in enhancement of surface transport. South

of 71.5°N the stratification is weaker and the flow is primarily barotropic and geostrophic (Weingartner et al. 2013a), so that wind momentum is diffused over much of the water column.

We next examine the dynamics associated with the divergent mode aided by snapshots of wind and surface current maps (Figure 2.10) from September 2011. The maps encompass a period when the winds transitioned from southerly (12 September, Figure 2.10a) to strong northeasterly (15–19 September; Figure 2.10b-d). Each map includes a vector showing the wind at the measurement time (black) along with the wind vectors for the preceding 12 (dark gray) and 24 hours (light gray).

Prior to 12 September the winds were southwesterly, and the northeastward-flowing regime held. At this time both the poleward pressure gradient and the coastal sea level setup acted in concert to propel the flow. On 13 September (not shown), the winds became east-northeasterly, and the divergent mode appeared for the next few days (Figures 2.10b). This transitional mode consisted of westward Ekman drift north of ~71.5°N and southwestward alongshore flow inshore of the 30 m isobath offshore of Point Lay. The time scales for the appearance of these two circulation features is plausible. The Ekman adjustment time scale is only a few hours (Allen 1973), whereas the spinup time scale for the alongshore flow is proportional to h/r, where h is the water depth and r is the linear bottom friction coefficient. The adjustment to southwestward flow in the shallow (<30 m) nearshore waters should be ≤0.5 day for r ~5 x 10^{-4} m s^{-1} (e.g., Brink 1998) but longer in deeper waters. Apparently there is a ridge in the cross-shore pressure gradient northwest of Icy Cape near ~70.5°N, manifested in the velocity field as the region of negligible flow along ~70.5°N on 15 September (Figures 2.10b). Note that the width of the southwestward flow is ~90 km and less than the local barotropic radius of deformation (~130 km). The implication is that although the cross-shore sea level gradient sloped downward onshore, it was of insufficient magnitude to reverse the pressure gradient farther offshore or in Barrow Canyon. By 17 September (Figure 2.10c) the winds had veered more towards the southwest. In response, canyon waters offshore of Point Franklin began veering northward, while the area of southwestward flow between Icy Cape and Point Lay expanded offshore. The winds continued to veer toward the southwest and intensified such that by 19 September the reversal regime was fully established, with the swiftest flows in the canyon and along the coast (Figure 2.10d). The divergent mode, although generally short-lived, thus has

the potential to disperse materials advected from the central shelf along the coast of western Alaska and into Barrow Canyon.

We expect that the SOM-derived surface circulation patterns occur throughout the year and that the divergent mode should occur more frequently through late fall and winter when transitions between downcanyon and upcanyon flow events are more common (Weingartner et al. 2017b). However, threshold wind speeds that catalyze the changes amongst the various modes may differ given that the surface stress will be modulated by sea ice.

2.6 Summary

We used SOM and EOFs in an examination of HFR-derived surface current patterns in the northeastern Chukchi Sea during the open-water seasons (nominally August–October) from 2010–2014. We identified major surface current circulation patterns and their dynamics in conjunction with regional winds and showed how this portion of the shelf surface circulation responds to the wind field and a background poleward pressure gradient.

We found that surface currents south of ~71.5°N and in Barrow Canyon flow northeastward except when northeasterly winds exceed ~6 m s^{-1}. The northeastward flow is primarily a manifestation of the large-scale pressure gradient between the Pacific and Arctic Oceans. When northeasterly wind speeds are >6 m s^{-1}, the coastal sea level setdown is large enough to cause southwestward surface flow inshore and westward flow over the central shelf. Less frequently southward surface currents occur over portions of the domain in response to northwesterly or westerly winds exceeding ~6 m s^{-1}.

We also detected the divergent mode, a transitional circulation feature of 1 to 5 days duration, which develops as the flow field adjusts from northeastward to southwestward in response to intensifying northeasterly winds. The divergent mode is characterized by eastward (onshore) flow across the central shelf, which diverges upon approaching the coast. A portion of this onshore flow continues into the head of Barrow Canyon while the remainder turns southwestward inshore of the 40 m isobath; however, sampling constraints prevented us from a precise determination of the nature of the divergence between these two regions. The divergent

mode is a consequence of interaction amongst the poleward pressure gradient, increasing northeasterly winds ($>\sim$6 m s^{-1}), local bathymetry, and the regional hydrographic structure.

Along ~71.5°N there is an extensive zonally-oriented front. North of this front, surface pressure gradients are weak, and the surface currents are Ekman-like. The strong Ekman response occurs because the water column is strongly stratified; fresh, cool meltwaters occupy the upper 15 m, and cold, salty winter waters occupy the bottom layer. South of the front the manifestation of the poleward pressure gradient is stronger, and the water column is less stratified, with the surface layer containing moderately salty and warmer Bering Sea summer waters.

2.7 Acknowledgments

Figure 2.1. (a) Map of the Chukchi Sea with place names. Blue dots indicate 2012 HFR network grid points with more than 60% temporal coverage. Red squares show locations of HFR field sites. The red outlined area represents the NARR wind domain used in the SOM and EOF analyses, with the red triangle the location representative of the shelf wind time series. Legs 1 and 2 are hydrographic transects conducted in September 2013. Black dot north of Wainwright denotes the BC2 mooring. Gray arrows show schematic pathways of Pacific waters. Bathymetric contours are drawn from 10–100 m at 10-m intervals. Place names include HV = Hope Valley, HC = Herald Canyon, HeS = Herald Shoal, CC = Central Channel, and HaS = Hanna Shoal. (b) Grid points within the red rectangle are used to determine upcanyon and downcanyon flow conditions.
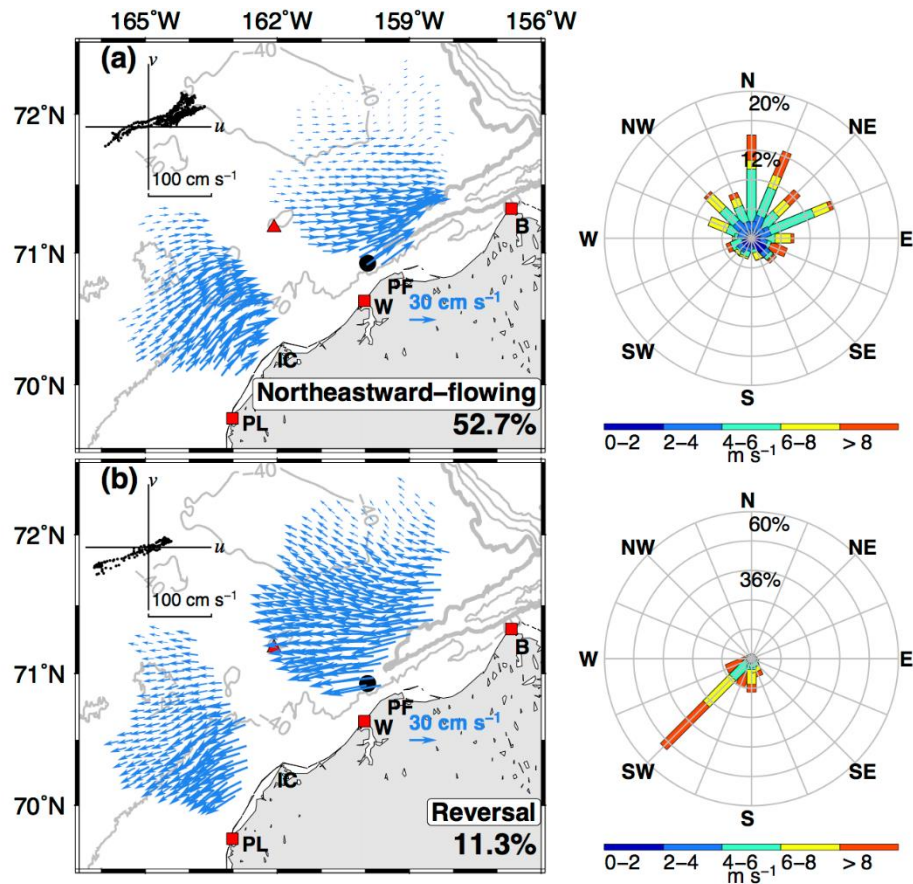
Figure 2.2. Representative circulation regimes categorized from twelve SOM-derived patterns of surface currents (blue vectors) for 2012: (a) northeastward-flowing regime and (b) reversal regime. The frequency of regime occurrence is included in each panel, and the 80 m isobath is thicker to define Barrow Canyon. The inserted scatter plot denotes vertically-averaged velocities from mooring BC2 (black dot) when the flow regime occurred. Polar histograms on the right denote wind velocities associated with the flow regime (red triangle). The direction follows oceanographic convention and speed is shaded. The percentage indicates frequencies of winds blowing toward that direction. Note that (c) and (d) are in the follow page.

Figure 2.2 cont. (c) northwesterly wind regime and (d) divergent mode. Note that the scales of current vectors in (c) and (d) are different than those in (a) and (b).
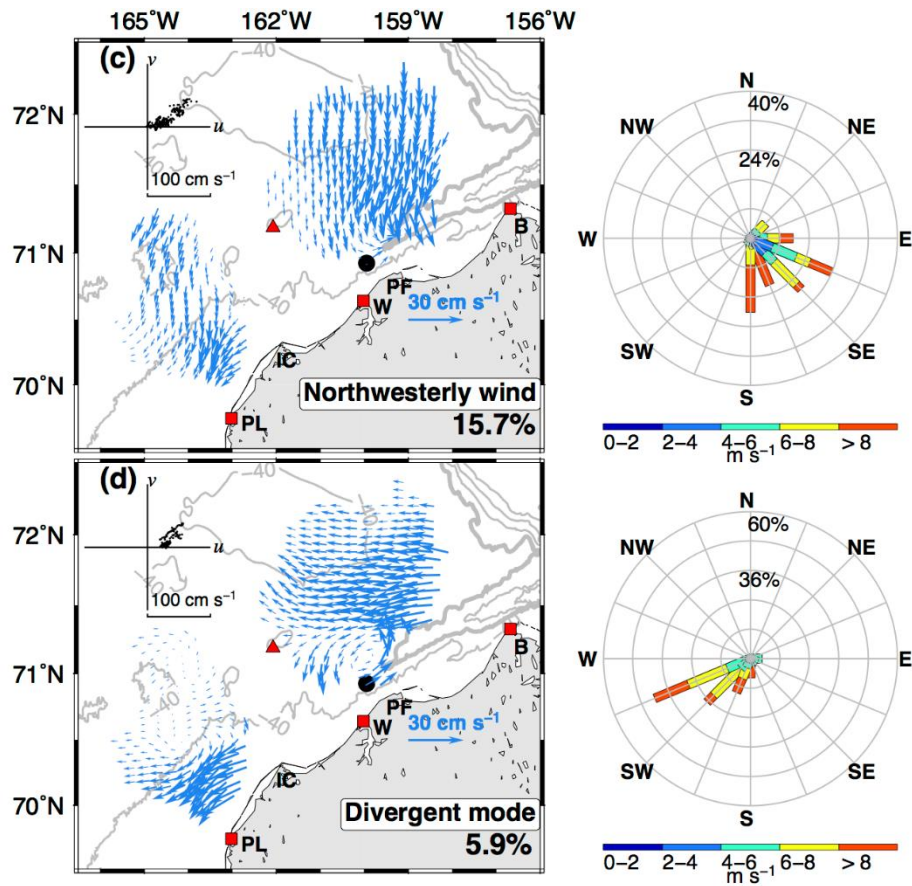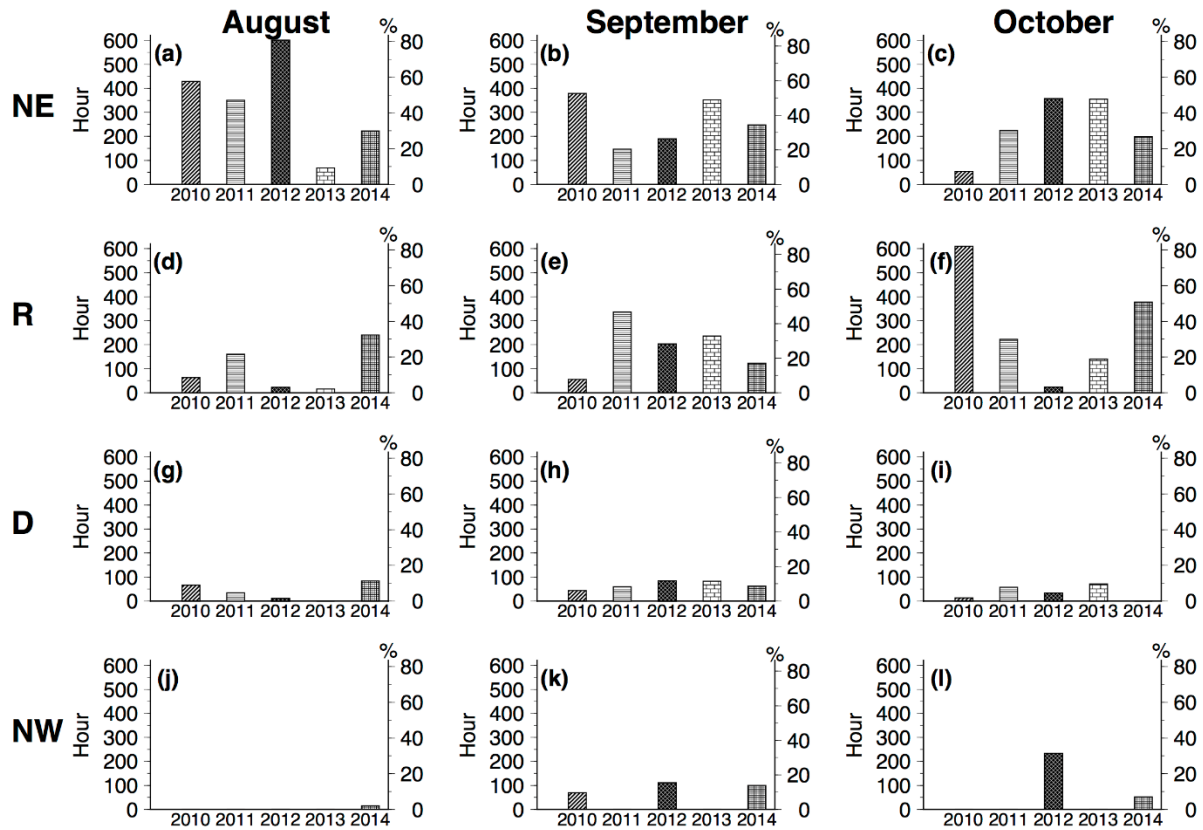
Figure 2.3. Monthly occurrences of SOM-derived circulation regimes for 2010-2014 with different hatching denoting different years. (a)-(c) Northeastward-flowing regime (NE). (d)-(f) Reversal regime (R). (g)-(i) Divergent mode (D). (j)-(l) Northwesterly wind regime (NW). A 15-day data gap in August 2013 is the reason for few regime estimates in that month.
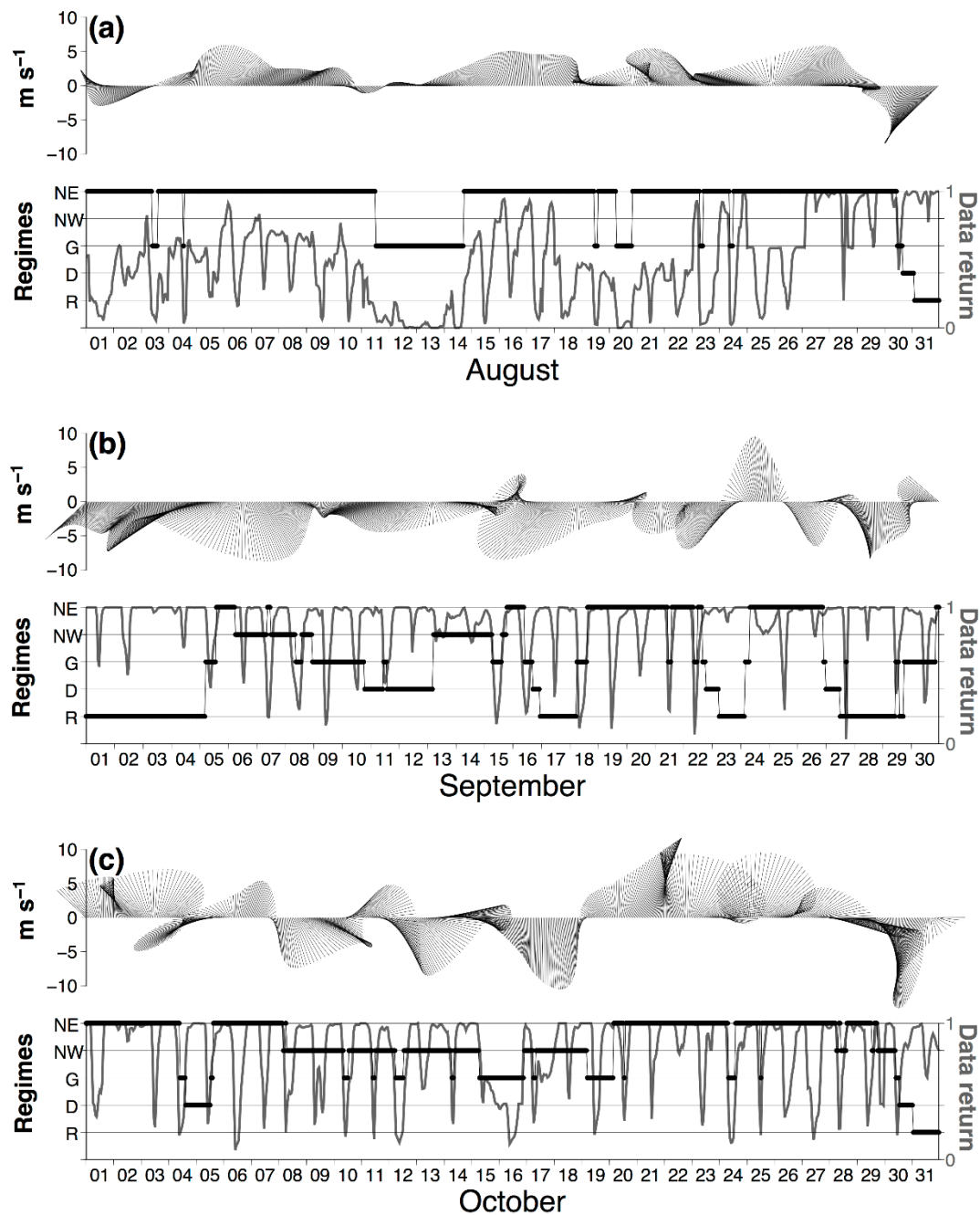
Figure 2.4. (a) Upper panel: time series of wind vectors in August 2012. The vector direction follows oceanographic convention. Lower panel: SOM-derived circulation regimes (black dots) in August 2012 and normalized data returns (gray line). The abbreviations are: R, reversal regime; D, divergent mode; G, pattern G; NW, northwesterly wind regime; NE, northeastward-flowing regime. (b) As in (a), but for September 2012. (c) As in (a), but for October 2012.

73
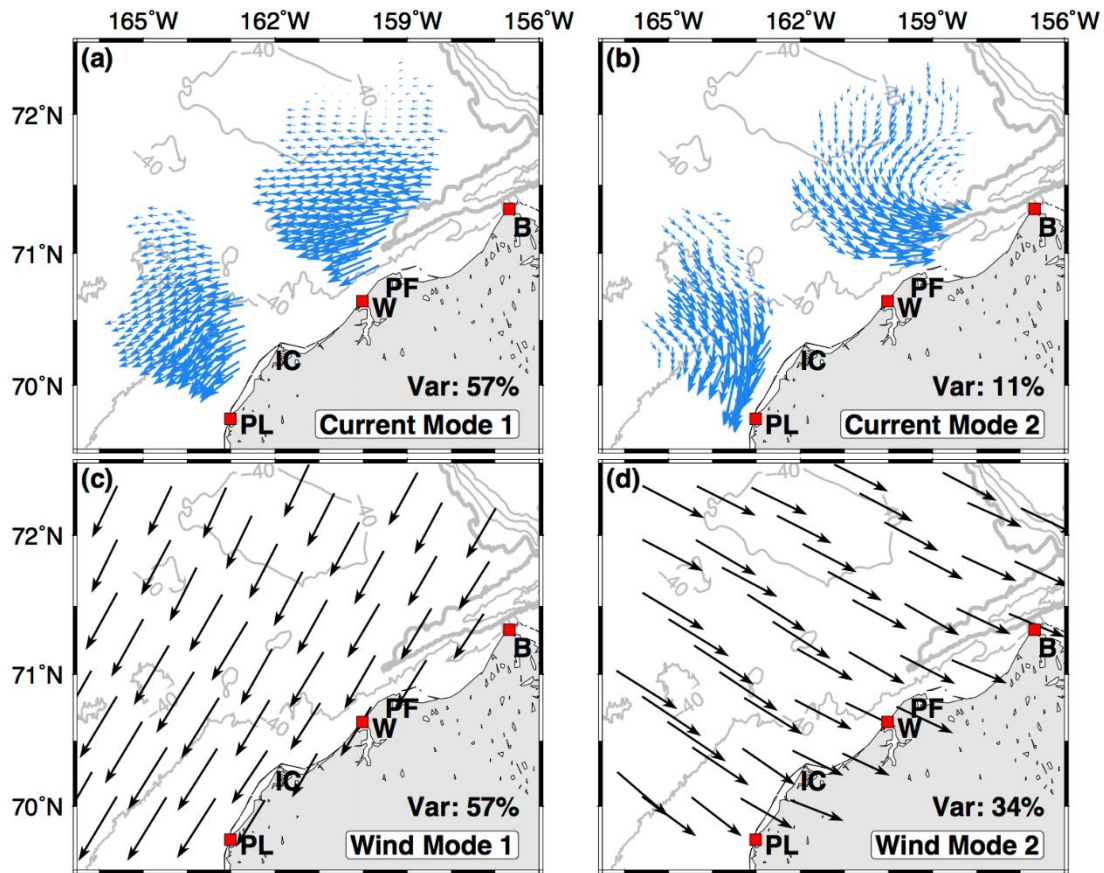
Figure 2.5. (a) EOF Mode 1 of 2012 reconstructed HFR data (blue vectors) and its explained variance. For clarity, only subsampled vectors are shown. (b) As in (a), but for Mode 2. (c) EOF Mode 1 of 2012 NARR winds (black vectors), also subsampled. (d) As in (c), but for Mode 2.
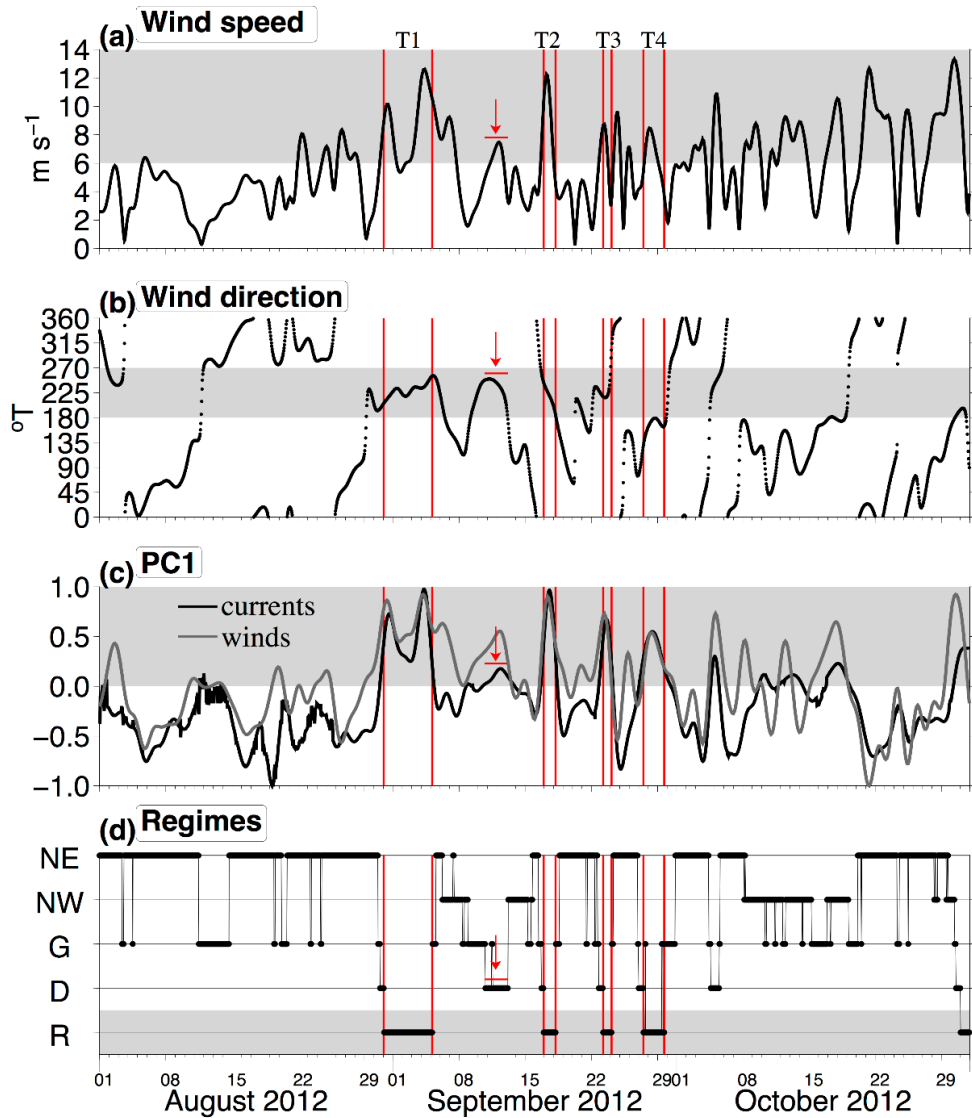
Figure 2.6. (a) Time series of wind speed with wind speeds ≥ 6 m s^{-1} highlighted in gray. (b) Time series of wind direction with gray shading corresponding to winds blowing from the northeast quadrant. (c) Time series of PC1 of surface currents (black) and PC1 of winds (gray) with gray shaded areas highlighting positive PC1 values. PC1 values approaching one indicate currents or winds approximating the Mode 1 structure. (d) Time series of representative circulation regimes derived from SOM (black dots): R, reversal (highlighted in gray); D, divergent mode; G, pattern G; NW, northwesterly wind; NE, northeastward-flowing. The gray shaded area highlights the reversal regime. Vertical red lines in each panel denote periods of selected reversal regimes (T1, T2, T3, and T4). Red arrow and bar denote a northeasterly wind event described in the text.
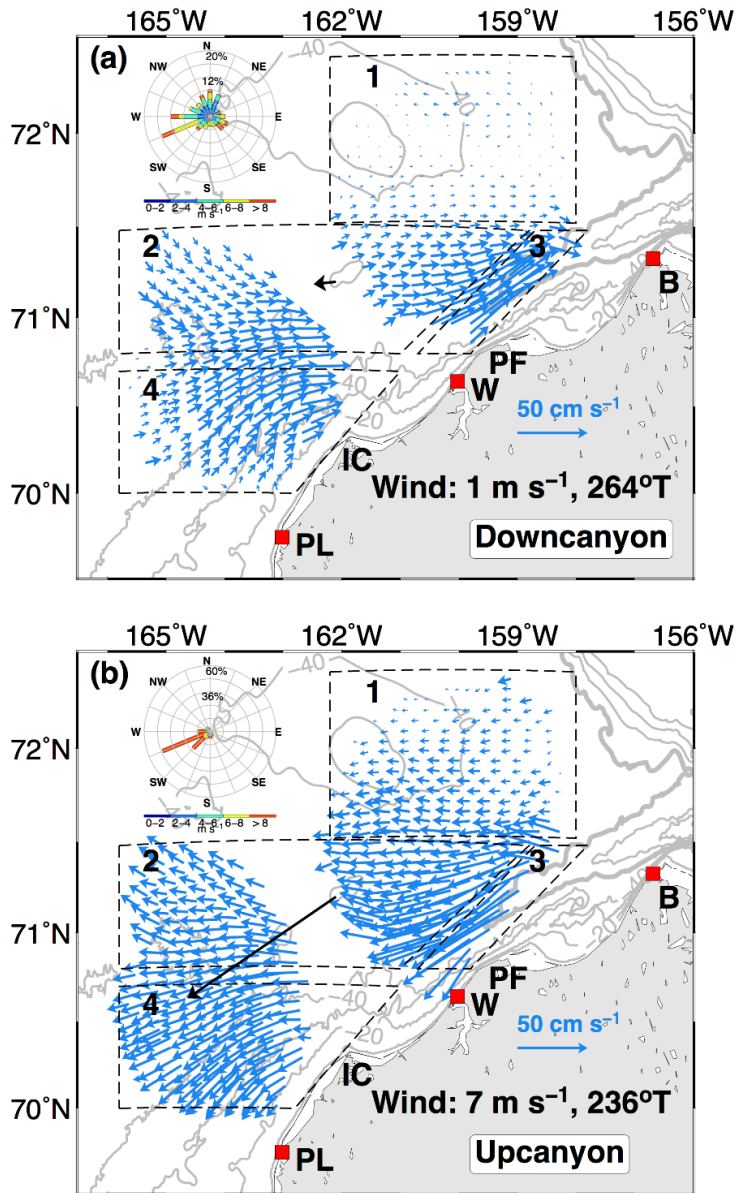
Figure 2.7. Mean (a) downcanyon and (b) upcanyon surface currents (blue vectors) for 2010–2014. Bathymetric contours (gray lines) are drawn within 200 m at 40-m intervals, with depths less than 40 m drawn at 10-m intervals. The black vector denotes the mean winds, and the polar histogram along 72°N denotes wind velocities. Areas circumscribed by dashed lines denote regions (labeled 1–4) of distinct flow behaviors (see text). For clarity, the vectors were subsampled.
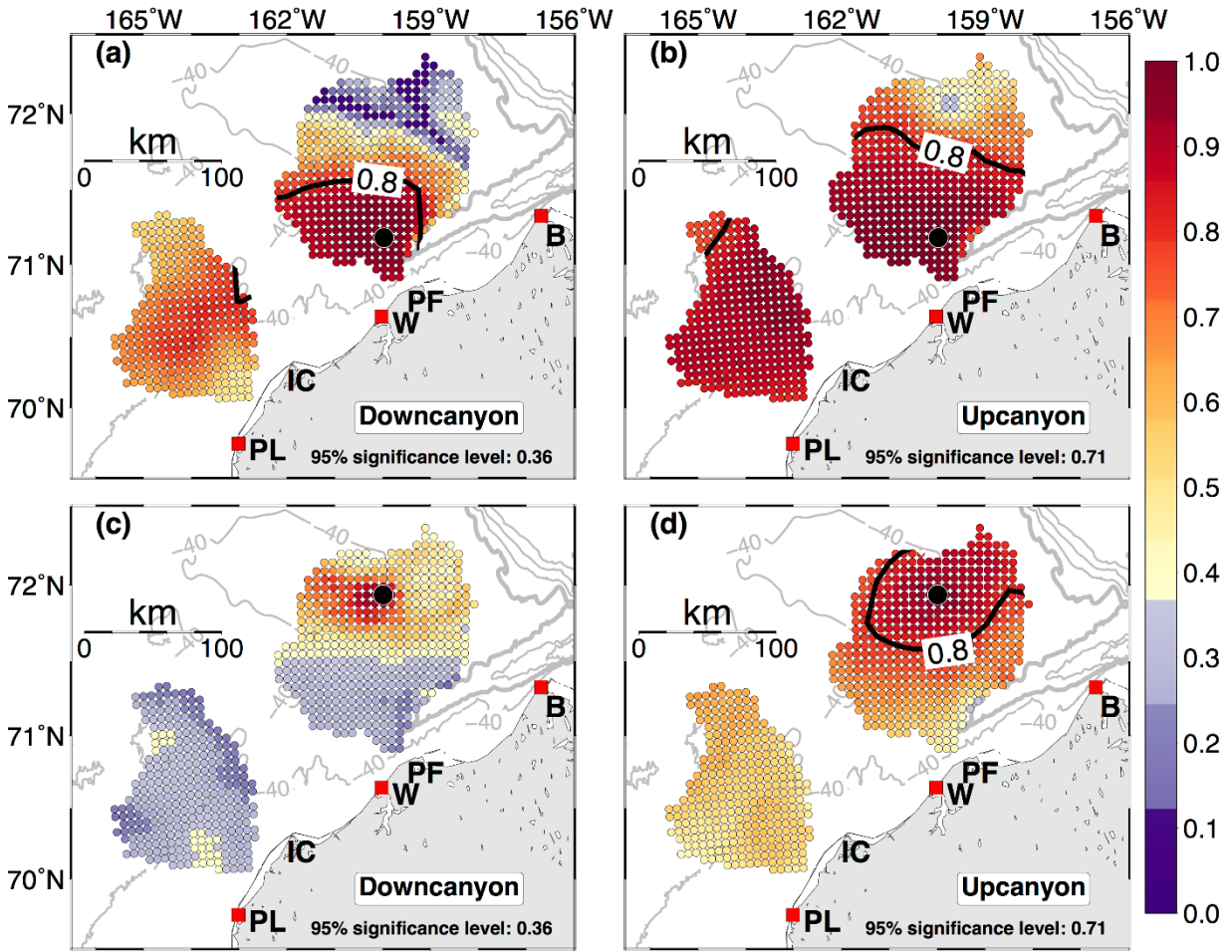
Figure 2.8. Spatial distribution of complex correlations of surface currents with respect to a reference grid point (large black dot) for (a, c) downcanyon and (b, d) upcanyon flow. Black contour denotes the 0.8 correlation level. Correlation below the *e*-folding scale is shaded in cool colors. The 95% significance level is estimated from the effective number of degrees of freedom using the integral time scale.
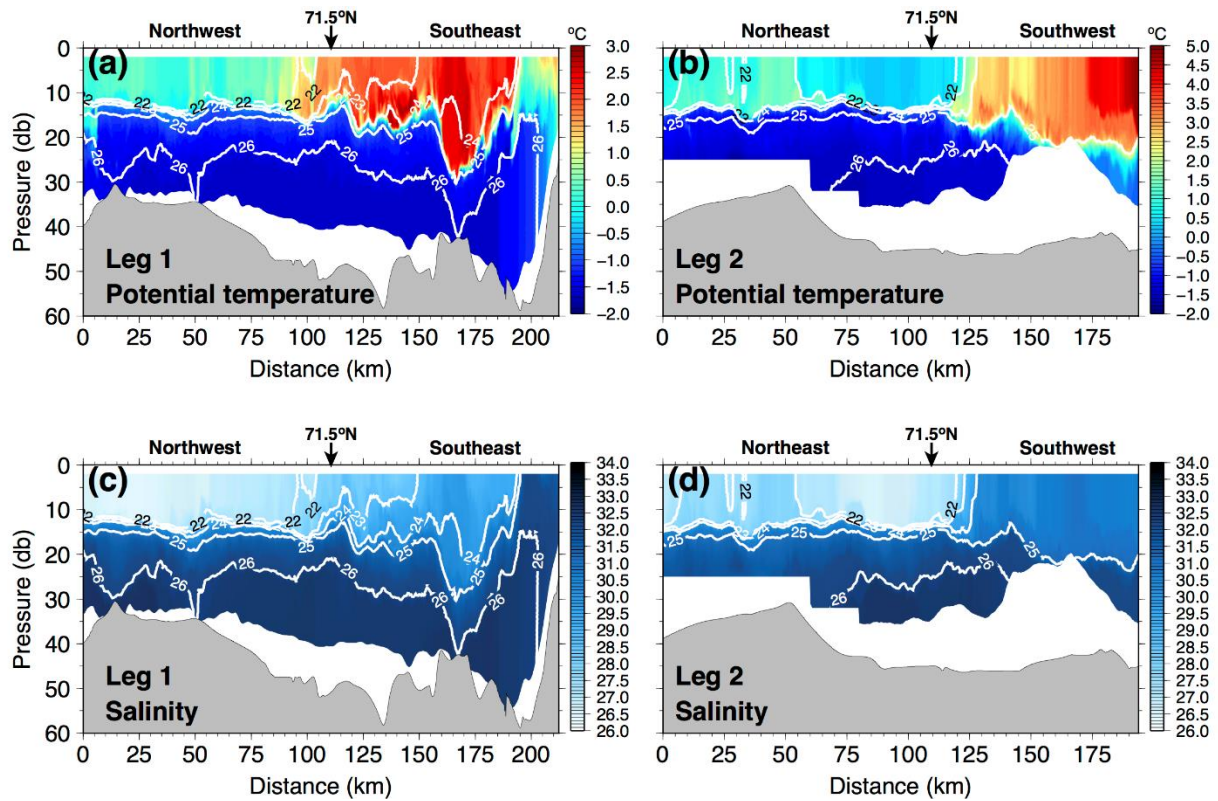
Figure 2.9. Vertical sections from September 2013 of potential temperature and salinity overlain with isopycnals (white contours) for (a, c) Leg 1 and (b, d) Leg 2. Black arrow denotes the location of 71.5°N. Note that the shading scales in (a) and (b) and the horizontal scales for Legs 1 and 2 are different.
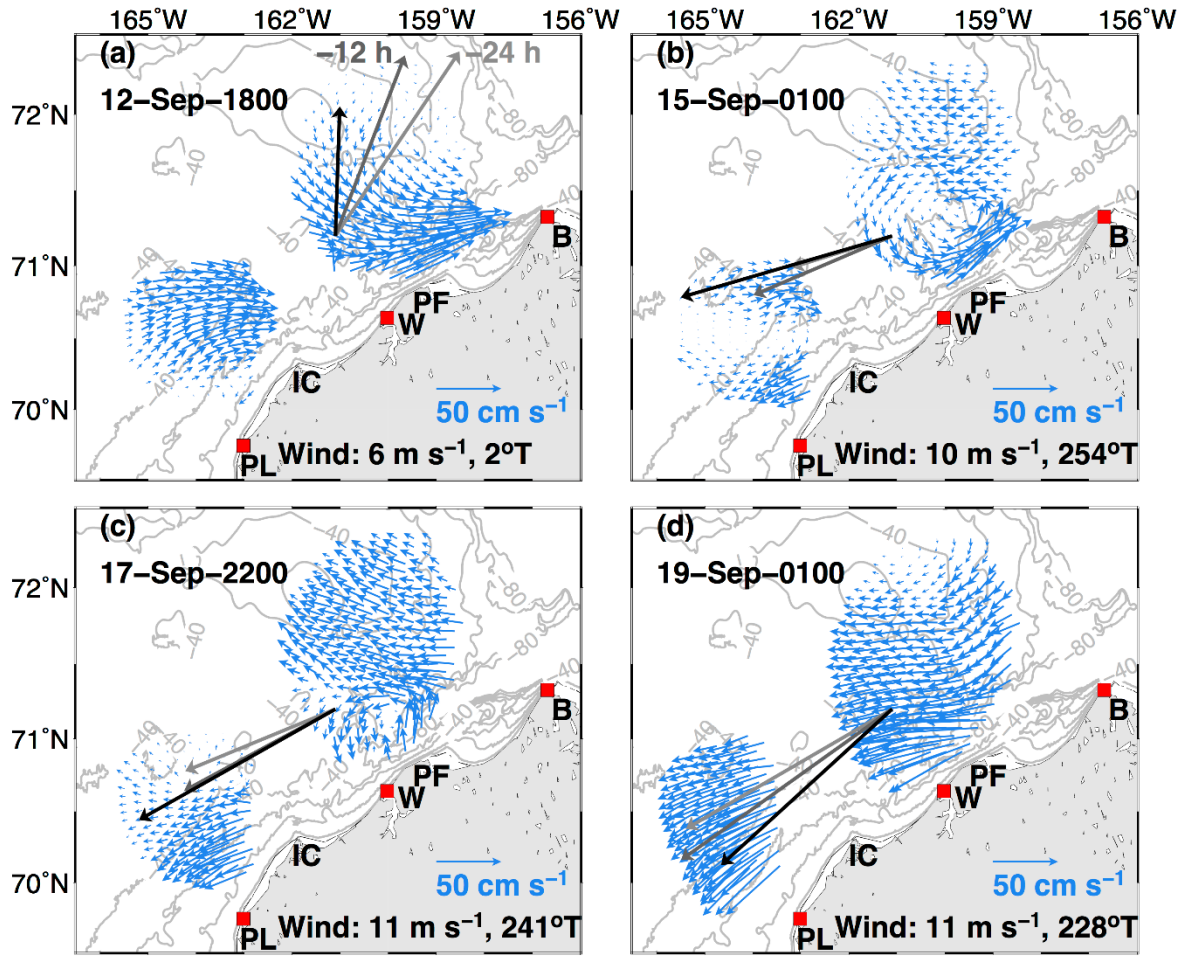
Figure 2.10. (a)-(d) HFR observations (blue vectors) during 12–19 September 2011 at indicated UTC time. The black vector denotes the wind at the cardinal hour of the snapshot, with the magnitude and direction shown in the legend, and the gray shaded vectors are winds for the preceding 12 and 24 hours. Bathymetric contours (gray lines) are drawn within 80 m at 10-m intervals. For clarity, the current vectors were subsampled.

Table 2.1. Summary of the EOF correlation analysis from the reconstructed fields. The correlations are all significant at the 95% significance level using the effective number of degrees of freedom derived from the integral time scale.

Year	Months	Correlation coefficient between PC1 of currents and winds	# of significant eigenmodes (currents)	% variance explained by Mode 1 (currents, winds)	% variance explained by Mode 2 (currents, winds)
2010	9 – 10	0.36[a]	2	50, 63	17, 30
2011	8 – 10	0.56	1	65, 65	9, 27
2012	8 – 10	0.74	2	57, 57	11, 34
2013	9 – 10	0.75	3	66, 60	15, 29
2014	8 – 10	0.83	3	64, 75	14, 19

[a]Low correlation coefficient is because wind Mode 1 in 2010 aligns nearly east-west, but Mode 1 of the currents is in the northeast-southwest direction.

2.8 References

Aagaard, K., and A. T. Roach, 1990: Arctic ocean-shelf exchange: Measurements in Barrow Canyon. *J. Geophys. Res. Ocean.*, **95**, 18163–18175, doi:10.1029/JC095iC10p18163. http://dx.doi.org/10.1029/JC095iC10p18163.

Aagaard, K., T. J. Weingartner, S. L. Danielson, R. A. Woodgate, G. C. Johnson, and T. E. Whitledge, 2006: Some controls on flow and salinity in Bering Strait. *Geophys. Res. Lett.*, **33**, doi:10.1029/2006GL026612. http://dx.doi.org/10.1029/2006GL026612.

Allen, J. S., 1973: Upwelling and Coastal Jets in a Continuously Stratified Ocean. *J. Phys. Oceanogr.*, **3**, 245–257, doi:10.1175/1520-0485(1973)003<0245:UACJIA>2.0.CO;2. http://dx.doi.org/10.1175/1520-0485(1973)003%3C0245:UACJIA%3E2.0.CO.

Barrick, D. E., 1978: HF radio oceanography — A review. *Boundary-Layer Meteorol.*, **13**, 23–43, doi:10.1007/BF00913860. http://dx.doi.org/10.1007/BF00913860.

Beckers, J. M., and M. Rixen, 2003: EOF Calculations and Data Filling from Incomplete Oceanographic Datasets. *J. Atmos. Ocean. Technol.*, **20**, 1839–1856, doi:10.1175/1520-0426(2003)020<1839:ECADFF>2.0.CO;2. http://journals.ametsoc.org/doi/abs/10.1175/1520-0426(2003)020%3C1839:ECADFF%3E2.0.CO;2.

Brink, K. H., 1998: Wind-driven currents over the continental shelf. *The Sea*, **10**, 3–20.

Chavanne, C., I. Janeković, P. Flament, P.-M. Poulain, M. Kuzmić, and K.-W. Gurgel, 2007: Tidal currents in the northwestern Adriatic: High-frequency radio observations and numerical model predictions. *J. Geophys. Res. Ocean.*, **112**, doi:10.1029/2006JC003523. http://dx.doi.org/10.1029/2006JC003523.

Danielson, S. L., T. J. Weingartner, K. S. Hedstrom, K. Aagaard, R. Woodgate, E. Curchitser, and P. J. Stabeno, 2014: Coupled wind-forced controls of the Bering–Chukchi shelf circulation and the Bering Strait throughflow: Ekman transport, continental shelf waves, and variations of the Pacific–Arctic sea surface height gradient. *Prog. Oceanogr.*, **125**, 40–61, doi:http://dx.doi.org/10.1016/j.pocean.2014.04.006. http://www.sciencedirect.com/science/article/pii/S0079661114000548.

Dzwonkowski, B., K. Park, and L. Jiang, 2011: Subtidal across-shelf velocity structure and surface transport effectiveness on the Alabama shelf of the northeastern Gulf of Mexico. *J. Geophys. Res. Ocean.*, **116**, doi:10.1029/2011JC007188. http://dx.doi.org/10.1029/2011JC007188.

Fang, Y.-C., T. J. Weingartner, R. A. Potter, P. R. Winsor, and H. Statscewich, 2015: Quality Assessment of HF Radar-Derived Surface Currents Using Optimal Interpolation. *J. Atmos. Ocean. Technol.*, **32**, 282–296. 10.1175/JTECH-D-14-00109.1.

Fredj, E., H. Roarty, J. Kohut, M. Smith, and S. Glenn, 2016: Gap Filling of the Coastal Ocean Surface Currents from HFR Data: Application to the Mid-Atlantic Bight HFR Network. *J. Atmos. Ocean. Technol.*, **33**, 1097–1111, doi:10.1175/JTECH-D-15-0056.1. http://dx.doi.org/10.1175/JTECH-D-15-0056.1.

Geoffroy, M., A. Majewski, M. LeBlanc, S. Gauthier, W. Walkusz, J. D. Reist, and L. Fortier, 2016: Vertical segregation of age-0 and age-1+ polar cod (Boreogadus saida) over the annual cycle in the Canadian Beaufort Sea. *Polar Biol.*, **39**, 1023–1037, doi:10.1007/s00300-015-1811-z. http://dx.doi.org/10.1007/s00300-015-1811-z.

Gong, D., and R. S. Pickart, 2015: Summertime circulation in the eastern Chukchi Sea. *Deep Sea Res. Part II Top. Stud. Oceanogr.*, **118**, 18–31, doi:10.1016/j.dsr2.2015.02.006. http://linkinghub.elsevier.com/retrieve/pii/S096706451500034X.

Hirano, D., Y. Fukamachi, E. Watanabe, K. I. Ohshima, K. Iwamoto, A. R. Mahoney, H. Eichen, D. Simizu, and T. Tamura, 2016: A wind-driven, hybrid latent and sensible heat coastal polynya off Barrow, Alaska. *J. Geophys. Res. Ocean.*, **121**, 980–997, doi:10.1002/2015JC011318. http://dx.doi.org/10.1002/2015JC011318.

Itoh, M., S. Nishino, Y. Kawaguchi, and T. Kikuchi, 2013: Barrow Canyon volume, heat, and freshwater fluxes revealed by long-term mooring observations between 2000 and 2008. *J. Geophys. Res. Ocean.*, **118**, 4363–4379, doi:10.1002/jgrc.20290. http://dx.doi.org/10.1002/jgrc.20290.

Johnson, W. R., 1989: Current response to wind in the Chukchi Sea: A regional coastal upwelling event. *J. Geophys. Res. Ocean.*, **94**, 2057–2064, doi:10.1029/JC094iC02p02057. http://dx.doi.org/10.1029/JC094iC02p02057.

Kaihatu, J. M., R. A. Handler, G. O. Marmorino, and L. K. Shay, 1998: Empirical Orthogonal Function Analysis of Ocean Surface Currents Using Complex and Real-Vector Methods. *J. Atmos. Ocean. Technol.*, **15**, 927–941.

Kaplan, D. M., and F. Lekien, 2007: Spatial interpolation and filtering of surface current data based on open-boundary modal analysis. *J. Geophys. Res. Ocean.*, **112**, C12007, doi:10.1029/2006JC003984. http://doi.wiley.com/10.1029/2006JC003984 (Accessed September 12, 2013).

Kim, S. Y., E. Terrill, and B. Cornuelle, 2007: Objectively mapping HF radar-derived surface current data using measured and idealized data covariance matrices. *J. Geophys. Res. Ocean.*, **112**, C06021, doi:10.1029/2006JC003756. http://doi.wiley.com/10.1029/2006JC003756 (Accessed September 12, 2013).

——, E. J. Terrill, and B. D. Cornuelle, 2008: Mapping surface currents from HF radar radial velocity measurements using optimal interpolation. *J. Geophys. Res. Ocean.*, **113**, C10023, doi:10.1029/2007JC004244. http://doi.wiley.com/10.1029/2007JC004244 (Accessed September 12, 2013).

Kohonen, T., 2001: Self-Organizing Maps. *Springer Ser. Inf. Sci., 3rd ed., Springer, New York*, **30**, 501 pp.

Kundu, P. K., and J. S. Allen, 1976: Some Three-Dimensional Characteristics of Low-Frequency Current Fluctuations near the Oregon Coast. *J. Phys. Oceanogr.*, **6**, 181–199, doi:10.1175/1520-0485(1976)006<0181:STDCOL>2.0.CO;2. http://dx.doi.org/10.1175/1520-0485(1976)006%3C0181:STDCOL%3E2.0.CO.

Liu, Y., and R. H. Weisberg, 2005: Patterns of ocean current variability on the West Florida Shelf using the self-organizing map. *J. Geophys. Res. Ocean.*, **110**, doi:10.1029/2004JC002786. http://dx.doi.org/10.1029/2004JC002786.

——, R. H. Weisberg, and C. N. K. Mooers, 2006: Performance evaluation of the self-organizing map for feature extraction. *J. Geophys. Res. Ocean.*, **111**, doi:10.1029/2005JC003117. http://doi.wiley.com/10.1029/2005JC003117 (Accessed October 25, 2013).

——, ——, and L. K. Shay, 2007: Current Patterns on the West Florida Shelf from Joint Self-Organizing Map Analyses of HF Radar and ADCP Data. *J. Atmos. Ocean. Technol.*, **24**, 702–712, doi:10.1175/JTECH1999.1. http://journals.ametsoc.org/doi/abs/10.1175/JTECH1999.1 (Accessed September 12, 2013).

Lu, K., T. Weingartner, S. Danielson, P. Winsor, E. Dobbins, K. Martini, and H. Statscewich, 2015: Lateral mixing across ice meltwater fronts of the Chukchi Sea shelf. *Geophys. Res. Lett.*, doi:10.1002/2015GL064967. http://dx.doi.org/10.1002/2015GL064967.

Martini, K. I., P. J. Stabeno, C. Ladd, P. Winsor, T. J. Weingartner, C. W. Mordy, and L. B. Eisner, 2016: Dependence of subsurface chlorophyll on seasonal water masses in the Chukchi Sea. *J. Geophys. Res. Ocean.*, **121**, 1755–1770, doi:10.1002/2015JC011359. http://dx.doi.org/10.1002/2015JC011359.

Mau, J.-C., D.-P. Wang, D. S. Ullman, and D. L. Codiga, 2007: Characterizing Long Island Sound outflows from HF radar using self-organizing maps. *Estuar. Coast. Shelf Sci.*, **74**, 155–165, doi:10.1016/j.ecss.2007.04.007. http://linkinghub.elsevier.com/retrieve/pii/S0272771407001072.

Mesinger, F., G. DiMego, E. Kalnay, K. Mitchell, P. C. Shafran, W. Ebisuzaki, D. Jović, J. Woollen, E. Rogers, E. H. Berbery, M. B. Ek, Y. Fan, R. Grumbine, W. Higgins, H. Li, Y. Lin, G. Manikin, D. Parrish, and W. Shi, 2006: North American Regional Reanalysis. *Bull. Am. Meteorol. Soc.*, **87**, 343–360, doi:10.1175/BAMS-87-3-343. http://dx.doi.org/10.1175/BAMS-87-3-343.

Mihanović, H., S. Cosoli, I. Vilibić, D. Ivanković, V. Dadić, and M. Gačić, 2011: Surface current patterns in the northern Adriatic extracted from high-frequency radar data using self-organizing map analysis. *J. Geophys. Res. Ocean.*, **116**, doi:10.1029/2011JC007104. http://dx.doi.org/10.1029/2011JC007104.

Mountain, D. G., L. K. Coachman, and K. Aagaard, 1976: On the Flow Through Barrow Canyon. *J. Phys. Oceanogr.*, **6**, 461–470, doi:10.1175/1520-0485(1976)006<0461:OTFTBC>2.0.CO;2. http://dx.doi.org/10.1175/1520-0485(1976)006%3C0461:OTFTBC%3E2.0.CO.

North, G. R., T. L. Bell, R. F. Cahalan, and F. J. Moeng, 1982: Sampling Errors in the Estimation of Empirical Orthogonal Functions. *Mon. Weather Rev.*, **110**, 699–706, doi:10.1175/1520-0493(1982)110<0699:SEITEO>2.0.CO;2. http://dx.doi.org/10.1175/1520-0493(1982)110%3C0699:SEITEO%3E2.0.CO.

Okkonen, S. R., C. J. Ashjian, R. G. Campbell, W. Maslowski, J. L. Clement-Kinney, and R. Potter, 2009: Intrusion of warm Bering/Chukchi waters onto the shelf in the western Beaufort Sea. *J. Geophys. Res. Ocean.*, **114**, doi:10.1029/2008JC004870. http://dx.doi.org/10.1029/2008JC004870.

Paduan, J. D., and L. Washburn, 2013: High-frequency radar observations of ocean surface currents. *Ann. Rev. Mar. Sci.*, **5**, 115–136, doi:10.1146/annurev-marine-121211-172315. http://www.ncbi.nlm.nih.gov/pubmed/22809196 (Accessed August 30, 2013).

Paquette, R. G., and R. H. Bourke, 1974: Observations on the coastal current of arctic Alaska. *J. Mar. Res.*, **32**, 195–207.

Paquette, R. G., and R. H. Bourke, 1981: Ocean circulation and fronts as related to ice melt-back in the Chukchi Sea. *J. Geophys. Res. Ocean.*, **86**, 4215–4230, doi:10.1029/JC086iC05p04215. http://dx.doi.org/10.1029/JC086iC05p04215.

Pickart, R. S., L. J. Pratt, D. J. Torres, T. E. Whitledge, A. Y. Proshutinsky, K. Aagaard, T. A. Agnew, G.W.K Moore, and H. J. Dail, 2010: Evolution and dynamics of the flow through Herald Canyon in the western Chukchi Sea. *Deep Sea Res. Part II Top. Stud. Oceanogr.*, **57**, 5–26, doi:10.1016/j.dsr2.2009.08.002. http://linkinghub.elsevier.com/retrieve/pii/S0967064509002458 (Accessed September 12, 2013).

Pickart, R. S., G. W. K. Moore, C. Mao, F. Bahr, C. Nobre, and T. J. Weingartner, 2016: Circulation of winter water on the Chukchi shelf in early Summer. *Deep Sea Res. Part II Top. Stud. Oceanogr.*, **130**, 56–75, doi:http://dx.doi.org/10.1016/j.dsr2.2016.05.001. http://www.sciencedirect.com/science/article/pii/S0967064516301011.

Questel, J. M., C. Clarke, and R. R. Hopcroft, 2013: Seasonal and interannual variation in the planktonic communities of the northeastern Chukchi Sea during the summer and early fall. *Cont. Shelf Res.*, **67**, 23–41, doi:http://dx.doi.org/10.1016/j.csr.2012.11.003. http://www.sciencedirect.com/science/article/pii/S0278434312003044.

Richardson, A. J., C. Risien, and F. A. Shillington, 2003: Using self-organizing maps to identify patterns in satellite imagery. *Prog. Oceanogr.*, **59**, 223–239, doi:http://dx.doi.org/10.1016/j.pocean.2003.07.006. http://www.sciencedirect.com/science/article/pii/S007966110300171X.

Roach, A. T., K. Aagaard, C. H. Pease, S. A. Salo, T. Weingartner, V. Pavlov, and M. Kulakov, 1995: Direct measurements of transport and water properties through the Bering Strait. *J. Geophys. Res. Ocean.*, **100**, 18443–18457, doi:10.1029/95JC01673. http://dx.doi.org/10.1029/95JC01673.

Serreze, M. C., A. P. Barrett, A. G. Slatter, R. A. Woodgate, K. Aagaard, R. B. Lammers, M. Steele, R. Moritz, M. Meredith, and C. M. Lee, 2006: The large-scale freshwater cycle of the Arctic. *J. Geophys. Res. Ocean.*, **111**, doi:10.1029/2005JC003424. http://dx.doi.org/10.1029/2005JC003424.

Shimada, K., T. Kamoshida, M. Itoh, S. Nishino, E. Carmack, F. McLaughlin, S. Zimmermann, and A. Proshutinsky, 2006: Pacific Ocean inflow: Influence on catastrophic reduction of sea ice cover in the Arctic Ocean. *Geophys. Res. Lett.*, **33**, L08605, doi:10.1029/2005GL025624. http://doi.wiley.com/10.1029/2005GL025624 (Accessed October 21, 2014).

Spall, M. A., 2007: Circulation and water mass transformation in a model of the Chukchi Sea. *J. Geophys. Res.*, **112**, C05025, doi:10.1029/2005JC003364. http://doi.wiley.com/10.1029/2005JC003364 (Accessed September 12, 2013).

Steele, M., W. Ermold, and J. Zhang, 2008: Arctic Ocean surface warming trends over the past 100 years. *Geophys. Res. Lett.*, **35**, doi:10.1029/2007GL031651. http://dx.doi.org/10.1029/2007GL031651.

Stewart, R. H., and J. W. Joy, 1974: HF radio measurements of surface currents. *Deep Sea Research and Oceanographic Abstracts*, Vol. 21 of, Elsevier, 1039–1049.

Stigebrandt, A., 1984: The North Pacific: A Global-Scale Estuary. *J. Phys. Oceanogr.*, **14**, 464–470, doi:10.1175/1520-0485(1984)014<0464:TNPAGS>2.0.CO;2. http://dx.doi.org/10.1175/1520-0485(1984)014%3C0464:TNPAGS%3E2.0.CO.

Taylor, M. H., M. Losch, M. Wenzel, and J. Schröter, 2013: On the Sensitivity of Field Reconstruction and Prediction Using Empirical Orthogonal Functions Derived from Gappy Data. *J. Clim.*, **26**, 9194–9205, doi:10.1175/JCLI-D-13-00089.1. http://dx.doi.org/10.1175/JCLI-D-13-00089.1.

Teague, C., 2001: Ionospheric effects on coastal radar systems., *Radiowave Oceanography: The First International Workshop*, H. C. Graber and J. D. Paduan, Eds., University of Miami, 56–61.

Vilibić, I., H. Kalinić, H. Mihanović, S. Cosoli, M. Tudor, N. Žagar, and B. Jesenko, 2016: Sensitivity of HF radar-derived surface current self-organizing maps to various processing procedures and mesoscale wind forcing. *Comput. Geosci.*, **20**, 115–131, doi:10.1007/s10596-015-9550-3. http://dx.doi.org/10.1007/s10596-015-9550-3.

Weingartner, T. J., D. J. Cavalieri, K. Aagaard, and Y. Sasaki, 1998: Circulation, dense water formation, and outflow on the northeast Chukchi Shelf. *J. Geophys. Res. Ocean.*, **103**, 7647–7661, doi:10.1029/98JC00374. http://dx.doi.org/10.1029/98JC00374.

——, K. Aagaard, R. Woodgate, S. Danielson, Y. Sasaki, and D. Cavalieri, 2005: Circulation on the north central Chukchi Sea shelf. *Deep Sea Res. Part II Top. Stud. Oceanogr.*, **52**, 3150–3174, doi:10.1016/j.dsr2.2005.10.015. http://linkinghub.elsevier.com/retrieve/pii/S0967064505002158 (Accessed September 20, 2013).

——, E. Dobbins, S. Danielson, P. Winsor, R. Potter, and H. Statscewich, 2013a: Hydrographic variability over the northeastern Chukchi Sea shelf in summer-fall 2008–2010. *Cont. Shelf Res.*, **67**, 5–22, doi:http://dx.doi.org/10.1016/j.csr.2013.03.012. http://www.sciencedirect.com/science/article/pii/S0278434313000782.

——, P. Winsor, R. A. Potter, H. Statscewich, and E. L. Dobbins, 2013b: OCS Study BOEM 2012-079 Application of High Frequency Radar to Potential Hydrocarbon Development Areas in the Northeast Chukchi Sea. *Final Rep., U.S. Dept. Inter. Alaska Outer Cont. Shelf Reg. Contract M09AC15207, OCS Study BOEM 2012- 079, 162 pp. [Available online www.boem.gov/ESPIS/5/5266.pdf]*,.

——, Y.-C. Fang, P. Winsor, E. Dobbins, R. Potter, H. Statscewich, T. Mudge, B. Irving, L. Sousa, and K. Borg, 2017a: The summer hydrographic structure of the Hanna Shoal region on the northeastern Chukchi Sea shelf: 2011–2013. *Deep Sea Res. Part II Top. Stud. Oceanogr.*, **144**, 6–20, doi:https://doi.org/10.1016/j.dsr2.2017.08.006.

——, R. A. Potter, C. A. Stoudt, E. L. Dobbins, H. Statscewich, P. R. Winsor, T. D. Mudge, and K. Borg, 2017b: Transport and thermohaline variability in Barrow Canyon on the Northeastern Chukchi Sea Shelf. *J. Geophys. Res. Ocean.*, **122**, doi:10.1002/2016JC012636. http://dx.doi.org/10.1002/2016JC012636.

Winsor, P., and D. C. Chapman, 2004: Pathways of Pacific water across the Chukchi Sea: A numerical model study. *J. Geophys. Res. Ocean.*, **109**, C03002, doi:10.1029/2003JC001962. http://dx.doi.org/10.1029/2003JC001962.

Wood, K. R., N. A. Bond, S. L. Danielson, J. E. Overland, S. A. Salo, P. J. Stabeno, and J. Whitefield, 2015: A decade of environmental change in the Pacific Arctic region. *Prog. Oceanogr.*, **136**, 12–31, doi:http://dx.doi.org/10.1016/j.pocean.2015.05.005. http://www.sciencedirect.com/science/article/pii/S0079661115001020.

Woodgate, R. A., K. Aagaard, and T. J. Weingartner, 2005: A year in the physical oceanography of the Chukchi Sea: Moored measurements from autumn 1990–1991. *Deep Sea Res. Part II Top. Stud. Oceanogr.*, **52**, 3116–3149, doi:10.1016/j.dsr2.2005.10.016. http://linkinghub.elsevier.com/retrieve/pii/S0967064505002146 (Accessed September 17, 2013).

Woodgate, R. A., K. Aagaard, and T. J. Weingartner, 2006: Interannual changes in the Bering Strait fluxes of volume, heat and freshwater between 1991 and 2004. *Geophys. Res. Lett.*, **33**, doi:10.1029/2006GL026931. http://dx.doi.org/10.1029/2006GL026931.

——, T. J. Weingartner, and R. Lindsay, 2012: Observed increases in Bering Strait oceanic fluxes from the Pacific to the Arctic from 2001 to 2011 and their impacts on the Arctic Ocean water column. *Geophys. Res. Lett.*, **39**, doi:10.1029/2012GL054092. http://dx.doi.org/10.1029/2012GL054092.

Wyllie-Echeverria, T., W. E. Barber, and S. Wyllie-Echeverria, 1992: Water masses and transport of Age-0 Arctic Cod and age-0 Bering Flounder into the northeaster Chukchi Sea, edited by J. B. Reynolds, Fish Ecology in Arctic North America, American Fisheries Society Symposium 19, 345 pp, 60-68.

2.9 Appendices

Appendix 2.1. Twelve original SOM patterns for the 2012 data.

SOM derived surface current and wind patterns from 2012 were used to define circulation features in the northeastern Chukchi Sea. Generating 12 patterns allowed us to isolate data gaps and unique circulation features; however, it also derived many patterns that were similar to one another. To simplify presented results in the main manuscript, similar patterns were grouped together. We provide all 12 original patterns here for those interested in more detail. Figure A2.1 corresponds to the simplified Figures 2.2a-d, while Figure A2.2 corresponds to Figure 2.4.

Please note that the number of the pattern is not a ranking, but rather an arbitrarily assigned identification number. This should be evident from the percentage of occurrence recorded in each figure.

Figures A2.1a and A2.1b were grouped together as the reversal regime (Figure 2.2b) as these patterns both depict overall flow in the domain to the southwest/west under northeasterly winds. Figures A2.1c and A2.1f are classified as the northwesterly wind regime (Figure 2.2c). Figure A2.1d stands alone as the divergent mode (Figure 2.2d). Figure A2.1e represents Pattern G, indicative of times when data returns were sparse.

Figures A2.1g through A2.1l were grouped together as the northeastward-flowing regime (Figure 2.2a). All of these patterns contained predominantly northeastward-flowing currents along the coastline. The main differences result from winds and data gap distributions. Patterns 7 (Figure A2.1g) and 10 (Figure A2.1j) depict discontinuities between the northern and southern masks, with sparse, variable currents in the southern region near Point Lay and Icy Cape. A review of the data confirmed that the Point Lay HFR was experiencing maintenance issues in August 2012, when patterns 7 and 10 occurred most often. Given that the northern region of currents is derived from the Wainwright and Barrow HFR, which were operational, it follows that the currents in the northern region are accurate while the currents in the southern region are not. Therefore it is still appropriate to categorize patterns 7 and 10 as the northeastward-flowing

regime, although they depict currents when only the northern mask is operational. Finally, Table

A2.1 summarizes these patterns.
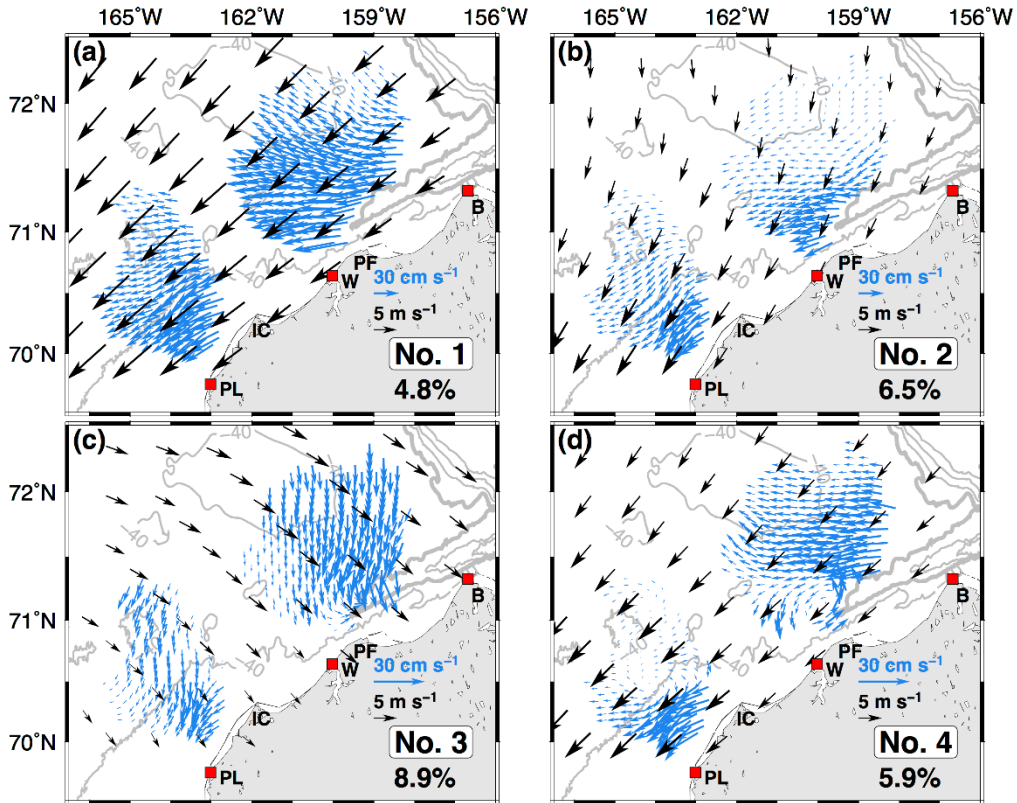
Figure A2.1. (a)-(d), SOM-derived patterns No. 1–4 of surface currents (blue vectors) and paired winds (black vectors) for 2012 data. Pattern number and its relative frequency of occurrence are shown in the lower right corner. The 80 m isobath is thicker to define Barrow Canyon. Note that the scales of current vectors in Patterns No. 3–8 are different.
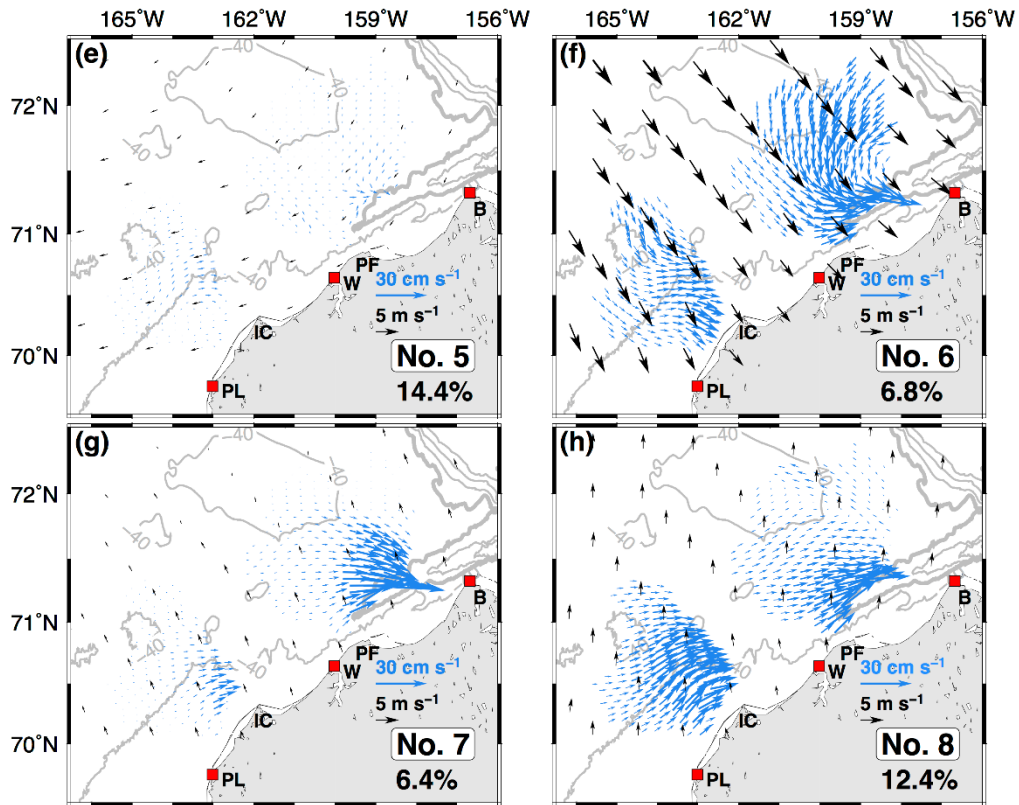
Figure A2.1 cont. (e)-(h), SOM-derived patterns No. 5–8 of surface currents (blue vectors) and paired winds (black vectors) for 2012 data.
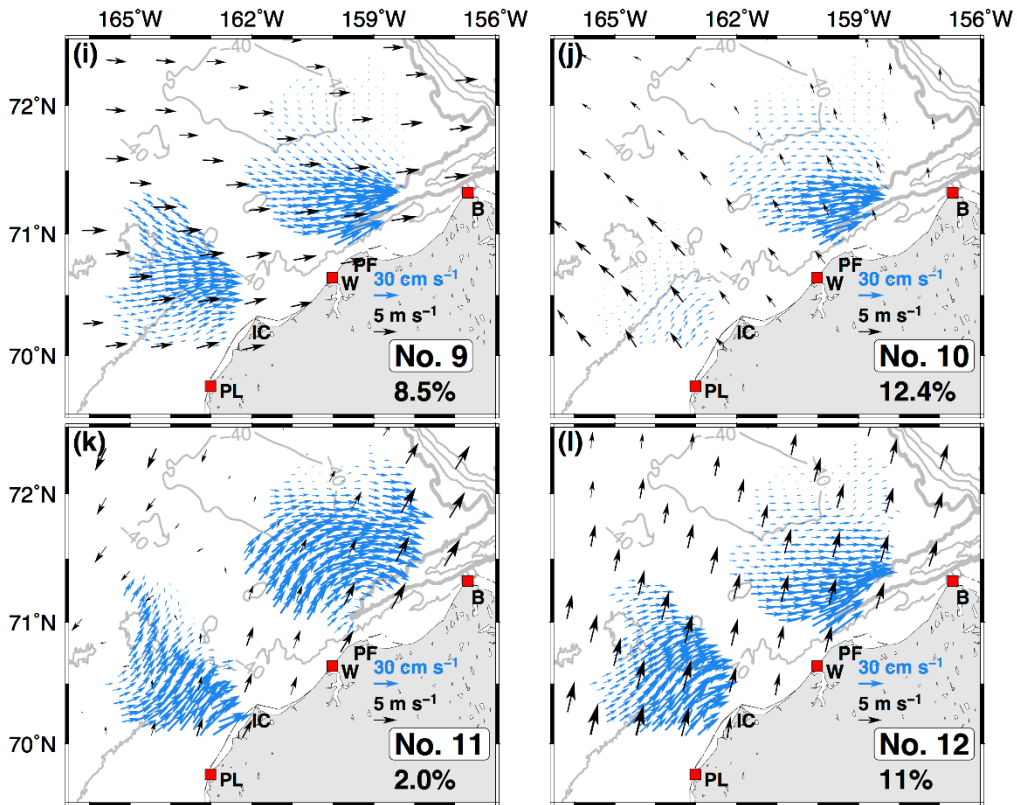
Figure A2.1 cont. (i)-(l), SOM-derived patterns No. 9–12 of surface currents (blue vectors) and paired winds (black vectors) for 2012 data.
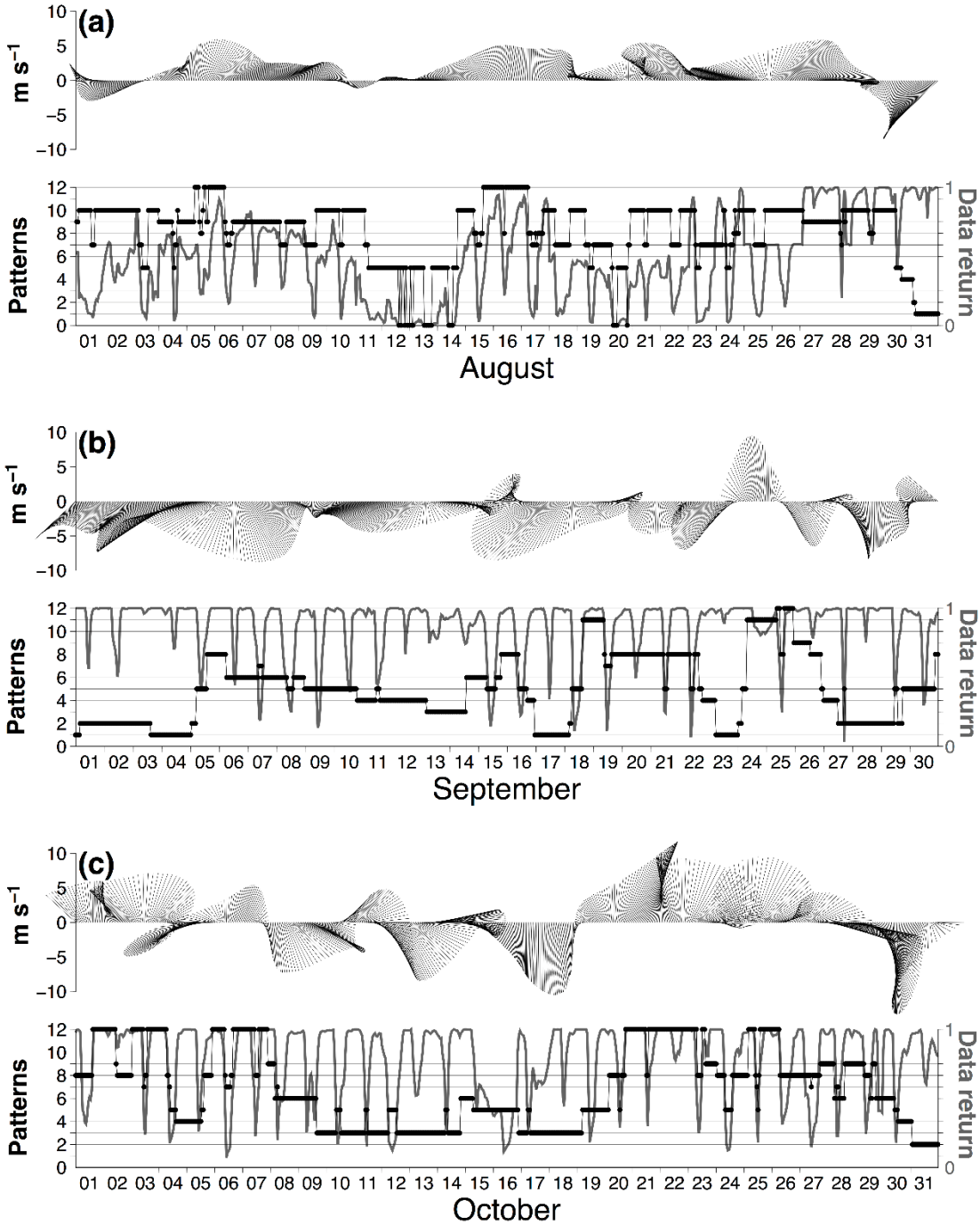
Figure A2.2. (a) Upper panel: time series of wind vectors in August 2012. The vector direction follows oceanographic convention. Lower panel: SOM-derived patterns (black dots) in August 2012 and normalized data returns (gray line). Pattern numbers correspond to Figure A2.1. Pattern 0 denotes times when data return is zero. (b) As in (a), but for September 2012. (c) As in (a), but for October 2012.

Table A2.1. A summary of the original SOM patterns and how they are grouped as circulation regimes in the main manuscript.

SOM Pattern Number	Regime Grouping
1	Reversal
2	Reversal
3	Northwesterly Wind
4	Divergent Mode
5	Data Gap
6	Northwesterly Wind
7	Northeastward-Flowing
8	Northeastward-Flowing
9	Northeastward-Flowing
10	Northeastward-Flowing
11	Northeastward-Flowing
12	Northeastward-Flowing

Appendix 2.2. Permission from co-author Rachel Potter to include manuscript in the dissertation.

UNIVERSITY
of ALASKA

Ying Chih Fang <yfang2@alaska.edu>

Permission to use manuscripts in my dissertation

Rachel Potter <rapotter@alaska.edu>   Wed, Oct 25, 2017 at 1:38 PM
To: Ying Chih Fang <yfang2@alaska.edu>

Dear, Fang,

You certainly have my permission to include *Quality Assessment of HF Radar-Derived Surface Currents Using Optimal Interpolation* and *Surface Current Patterns in the Northeastern Chukchi Sea and Their Response to Wind Forcing* in your dissertation.

Thank you,
Rachel

_____

Rachel Potter
University of Alaska Fairbanks
College of Fisheries and Ocean Sciences
PO Box 757220
Fairbanks, AK 99775-7220
907-474-5709 (Phone)
http://www.uaf.edu/cfos/
http://www.chukchicurrents.com

[Quoted text hidden]

Appendix 2.3. Permission from co-author Hank Statscewich to include manuscript in the dissertation.

UNIVERSITY
of ALASKA

Ying Chih Fang <yfang2@alaska.edu>

Permission to use manuscripts in my dissertation

Hank Statscewich <hstatscewich@alaska.edu> Wed, Oct 25, 2017 at 1:38 PM
To: Ying Chih Fang <yfang2@alaska.edu>
Cc: Rachel Potter <rapotter@alaska.edu>

Fang,
You have my permission to include these two papers as a part of your dissertation. Congratulations on completing your Ph.D!
Hank

On Wed, Oct 25, 2017 at 1:27 PM, Ying Chih Fang <yfang2@alaska.edu> wrote:
Hello Rachel and Hank,

You both are co-authors on two manuscripts that I want to include in my dissertation to fulfill the requirements of a PhD in Oceanography from the University of Alaska Fairbanks.

The first one is titled "QUALITY ASSESSMENT OF HF RADAR-DERIVED SURFACE CURRENTS USING OPTIMAL INTERPOLATION"; and the second one is titled "SURFACE CURRENT PATTERNS IN THE NORTHEASTERN CHUKCHI SEA AND THEIR RESPONSE TO WIND FORCING".

Please reply to this email and indicate whether you grant permission to include these 2 papers.

Thank you very much,
Fang
--

Ying-Chih Fang 方盈智

Graduate Student (Oceanography)

College of Fisheries and Ocean Sciences (CFOS)

University of Alaska Fairbanks

Fairbanks, Alaska, USA

E-mail: yfang2@alaska.edu

Appendix 2.4. Permission from co-author Brita Irving to include manuscript in the dissertation.

UNIVERSITY
of ALASKA

Ying Chih Fang <yfang2@alaska.edu>

Permission to use manuscript in my dissertation

Brita Irving <bkirving@alaska.edu>   Wed, Oct 25, 2017 at 1:32 PM
To: Ying Chih Fang <yfang2@alaska.edu>

Hi Fang,

You have my permission to use the manuscript in your dissertation. Congratulations!

On Wed, Oct 25, 2017 at 1:30 PM, Ying Chih Fang <yfang2@alaska.edu> wrote:
Hello Brita,

You are a co-author on one manuscript that I want to include in my dissertation to fulfill the requirements of a PhD in Oceanography from the University of Alaska Fairbanks.

The paper is titled "SURFACE CURRENT PATTERNS IN THE NORTHEASTERN CHUKCHI SEA AND THEIR RESPONSE TO WIND FORCING".

Please reply to this email and indicate whether you grant permission to include the paper.

Thank you very much,
Fang

--

Ying-Chih Fang 方盈智

Graduate Student (Oceanography)

College of Fisheries and Ocean Sciences (CFOS)

University of Alaska Fairbanks

Fairbanks, Alaska, USA

E-mail: yfang2@alaska.edu

CHAPTER 3: Low-frequency Flow Variability of the Hanna Shoal Region in the Northeastern Chukchi Sea[3]

3.1 Abstract

We analyze velocity and hydrographic observations derived from 23 moorings from 2011–2014 on the northeastern Chukchi shelf. The focus is on subtidal circulation dynamics in the Hanna Shoal region. Along the east side of Hanna Shoal the velocity field is often strongly vertically sheared with the upper layer flow to the northwest and the lower layer flowing southward. The sheared flow is a result of heavy stratification induced by dilute ice meltwaters overlaying cold, salty winter-formed waters. In sharp contrast to the shelf west and south of Hanna Shoal, the stratification east of the Shoal likely persists year-round, especially if ice persists over the Shoal through late summer. Wind-forced Ekman currents and a baroclinic pressure gradient are responsible for the mean upper-layer flow. Whereas bottom currents are southward and arise as a consequence of the barotropic forcing due to the sea-level difference between the Pacific and Arctic oceans. Along the western side of the Shoal, the flow is weakly sheared and seasonally stratified, with complete stratification breakdown in early winter. In winter, a seasonally-variable, along-isobath density gradient develops that impels a cross-isobath flow along the bottom, while the mean flow in the upper water column suggests convergence on the northern side of Hanna Shoal. Both features imply that shelf-basin exchange may occur north of Hanna Shoal.

At shorter periods, the circulation around the Shoal is altered by the passage of barotropic, topographic waves of ~3 day period, triggered by strong surface stress impulses. The waves propagate clockwise around the Shoal from the east side, but the signal is damped along the northwest side of the Shoal and near Barrow Canyon. The absence of the wave in these regions is likely due to scattering, convergence in potential vorticity (PV) contours, and/or blocking by large PV gradients.

---

[3] Prepared for submission to Progress in Oceanography as Y.-C. Fang, T. J. Weingartner, E. L. Dobbins, P. Winsor, H. Statscewich, R. A. Potter, T. Mudge, C. A. Stoudt, and K. Borg, "Low-frequency Flow Variability of the Hanna Shoal Region in the Northeastern Chukchi Sea".

3.2 Introduction

Pacific waters, propelled by the poleward pressure gradient between the Pacific and Arctic Oceans (Aagaard et al. 2006; Stigebrandt 1984; Woodgate et al. 2005), flow northward from Bering Strait across the Chukchi Sea shelf. These waters substantially influence the sea ice and ecosystem of the Chukchi shelf and the Arctic Ocean (e.g., Blanchard et al. 2017; Grebmeier et al. 2015; Shimada et al. 2006; Wood et al. 2015; Woodgate et al. 2010). On average the Pacific inflow is ~1 Sv (Roach et al. 1995; Woodgate 2005; Woodgate et al. 2012) with maximum transport (~1.3 Sv) in summer and minimum (~0.4 Sv) in winter (Woodgate 2005). Observations (e.g., Pickart et al. 2010, 2016; Weingartner et al. 2005; Woodgate et al. 2005) and numerical models (Winsor and Chapman 2004; Spall 2007) indicate that the Pacific inflow is topographically steered along three major pathways (Figure 3.1a). One branch flows through Hope Valley and Herald Canyon, another flows northeastward along the Alaskan coast and exits the shelf through Barrow Canyon. and the third flows northward through the Central Channel (Figure 3.1a). The focus of this paper is Hanna Shoal, which lies at the northern end of the Central Channel or ~200 km northwest of Barrow. The Shoal is a west-east oriented oval ~150 km on its major axis and ~55 km on its minor axis (as defined by the 40 m isobath). The shelfbreak (~100 m isobath) lies 75 km to the north, and the broad, gently sloping central shelf of 40–45 m depth is to the south. Minimum depths atop the Shoal are ~20 m and shallow enough to ground sea ice with deep keels, as evidenced by the heavily scoured gravelly seabed (Grantz and Eittreim 1979).

The waters surrounding Hanna Shoal support a rich benthic ecosystem of considerable importance to walrus and other benthic-feeding organisms (Grebmeier et al. 2015; Blanchard et al. 2017). In addition, heavy and/or persistent sea ice cover often encapsulates the Shoal through summer (Martin and Drucker 1997), which provides important habitat for a diversity of ice-obligate and ice-associated species (Moore and Huntington 2008; Moore et al. in press) that feed over the surrounding waters. Dunton et al. (2017) suggest that the regional circulation and hydrography are critical in supporting the productivity of the Hanna Shoal area.

Barotropic models (Winsor and Chapman 2004; Spall 2007) suggest that some of the flow from the Central Channel, along with a portion of the eastward-flowing outflow from

Herald Valley, flows clockwise around the western flank of the Shoal but weakens on the eastern side of the Shoal due to isobathic divergence. Previous measurements indicate that the flow over the shelf east of the Central Channel and south of Hanna Shoal is predominantly barotropic (Weingartner et al. 2005, 2013a). Here the surface current response time to wind forcing is ~1 day, consistent with barotropic geostrophic adjustment in the presence of bottom friction (Fang et al. accepted; Chapter 2 of this dissertation). On the northeast side of the Shoal, baroclinic effects that oppose the clockwise circulation may be substantial (Weingartner et al. 2017a), and the surface currents are Ekman-like and respond within a few hours to the winds (Fang et al. accepted). Current and hydrographic measurements (Weingartner et al. 2013a, 2017a; Pickart et al. 2016) suggest an eastward flow emanating from the Central Channel along the southern flank of the Shoal. These two branches presumably merge somewhere southeast of the Shoal and eventually continue eastward toward Barrow Canyon to join the northeastward-flowing coastal pathway. The rapidity of the shelf circulation response to winds can cause substantial variability in the flow and thermohaline structure (Woodgate et al. 2005; Weingartner et al. 2005; Pisareva et al. 2015). Sufficiently strong northeasterly winds can induce upcanyon (southwestward) flow in Barrow Canyon (e.g., Itoh et al. 2013; Johnson 1989; Weingartner et al. 2017b) and broad-scale, sustained flow reversals over the shelf (Weingartner et al. 1998; Woodgate et al. 2005).

Grounded sea ice atop Hanna Shoal has an important influence on the regional hydrography (Weingartner et al. 2017a). Wind-induced divergent ice movements promote leads or latent heat polynyas (e.g., Hirano et al. 2016) over the Shoal in winter, which facilitates sea ice production and, consequently, the formation of near-freezing (<-1°C), very saline (>32.5) Winter Waters (WW). In summer nutrient-rich WW is typically found within ~20–25 m above the seabed surrounding the Shoal (Danielson et al. 2017), which may enhance local photosynthesis. In summer and fall, the northward flow in the Central Channel brings warm (3–5°C) and salty (>31) Bering Sea Waters (BSW) (e.g., Gong and Pickart 2015; Weingartner et al. 2013a) to the Hanna Shoal region. Concurrently, melting sea ice creates a ~15 m thick layer comprised of cold (0–2°C), fresh (<30) meltwaters (MW) which cap the WW by forming a strong, but thin, pycnocline. When MW is present, the lateral juxtaposition of this water mass and BSW forms a front that extends from the southwestern side of Hanna Shoal eastward along ~71.5°N to the western wall of Barrow Canyon (Weingartner et al. 2013a, 2017a). Idealized

models find that this frontal system is favorable to baroclinic instability and the formation of mesoscale motions and intrapycnocline eddies (Lu et al. 2015).

Although considerable progress has been made over the past two decades in understanding circulation processes over portions of the Chukchi shelf, the region around Hanna Shoal has been comparatively understudied due to heavy summer ice concentrations. Herein, we use moored current meter data collected from around Hanna Shoal from 2011–2014 to examine the spatial structure and the temporal variability in the regional circulation in response to synoptic and seasonal variations in forcing. The data set contains 23 current meter moorings deployed in the area. Although not all the data are contemporaneous, they afford a broad perspective on the regional circulation across different seasons and years. The paper is arranged as follows. Mooring configuration and analysis techniques are described in Section 3.3. Hydrographic properties and mean circulation patterns under different wind regimes are presented in Section 3.4. We also present the results of correlation analysis and findings from a complex empirical orthogonal function analysis, which suggests there are occasionally trapped propagating signals around Hanna Shoal. Section 3.5 discusses the results and associated dynamics, and Section 3.6 summarizes the study.

3.3. Data and Methods

3.3.1 Moorings

Three groups of moorings comprise the current velocity data sets (Figure 3.1b) and are denoted by the acronyms ASL (ASL Environmental Sciences), BC (Barrow Canyon), and COMIDA (Chukchi Offshore Monitoring in Drilling Area) in accordance with the different programs that processed them. ASL moorings were funded by the oil industry, BC moorings were jointly funded by the Bureau of Ocean Energy Management (BOEM) and oil industry, and the COMIDA array was funded by BOEM. The moorings, with variable record lengths, were emplaced from August 2011 to September 2014. In general, each mooring was equipped with Teledyne RDI 300 kHz or 600 kHz upward-looking ADCP (acoustic Doppler current profiler) situated ~3 m above the sea floor, with vertical coverage ranging from ~5 m below the surface to near-bottom. Temporal and vertical resolutions of the current velocities for the BC and

COMIDA moorings were 15–60 minutes and 1 m, respectively. For the ASL moorings, currents were determined at three depths; near-bottom, mid-depth, and near-surface. Data acquisition procedures for the ASL moorings are given by Mudge et al. (2015) and those for the COMIDA and BC moorings are documented in Weingartner et al. (2016) and Weingartner et al. (2013b), respectively. Mooring configurations, locations, period of records, and vertical coverages are summarized in Table 3.1.

Data gaps were temporally random and generally <~3 hours in duration. The data was gap-free at depths deeper than ~15 m, but gaps totaling 2 to 8% of the record length were present at ~10 m depth and were very large (≥~30% of the record length) at near-surface depths (≤~5 m). Therefore we did not use data at depths shallower than 10 m. Existing gaps <10% of the record length were subjected to a gap-filling approach (Beckers and Rixen 2003) if the total length of all gaps are <10% of the record length. This technique uses the data variance to fill gaps and as such is more statistically reliable than linear interpolation. After filling the gaps, we subsampled the time series to hourly intervals and then generated low-frequency currents by filtering with a 40-hour cutoff low-pass filter. Only the filtered, low frequency currents are considered unless otherwise explicitly stated. To explore spatial differences in the vertical velocity structure around Hanna Shoal, we computed the fraction of variance accounted for by the barotropic component from the COMIDA moorings following Edwards and Seim (2008).

For the purpose of presenting shelf-wide circulation patterns from all contemporary observations, we define the following three periods for analyses: 28 August 2011–24 June 2012 is the 2011–12 period; 11 Sep 2012–24 June 2013 is the 2012–13 period; and 9 September 2013–16 June 2014 is the 2013–14 period.

3.3.2 Hydrography

Although Table 3.1 indicates that multiple moorings were equipped with temperature and conductivity sensors, we only present *in situ* temperature/salinity measurements collected from SeaBird IM-37 MicroCAT Recorders mounted on the COMIDA NW50 and NE50 moorings. The reason for this is that the NE50 mooring measured thermohaline information at two different depths, which enables us to evaluate the strength of the stratification in the water column. Data

from NW50 are used, in addition to NE50, to determine thermohaline responses from the western side of the Shoal, so spatial variation between the two sides of the Shoal can be investigated. The original time series was at 1–15 minutes resolution and de-spiked before forming daily averaged time series.

3.3.3 Winds

We used the 10-m surface wind field at spatial and temporal resolutions of ~35 km and 3 hour, respectively, from North American Regional Reanalysis (NARR) model (Mesinger et al. 2006). The NARR grid point (yellow diamond in Figure 3.1a) closest to the NE40 mooring was selected as representative of local winds. Winds from 2010–2014 were collected and low-pass filtered with 40-hour cutoff period.

3.3.4 Surface stress resulted from winds and ice

The ADCPs on the COMIDA moorings were programmed in bottom-tracking mode to allow derivation of the ice concentration and velocity. The methodology follows that of Visbeck and Fischer (1994), and the detailed procedures are given by Stoudt (2015). Time series of ice concentration from the COMIDA moorings were given in Weingartner et al. (2016). Here we use the winds and ice velocities to form total surface stress following Yang (2006), which is then used as a parameter in investigating barotropic signals from the COMIDA moorings (Section 3.4.7).

3.3.5 Correlation and Complex Empirical Orthogonal Function analyses

Correlations between winds and currents were computed using the lagged complex correlation approach of Paduan and Rosenfeld (1996). Analysis of complex empirical orthogonal functions (CEOFs) is a technique based on the Hilbert transform and was used in examining propagating, wave-like features at a ~3 day period in the collected velocity measurements. This method can extract nonstationary narrow-band signals and has been applied to both atmospheric (e.g., Barnett 1983) and oceanographic (e.g., Auad and Hendershott 1997; Chavanne et al. 2010) data.

106

Briefly, the CEOF analyses proceeded as follows. Each velocity component time series near the ~25 m depth was filtered with a 50–100 hour pass band. This depth was chosen because it is the most common among the various moorings. We will show that the signal is nearly barotropic, thus the choice of depths is independent of the analysis. Filtered time series were Hilbert transformed and then used to create a covariance matrix for EOF computation (e.g., Kaihatu et al. 1998). The resultant eigenvectors are complex with the imaginary component 90° out-of-phase with the real component. Time series of the modal amplitude and phase of Mode 1 were also formed to examine the propagating signal. For all three observational periods, EOF Mode 1 explains ~70% of the total variance, whereas Mode 2 is only ~10%; hence, only Mode 1 results are presented.

3.4 Results

3.4.1 Winds

We begin by showing a 5-year time series of local winds from January 2010–December 2014 (Figure 3.2). Northerly and northeasterly winds predominated, although these were interspersed with episodes of southeasterly and southerly events. Mean winds over the 5-year period were ~2.0 m s^{-1} toward ~245°T. For the three time periods defined in Section 3.3.1, the record-length mean winds for all years combined were northeasterly (~237°T) at ~1.6 m s^{-1} with no substantial differences found among these periods.

We divided each of the three periods into segments of partially and completely ice-covered months based on the COMIDA ADCP data (see Weingartner et al. 2016). The months of June through November are defined as partially ice-covered, whereas completely ice-covered months range from December to May. Note that open-water seasons are included in the partially ice-covered months. Wind statistics for the ice-covered or partially ice-covered months did not yield significant differences. Principal axes and mean velocities showed a predominance of northeasterly winds (217–248°T) with speeds >7 m s^{-1}. However, in June–November 2012 mean winds were relatively weak (~0.3 m s^{-1}) and northwesterly (~149°T). Mean values of the two velocity components were not significantly different from zero at the 95% level, suggesting winds were variable during this period. This is consistent with the fact that the principal axis of

the winds in June–November 2012 only explained ~61% of the total variance, the smallest among all periods.

3.4.2 Mean circulation patterns

Figure 3.3 shows maps of the mean velocity vectors at three representative depths, along with mean winds, arranged by time period (columns) with record-length means in the top row, means for the ice-covered season in the middle row, and means for the open water/partially ice-covered season in the bottom row. The record-length mean winds for each time period were from the northeast at an average speed of $\leq$2 m s^{-1}. The maps (Figure 3.3a, d, g) are based on 300 days in 2011–12, 286 days in 2012–13, and 280 days in 2013–14. The current maps are all consistent with one another with northward flow in the Central Channel (Crackerjack), eastward flow over the central shelf south of Hanna Shoal (HS04, HS05, HS06, BC4-6, Burger, CPAI01, Statoil3, and Statoil4), and northeastward/eastward currents in Barrow Canyon (BC1-3) and along the northwest side of Hanna Shoal (HS01–03, NW40, NW50). At each of these locations the vertical velocity shear is small. On the east side of the Shoal CPAI02 shows weak eastward flow (toward Barrow Canyon) in 2011–12 over the entire water column. In 2012–13, the flow in the upper half of the water column is westward but eastward along the bottom. The flow was also strongly sheared in the vertical along the northeast side of Hanna Shoal (NE50 and NE60) in both 2012–13 and 2013–14, with the bottom flow southward at all locations while the upper layers were northwestward (NE50 and NE60).

For the ice-covered season (182–183 days per year) mean winds ranged from 1.0–2.2 m s^{-1} from the northeast; however, the circulation maps (Figure 3.3b, e h) show considerably more interannual variability. In 2011–12, the flow in Barrow Canyon was weak or slightly to the southwest, while flow over the central shelf was weakly eastward, and in fact not statistically different from zero. Presumably the southwestward flow along the coast turned offshore somewhere farther south along the coast. However, currents in the Central Channel were still northward and those along the northwest side of Hanna Shoal were northeastward. Currents at these two locations were similar during the later years, even though quite different flow conditions prevailed elsewhere. For example, in 2012–13, the mean flow was southwestward in Barrow Canyon, while flow over the central shelf was mostly northward. Northeast of Hanna

Shoal the bottom flow was southward at NE50 and NE60, but northward in the upper half of the water column and northward throughout the (shallower) water column at NE40. At CPAI02, the flow was westward at the surface, a minimum at mid-depth and eastward at the bottom. In 2013–14, the flow in both Barrow Canyon and over the central shelf was eastward while in the Central Channel and along the northwest side of Hanna Shoal it was again northward and northeastward, respectively. On the northeast side of Hanna Shoal the flow was northwestward at all locations and depths, although swifter at the surface than at the bottom. The opposing flow directions on the east and west sides of Hanna Shoal suggest convergence along the north side of the Shoal.

The final set of maps encompasses the partially ice-covered season (Figure 3.3c, f, i), which were based on 117 (2011–12), 104 (2012–13), and 98 (2013–14) days. The mean winds during this season showed the greatest interannual variability and were 3.5 m s^{-1} from the northeast in 2011–12, 0.3 m s^{-1} from the southwest in 2012–13, and 1.8 m s^{-1} from the northeast in 2013–14. Nevertheless current directions and magnitudes were similar from year-to-year. Flow directions were also similar to the record-length means, although the magnitudes of the currents were greater during the partially ice-covered season. The latter point is not unexpected since this season includes the open water and summer season, when the transport increases in Bering Strait (Woodgate 2005) and in Barrow Canyon (Weingartner et al. 2017b).

3.4.3 Wind-induced variability

Fang et al. (accepted) found that northeasterly winds ≥~6 m s^{-1} are critical for reversing surface circulation over the northeastern Chukchi Sea shelf from flow eastward over the central shelf and northeastward in Barrow Canyon to westward and southwestward over these regions, respectively. They also showed that northwesterly winds ≥~6 m s^{-1}, although of relatively infrequent occurrence, generate southward flow over the entire shelf. Fang et al. (accepted) found that winds ≤4 m s^{-1} do not substantially change the background surface current field over the northeastern shelf. Thus, it is of interest to investigate the response of subsurface currents to northeasterly and northwesterly winds. We formed composite circulation patterns of the subsurface currents based on the following wind criteria: the northeasterly regime having wind directions towards the southwest sector (≥180°T and ≤270°T) and at speeds ≥4 m s^{-1}, the northwesterly regime with wind directions toward the southeast sector (≥90°T and <180°T) at

speeds ≥ 4 m s^{-1}, and the normal regime with wind fields exclusive of the preceding two conditions. A comparison of the two wind-related regimes with the normal regime shows wind-induced flow variations.

Figure 3.4 shows the averaged currents at three representative depths under each regime (aligned in separate rows) for the 2011–12, 2012–13, and 2013–14 periods (aligned in columns). The normal regime is shown in the top row (Figures 3.4a, d, and g), the northeasterly regime in the middle row (Figures 3.4b, e, and h), and the northwesterly regime in the bottom row (Figures 3.4c, e, and i). These composites are based on 13,950 hours that satisfy the normal regime wind criteria, 5,507 hours for the northeasterly regime, and 1,087 hours for the northwesterly regime.

3.4.3.1 The normal regime

For the normal regime (Figure 3.4a, d, g) the mean winds were <1 m s^{-1} from either the northeast or southeast. The flow pattern under this regime is similar to the record-length means (Figure 3.3a, d, g). The flow is northward in the Central Channel (Crackerjack) and eastward over the central shelf south of Hanna Shoal (HS04, HS05, HS06 BC4–6, Burger, CPAI01, Statoil3, and Statoil4), indicating the connectivity between Central Channel and Barrow Canyon. This eastward flow turns abruptly to the northeast and accelerates at the head of Barrow Canyon (BC1–3). Here the flow presumably merges with nearshore flow moving northeastward along the coast. There is also northeastward flow rounding the northwest corner of the Shoal (HS01, HS02, NW40, and NW50), with negligible flow atop Hanna Shoal (HS03). At all locations the vertical velocity shear is negligible, except on the eastern side of the Shoal where the picture is more complicated. At NE40 currents at all depths are southward, consistent with the notion of a clockwise circulation around the Shoal, but farther to the northeast at NE50 and NE60 (2012–13 and 2013–14) the flow in the upper half of the water column was northwestward consistent with the baroclinic forcing documented by (Weingartner et al. 2017a) during cruises in August 2012 and 2013. The bottom currents at these two moorings were weakly southward in 2012–13 but weakly westward in 2013–14. Currents southeast of the Shoal (mooring CPAI02) were weak (~1 cm s^{-1}) and eastward at all depths in 2011–12. In 2012–13 (Figure 3.4d), the bottom currents were also eastward but much stronger (~5 cm s^{-1}), while the surface currents were weak and eastward.

3.4.3.2 The northeasterly and northwesterly regimes

In each year the mean winds for the northeasterly regime (Figure 3.4b, e, h) were ~6 m s^{-1}. Under these winds the flow is reversed over the entire shelf south of Hanna Shoal and in Barrow Canyon. Canyon waters flow swiftly southwestward at the surface and bottom. This figure suggests that waters flowing up Barrow Canyon, along with coastal waters, feed the central shelf and the Central Channel. The flow in the Central Channel (Crackerjack) assumes a northwestward current at all depths. Interestingly the flow on the northwest side of Hanna Shoal remains northeastward (northward/northwestward near the surface), except atop the shoal (HS03), where the flow is westward at all depths. On the northeast side of Hanna Shoal the bottom flow is southward everywhere (NE40, 50, and 60) while flow in the upper half of the water column is northward/northwestward. Southeast of Hanna Shoal (CPAI02), the bottom flow is westward, while flow in the upper half of the water column is northwestward. In all cases flow is strongly sheared in the vertical except in the Central Channel (Crackerjack) and at CPAI01 in 2011–12.

The mean wind velocities for the northwesterly regime (Figure 3.4c, f, i) ranged from 4.7 (2013–14) –5.6 m s^{-1} (2012–13) to the southeast. The circulation pattern under these winds is less consistent from year-to-year, in part because northwesterly winds are infrequent and their durations are relatively short (<2 days versus >3 days for northeasterly winds) such that the flow may not have completely adjusted in some cases. The flow pattern consists of southward/southwestward upper ocean currents over the central shelf during the first two years, whereas in 2013–14 these tended to have a more eastward flow. In 2011–12 the bottom currents were also southward, but in 2012–13 these veered eastward or southeastward, and in 2013–14 they were swift and more southeastward at Burger.

3.4.4 Spatial coherence structure

An overview of the circulation spatial coherence is afforded by empirical orthogonal functions (EOFs) using the record length velocity time series rotated onto the major principal axis of each mooring. We show results from the 2012–13 period using the near-bottom vectors as these provide the best coverage around Hanna Shoal and the central shelf. The near-surface

vectors were also analyzed and yielded similar results. Sensitivity experiments show that mooring sites on the Shoal proper (<~40 m isobath) gave ambiguous results, and resultant eigenvectors were sensitive to input data. Therefore, the moorings used are Crackerjack, CPAI01, CPAI02, Burger, NW50, NE50, NE60, Statoil4, and BC2. We present EOF Modes 1–3 along with their temporal amplitude times series versus winds rotated onto the major principal axis in Figure 3.5. The first mode explains 39% of the variance, and the eigenvector weights are largest south and southeast of Hanna Shoal (e.g., Crackerjack, Burger, BC2, and CPAI02). Eigenvectors for the COMIDA moorings (NW50, NE50, and NE60) are smaller. The second mode explains 24% of the variance and shows a complicated pattern. Mode 3 captures 16% of the variance, showing relatively large eigenvectors at NW50, NE50, NE60, and BC2.

We correlate the modal temporal amplitudes to the rotated winds. The results indicate only Modes 1 and 2 are associated with winds (the estimated 95% significant level is ~0.2). To interpret the eigenvectors more carefully, the modal temporal amplitude is correlated with the rotated currents so that we can evaluate how well the eigenvectors capture the variance. Mode 1 represents about half of the variability for all moorings except NW50. Thus, the flow at NW50 may originate from Herald Canyon and is not associated with Mode 1. The highest correlation (0.92) appears at CPAI01 (near Central Channel), denoting large-scale flow on the shelf. There is low but significant correlation between temporal amplitude of Mode 1 and rotated winds, suggesting that this pattern is mainly dominated by the background pressure gradient.

The correlation between Mode 2 temporal amplitude and rotated currents were largest at NW50 (0.51), NE50 (0.50), Statoil4 (0.79), and BC2 (0.83), whereas for Crackerjack the correlation is very low (<0.05). Sites with higher correlations are close to Hanna Shoal and in Barrow Canyon. Thus Mode 2 may be interpreted as the Hanna Shoal mode and is significantly correlated with the winds, suggesting that it represents wind-induced variations. We find NE50 and NE60 are out-of-phase with NW50, implying systematic divergence/convergence along the northern side of the Shoal.

Mode 3 has very little correlation with winds and largely explains variability at NW50, NE50, NE60, and CPAI02. Again eigenvectors at NW50, NE50, and NE60 are out-of-phase. The origin of this mode is unclear, although it may be linked to the cross-isobath baroclinic pressure

gradients, greatest along the eastern side of Hanna Shoal, and to the along-isobath baroclinic pressure gradients, present in winter and discussed in Section 3.5.

3.4.5 Hydrography

In this section we present seasonal changes in the thermohaline properties along the northwest (NW50) and northeast (NE50) sides of Hanna Shoal. Temperature and salinity variations in Barrow Canyon were addressed by Weingartner et al. (1998, 2017b), and those on the central shelf and western Chukchi Sea were analyzed by Woodgate et al. (2005) and Weingartner et al. (2005). Figure 3.6 shows the 2012–2014 time series of winds, bottom currents, and bottom temperatures and salinities at NW50. (Temporal changes in temperature and salinity at NW40 paralleled those at NW50 and are not shown.).

In August 2012 and 2013 the water column was heavily stratified over the shelf immediately surrounding and to the north of Hanna Shoal, where surface meltwaters overlaid dense bottom waters (Weingartner et al. 2017a). Weingartner et al. (2017a) also identified a front that trends southeast from the west side of Hanna Shoal and thence eastward toward the head of Barrow Canyon along ~71.5°N. South of the front the water column was less stratified because warm, salty waters overlaid winter waters. Whereas in 2011 the front was absent, waters were weakly stratified and consisted only of Bering Sea Summer Water.

In spite of considerable variability in the winds, bottom currents were remarkably steady at ~7 cm s^{-1} toward the northeast throughout the 2-year record. In mid-August 2012, bottom temperatures were close to the freezing point (~-1.8°C), and salinities were ~33.5. Thereafter, temperatures gradually increased through fall and early winter to a maximum of ~0.5°C by late December, while salinities slowly decreased over the same time period. These seasonal changes in temperature and salinity were probably associated with northward advection through the Central Channel of warmer, fresher, and more weakly stratified Bering Sea Summer Water, which gradually cooled through fall as it proceeded across the shelf. Temperature and salinity decreased rapidly beginning in mid-January as temperatures dropped to the freezing point and salinities reached their annual minimum of ~31. Salinity then increased slowly to ~33 by June and maintained this value through November 2013. Somewhat similar temperature and salinity

113

transitions occurred in 2013–14 although the salinity remained more steady. Warming began in July, attained a maximum in mid-November, and then rapidly decreased to the freezing point by early December. Again rapid cooling was accompanied by a salinity decrease from 32.5 to 31.5. The abrupt fall and/or late winter temperature and salinity decreases are similar to the seasonal temperature and salinity changes observed south of Hanna Shoal (Weingartner et al. 2005) and most likely reflect a complete breakdown in stratification by cooling and wind mixing.

An important point to note in the 2012–13 time series is that the coldest and saltiest water occurred in June, well past the time when freezing typically occurs on the shelf. Hence this dense water signature is a result of horizontal advection from the southwest (Figure 3.6b) and not a consequence of local ice production. The specific source of this dense water is not known, but it could be from the Central Channel (Weingartner et al. 2005), Herald Valley (Pickart et al. 2010), or as a result of local formation atop Hanna Shoal.

Consider next the time series at NE50 (Figures 3.7). Bottom velocities were southeastward in general, particularly in 2012–13 although less so in 2013–14. In 2012–13, there were two MicroCATs, which measured temperature and salinity at 25 m and 47 m depths. The temperature record at 25 m indicates temperatures were ~-1.2°C through October. From November through early January temperatures varied rapidly by 1°C or more, before collapsing to near-freezing point (~-1.7°C) in mid-January. Salinities were initially ~32.5 but decreased by ~2 in early November, coincident with a warm pulse. An additional decrease to ~28 occurred in early December. From January through mid-June salinities varied between 29.5 and 31.0, and temperatures were near-freezing. Salinities and temperatures increased to ~32 and -1.4°C in mid-June. This mid-depth temperature increase may be associated with penetrating solar radiation as sea ice begins breaking up and meltponds allow solar radiation to penetrate through the ice and into the water column (Light et al. 2008). Bottom temperatures and salinities evolved quite differently. Initially, temperatures were at the freezing point and salinities were ~33.5. Temperatures gradually increased and reached their maximum of -0.5°C in late December, a full month after temperatures at 25 m depth attained their maxima. Thereafter temperatures remained above the freezing point (and above those at 25 m) and salinities ranged between 31.0 and 32.0. Finally, in early June bottom temperatures fell to the freezing point, and salinities rose to about

33.0. The seasonal evolution of bottom temperatures and salinities was similar in 2013–14, but this thermohaline evolution was different than that observed at NW50.

Consider next the salinity differences between the records at 25 and 47 m (Figure 3.7d, red line), which provide an index of the stratification. In fall the vertical salinity difference between 25 and 47 m was ~1, but this increased to ~5 by mid-December. This increase came about primarily because of freshening at 25 m, even though the bottom salinity had also decreased, albeit slightly, through fall! The shallow salinity decrease was associated with increasing temperatures, which were a maximum of ~0°C in mid-December. Throughout February bottom salinities continued to decrease even though salinities increased at 25 m. In March, the salinity difference briefly reached a minimum of <1. This change coincided with a brief period of northward bottom flow, an increase in salinity at both depths, and a decrease in bottom temperatures to the freezing point. All of these changes imply advection of a less stratified water column and denser water from the south rather than local mixing. After March, the stratification increased again, due primarily to a salinity increase at the bottom. Bottom and mid-depth salinities both increased in July and remained nearly constant into August. The salinity record indicates that the vertical stratification over this portion of the Chukchi Sea shelf remains intact throughout the year, in sharp contrast to the shelf south and northwest of Hanna Shoal.

The annual collapse of bottom temperatures to the freezing point occurred at NW50 in mid-January of 2013 but two months earlier, in November 2013, the following fall. We suggest that these differences in freeze-up timing were related to differences in the onset of ice cover. Figure 3.8 shows ADCP-derived ice concentrations at NE50 and NW50. In 2012, northerly winds rapidly advected ice over the northeastern Chukchi Sea with coverage being spatially uniform at ~100% concentration by mid-November. In fall 2013, the development of 100% ice cover was much slower at NW50 and included episodic advances and retreats before finally setting up. In contrast, 100% ice cover was achieved earlier on the east side of the Shoal than in the Central Channel and on the northwest side of the Shoal. These differences in ice cover (in conjunction with the differences in stratification) on either side of the Shoal can account for the interannual differences in winter cooling at NW50. Earlier onset of ice cover on the northeast

side of the Shoal would also suppress convective mixing and the breakdown of stratification due to the insulating effect of the ice cover.

3.4.6 Correlation analysis

We investigated the relationship between wind and current vectors at all mooring locations by computing lagged complex correlations at hourly increments. Lags for more than 5 days were negligible and thus not shown. Correlation coefficients were low ($\leq$~0.1) and not significant for most moorings for the 2011–12 period (Figure 3.9). The sole exception was the near-surface correlation at CPAI01, where the zero-lag correlation was above the 95% significance level. For the 2012–13 period the wind-current correlations were significant at all depths and locations, with the largest correlations at a lag of 0.3 days. The correlations were strongest for the near-surface currents where the phase was ~80° to the right of the wind, consistent with Ekman dynamics in the upper layer. Similar correlation results were obtained for the other moorings in the 2012–13 and 2013–14 periods.

The 2012–13 CPAI02 correlation includes a plateau in the correlation function for the surface currents at a lag of ~3 days where r~0.2. A secondary peak is found at this lag in the deeper depths as well. This secondary peak was not evident at Burger or CPAI01 but was found elsewhere and was most pronounced along the eastern side of Hanna Shoal (2012–14 NE40, NE50, and NE60) (Figure 3.10). The maximum correlation at the deepest depth for NE50 occurred at 2–3 days, but peaks at this lag were not obvious at NW40 and NW50. Small secondary peaks were present in 2011–12 at HS04–06 along the south side of Hanna Shoal, with magnitudes of ~0.1.

The correlations suggest that the local current response to winds was weaker in 2011–12 than in 2012–13 and 2013–14. In the latter years there was a spatially correlated signal at a period of ~3 days with largest magnitudes along the eastern side of Hanna Shoal. We examined this 3-day signal more closely by computing the coherence squared and phase spectra of mooring pairs and depths. For spectra computed from mooring pairs (not shown) around the Shoal proper, sites along the eastern or southern sides of Hanna Shoal all showed a correlated signal occupied the band of 50–100 hours. Pairs along the southern flank of the Shoal with moorings along the

northwestern side of Hanna Shoal in 2011–12 and for the COMIDA moorings on the northwestern and northeastern sides of Hanna Shoal in the later years were again maxima in the 50–100 hour band and suggestive of clockwise propagation around the Shoal. This signal was also found in pairs between the sites near the Shoal and those near Barrow Canyon and the central shelf. Coherence squared values in this band were significant, albeit smaller, for moorings between the Shoal proper and the central shelf. In all cases, the signal was most pronounced in the u components, and the spectral shapes contained a plateau at periods of 50–100 hours. The phase differences at these periods between the COMIDA moorings and CPAI02 range from 70–120°, implying that the signal propagates southward from the COMIDA sites. If we assume an approximate period of ~75 hours, this signal would take ~20 hours to propagate from the COMIDA eastern sites to CPAI02 to induce a ~100° phase difference. The distance between NE50 and CPAI02 is about 60 km, and the implied southward propagation speed is ~0.8 m s^{-1}.

We summarized these findings by constructing a regional map of the vertical coherence spectra using the u components between near-surface and near-bottom depths at each mooring site for the 2011–12 and 2012–13 periods (Figure 3.11). These show a pattern of higher coherence squared in the 50–100 hour band along the southeastern sides of Hanna Shoal and decreasing coherence on the northwestern side of the Shoal or farther south of the Shoal. Moreover, the phase spectra (not shown) were all in-phase, indicating the signal was barotropic.

3.4.7 Topographic wave mode

In aggregate the spectral results suggest clockwise propagation around the Shoal with shallow water to the right of the propagation and velocity fluctuations vertically in-phase. These results are all consistent with those of a barotropic topographic wave. We conduct additional tests for this contention by inspecting several of the times series more closely and computing the CEOF for the various time periods. We first show ~2-year (August 2012–September 2014) time series of the mean daily total surface (based on ADCP-derived ice concentration) and wind stress, and current shear variances based on the difference between the near-surface and bottom bins (Martini et al. 2014) and 50–100 hour bandpassed currents at NE40 (Figure 3.12). Wave-like fluctuations are apparent as striped patterns of positive-negative velocities throughout the

117

vertical (in particular for the *u*-component) across the time series. Large values of shear variance coincide with large values of the wind and total stress, suggesting the wave-like signal is associated with pulses in the wind and/or ice movement.

We then applied the CEOF analysis to the 50–100 hour bandpassed currents at ~25 m, which is not necessarily the mid-depth position at each mooring, but rather the most common depth among them. Note that the 2011–12 BC6 mooring was not included because the data was only 2 months. All three observational periods were analyzed and yielded similar results, thus we present results primarily from the 2011–12 and 2012–13 periods, because there were more moorings available.

Figure 3.13 shows the 2011–12 CEOF results in terms of time series of temporal amplitude (PC1) of Mode 1 and the unwrapped phase for this mode, along with the mean daily winds. The PC1 time series often varies with shifts in the wind velocity. The temporal phase varies linearly with time, and a linear least squares fit to this curve yields a period of ~3.1 days (74 hours). We overlaid isolines of potential vorticity (i.e., f/h, where f is the local Coriolis parameter and h is the local depth) with eigenvectors because phase propagation for a topographic wave follows f/h contours rather than bathymetry (Figure 3.14). The complex spatial eigenvectors show a phase difference of ~90° for real and imaginary parts at sites near the southern flank of Hanna Shoal. Similar results of spatial eigenvectors were given by Auad and Hendershott (1997), in which complex eigenvectors indicated a westward propagating wave in the Santa Barbara Channel. We also computed the spatial phases of the *u*-components (Figure 3.14) and found that the phase increased from the east to the west. There is also a suggestion of increasing phase to sites south of CPAI02, for example at HS06, BC4, and BC5. This increase in phase is halted at BC3 and at moorings BC2 and BC1, where the eigenvectors have >>90° phase difference, suggesting the wave did not pass here.

Results from the 2012–13 CEOF analyses are shown in Figure 3.15. The PC1 values again vary with time with the largest values corresponding with the striped patterns in the velocity time series (Figure 3.12). For example, the large PC1 values in late September 2012 coincided with the occurrence of the wave-like signal in the velocity data. Similar to 2011–12, these signals are associated with stress transitions. Time series of temporal phase yielded a

118

period of ~3.2 days for the wave-like signal, similar to the 2013–14 estimate of ~3.5 days. The ~3 day period obtained from the CEOF is consistent with the coherence spectra with significant coherence in the 50–100 hour band among mooring pairs. The corresponding complex spatial eigenvectors are shown in Figure 3.16. These eigenvectors have nearly 90° phase shifts at sites east and south of Hanna Shoal. This discrepancy may be due, in part, to differences in the mid-depth selected in the analyses because the ASL and COMIDA moorings did not have common mid-depths. However, the eigenvector angles were similar among the COMIDA NE40, NE50, and NE60 moorings, as were those for the ASL moorings. Nonetheless, this pattern still indicates a propagating wave-like signal in this area, with propagation proceeding from the northeast to the southeast on the east side of Hanna Shoal and then to the west along the southern side of the Shoal.

The wave signal is absent near Barrow Canyon and along the northwest side of Hanna Shoal. We suggest that the absence of wave signals in Barrow Canyon is associated with the large f/h gradients which likely block wave propagation into this region, and in particular offshore of BC4 where the large f/h gradient begins (Figure 3.14). A similar blocking condition was documented by Miller et al. (1996) along steep bathymetry over the shelf southeast of Iceland. The wave signal is also absent or, at best, muted along the northwestern side of Hanna Shoal and discussed in Section 3.5.

3.5 Discussion

Our results suggest there are important dynamical and thermohaline differences between the eastern and western sides of Hanna Shoal and between the shelf region north and south of Hanna Shoal. For example, the east side of Hanna Shoal likely remains stratified year-round, whereas the stratification breaks down annually by late fall or early winter on the shelf south of Hanna Shoal, within the Central Channel, and along the northwest side of the Shoal. The degree of stratification on the eastern side of the Shoal depends in part on the amount of meltwater remaining over the northeastern Chukchi shelf in summer as ice retreats. In 2011, ice retreated early over the entire northeastern shelf and the stratification was weak in fall prior to freeze-up (Weingartner et al. 2017a). In 2012 and 2013, heavy ice remained over Hanna Shoal into September, which resulted in a heavily stratified water column over the Shoal. The persistent

northeastward flow originated from the Central Channel along the western side of the Shoal will eventually replace this stratified meltwater/winter water structure with less-stratified waters (Weingartner et al. 2005). As fall progresses, the weakly stratified waters will cool and mix during fall storms, homogenizing the water column (Kawaguchi et al. 2015). Steady northward advection from the Central Channel or from the western Chukchi into the area northwest of Hanna Shoal thus plays a major role in configuring the hydrography around Hanna Shoal. Through summer and fall, this flow includes warm Bering Sea Summer Waters that generally lead to an earlier retreat in sea ice both within the Central Channel and along the western part of Hanna Shoal (Martin and Drucker 1997) compared to the eastern side of the Shoal. Similarly, in fall, the flow of the warmer Bering water retards the development of sea ice, either by *in-situ* freezing or inhibiting ice advection, compared to the eastern side of the Shoal. The earlier fall presence of ice east of Hanna Shoal insulates this portion of the shelf from convective cooling and thus enhances or maintains stratification here.

Another mechanism that may affect the stratification on the eastern side of the Shoal is the westward Ekman drift of low-density surface waters from the basin and/or Barrow Canyon into the region, particularly under northwesterly and northeasterly winds (Figures 3.4e, f, h, i). This drift, along with the baroclinicity on the eastern side of the Shoal appears to be sufficiently large to overcome the upper ocean barotropic pressure gradient that tends to force clockwise flow around the Shoal. Differences in stratification are reflected in the vertical structure of the currents. Those on the eastern side of the Shoal are more sheared in the vertical, with the surface flow largely in accordance with Ekman dynamics (Fang et al., accepted). In addition there is a baroclinic tendency that impels a northwesterly flow over the upper half of the water column (Weingartner et al. 2017a). These conditions are reflected in the mean circulation and wind-regime maps of Figures 3.3 and 3.4, respectively and in the lower proportion of barotropic variance at the NE50 and NE60 moorings (Table. 3.1).

Mean circulation patterns imply flow convergence somewhere along the northern side of the Shoal over the upper portion of the water column (Figure 3.3d, g). This result is consistent with Weingartner et al. (2017a), who found northwestward baroclinic currents at the eastern side of the Shoal based on hydrographic transects measured in August of 2012 and 2013. Circulation differences on either side of the Shoal also lead to along-isobath density gradients, as implied by

120

the differences in bottom densities along the 50 m isobath (Figure 3.17) from moorings NE50 and NW50. These vary throughout the year but are largest in late fall and winter and imply an along-isobath baroclinic pressure gradient that forces cross-isobath flow. The magnitudes of these flows can be ~1 cm s^{-1} over the lower 25 m of the water column, as estimated from the thermal wind relation, and persist for several months. These cross-isobath flows will affect mass and property exchanges between the northern part of Hanna Shoal and the Arctic basin. Moreover, they have implications on the local vorticity balance due to frictional stress curl. This finding implies that northern Hanna Shoal could be important in shelf-basin exchange and deserves future study.

Weingartner et al. (2017a) reported that meltwater was completely absent from the northeastern shelf in the summer of 2011, in contrast to the thick, pervasive meltwater cap present in the summers of 2012 and 2013. These differences in meltwater distribution have potential consequence on the circulation east of Hanna Shoal, as suggested by the differences in the wind-driven response observed at CPAI02 between 2011–12 and 2012–13. The wind-current correlations were significant in the latter period but not the former. These interannual variations are also evident in Figure 3.18, which shows the progressive vector diagrams (PVD) for near-bottom and near-surface velocities at CPAI02 for the 2011–12 record and 2012–13 record. PVDs for the winds in each year did not differ substantially from one another. In 2012–13 the bottom flow was about ~2.5 times larger than that for the 2011–12 period. There was also a striking difference in the upper ocean flow between years. In 2012–13 this flow was northwestward, whereas in 2010-11 it was weakly northward. We suggest that in the presence of heavy stratification the surface and bottom boundary layers do not overlap, whereas under weakly stratified conditions they may. Our findings are consistent with Dzwonkowski et al. (2011) who showed seasonal variations in surface layer transport attributable to differences in stratification caused by solar heating. Meltwater plays a comparable role in shaping the circulation structure along the eastern side of Hanna Shoal. In this case, the interannual variability is dictated by the seasonal retreat of sea ice, and it appears that the summer meltwater influence may persist throughout the year.

Viewed in aggregate, Figure 3.3 suggests some degree of continuity in the bottom flow around the northern and eastern sides of Hanna Shoal. Indeed, these observations corroborate the

model-predicted clockwise flow around Hanna Shoal, which is driven by the barotropic pressure field established between the Pacific and Arctic oceans (Winsor and Chapman 2004; Spall 2007). This clockwise circulation appears to persist even under quite different wind conditions (Figure 3.4). On the other hand the temperature and salinity properties of the bottom waters do vary (Figures 3.6 and 3.7), at least along the 50 m isobath, which may be due to the cross-shelf exchanges hypothesized to occur along the northern side of Hanna Shoal. Nevertheless, these bottom waters ultimately turn eastward and enter Barrow Canyon, as implied in Figure 3.18. As indicated in the models, some of these dense bottom waters may derive from Herald Valley, suggesting that not all of the dense waters entering Barrow Canyon flow across the eastern or central Chukchi Sea. It remains unclear if this dense water flows laterally into the western side of Barrow Canyon along its entire length, or if it turns eastward only along the southeastern side of Hanna Shoal and enters the head of the Canyon.

Topographic waves are a consequence of the conservation of potential vorticity and are controlled by both bottom slope and stratification. The barotropic structure of the observed waves (Figure 3.12) indicates the stratification effect is not important, so the observed waves should be explicable in terms of being the fundamental Rossby mode controlled by sloping bottom (e.g., Pedlosky 1987). Under negligible stratification topographic Rossby waves approximate barotropic shelf waves (Wang and Mooers 1976). Following Beckenbach and Washburn (2004), we compute the effective beta parameter, $\beta = \alpha f/D$ due to sloping bottom, where α is the bottom slope and D is the representative local depth (~50 m). The determination of α is based on hydrographic transects along the northeast side of Hanna Shoal, where water depth increases from ~20 m in ~60 km, to yield $\beta = \sim8.7\times10^{-10}$ m^{-1} s^{-1}. This parameter is used to estimate the propagation speed for the fundamental mode as $c = 2\mu^2/\beta$, where μ is the wave frequency ($2\pi/3.2$ day^{-1}, from the average of the 3-year CEOF estimates). We find $c = \sim1.2$ m s^{-1}, close to our inferred propagation speed of ~0.8 m s^{-1} based on the coherence spectra. Most likely these waves are triggered by cross-isobath flow initiated by changes in surface stress as suggested by Figures 3.12, 3.13, and 3.15.

Although blocking resulting from large f/h gradient is feasible in explaining the lack of a wave signal in Barrow Canyon, the absence of wave signals northwest of Hanna Shoal requires a different interpretation because the f/h gradient is comparable to that on the eastern side where

the waves appear to originate. The wave scattering arguments of Yankovsky and Chapman (1995) with respect to the influence of mean current shears and variable shelf widths may be relevant. Yankovsky and Chapman (1995) showed that in the presence of mean current shear the number of potentially freely propagating wave modes is reduced, and furthermore that spreading of *f/h* contours favors propagation, whereas convergence of the *f/h* contours induces shorter scale oscillations and scattering into higher, more slowly, propagating modes. Their results are consistent with the CEOF analyses that indicate wave signals were present over the central shelf south of Hanna Shoal. As the wave propagates along the *f/h* contours south of Hanna Shoal, it will turn northwestward and approach the western side of Hanna Shoal, where the *f/h* contours converge (a narrowing shelf), scattering wave energy into higher wave modes, which may quickly decay. A similar mechanism might also occur near Barrow Canyon due to converging *f/h* contours.

3.6 Summary

We analyzed velocity and hydrographic measurements from 23 moorings of the Hanna Shoal region of the northeastern Chukchi Sea during 2011–2014 to study the interannual and seasonal circulation variability and their response to winds. Along the eastern side of Hanna Shoal the flow is vertically-sheared and strongly stratified year-round. In contrast, conditions on the western side of the Hanna Shoal consist of a weakly-sheared and weakly-stratified water column due to advection of shelf waters from the south and possibly the west. These thermohaline contrasts yield different wind-driven responses on either side of the Shoal and, in winter, result in time-varying, along-isobath density gradients that would force cross-isobath flows. In addition, the results suggest that there is zonal convergence in the upper portion of the water column. This convergence is a consequence of the barotropic tendency to force clockwise flow around the Shoal and the presence of baroclinic pressure gradients on the eastern side of the Shoal that force a counterclockwise circulation. Consequently, the northern side of Hanna Shoal may be important in shelf-basin exchanges. The amount of summer remnant sea ice has fundamental influence in shaping the strength of stratification for the coming winter and spring, which consequently determines the behaviors of wind-current responses. Finally, a barotropic, topographic wave with ~3 day period is found along the eastern side of Hanna Shoal. The waves are triggered by the onset of strong winds and/or ice movement and propagation is then

controlled by variations in the bottom slope. Once triggered, the wave propagates clockwise around the Shoal. Large bathymetric variations may block wave propagation into Barrow Canyon or scatter the wave energy along the northwestern side of Hanna Shoal.
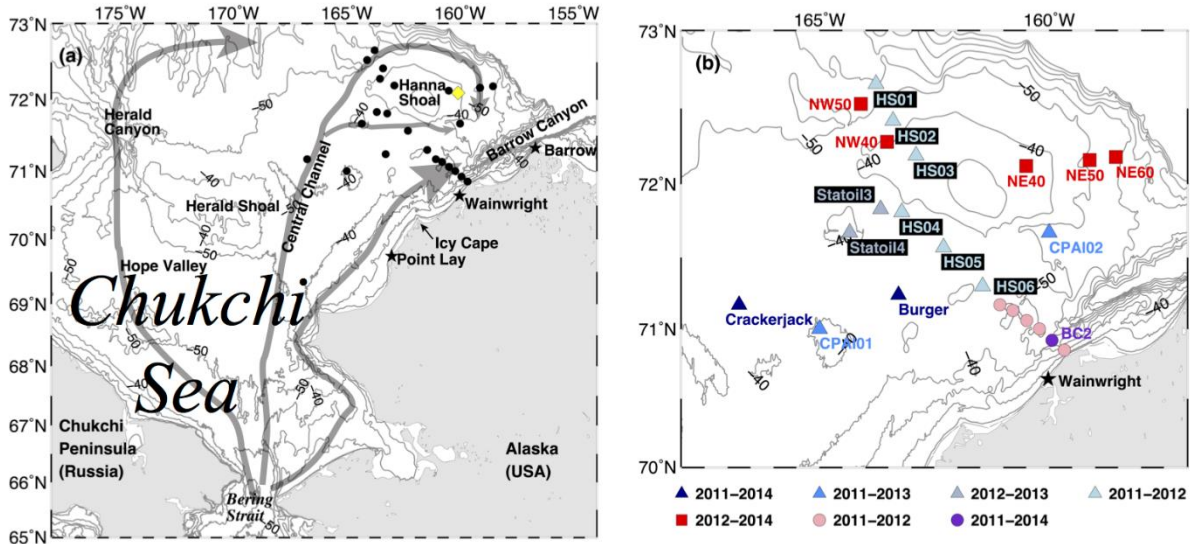
Figure 3.1. (a) Map of the Chukchi Sea with place names. Black dots indicate mooring sites. The yellow diamond denotes the NARR wind grid point representative of the shelf wind time series. Black stars denote three local villages along the Alaskan coast. Gray arrows show schematic pathways of Pacific waters. Bathymetric contours are drawn from 10–100 m at 10-m intervals. (b) Enlargement of the Hanna Shoal region and mooring sites categorized by deployment years and projects. Triangles denotes the ASL moorings, circles denote the BC moorings (BC1–BC6, with BC1 closest to the coast), and red squares indicate the COMIDA moorings. Different colors denote different temporal coverages.
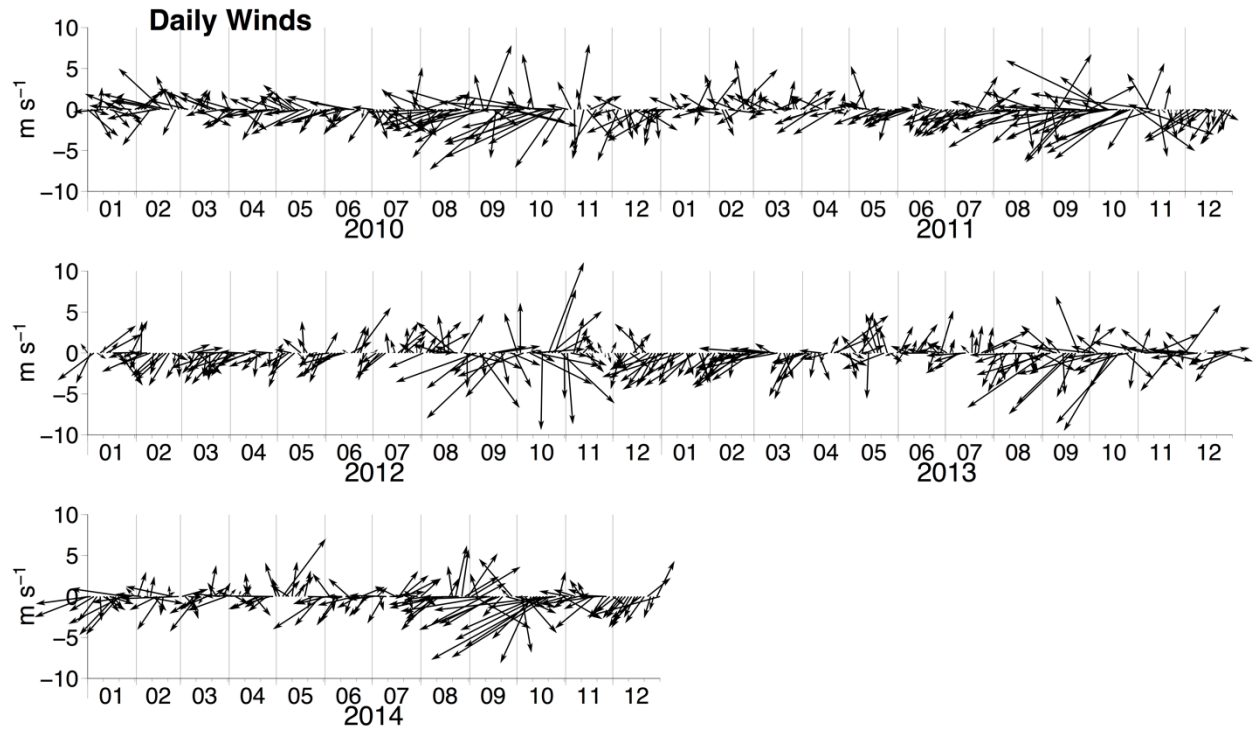
Figure 3.2. Time series of daily averaged wind vectors from January 2010–December 2014. Vector direction follows oceanographic convention. For clarity, vectors are plotted every 2 days. X-axis labels represent months.
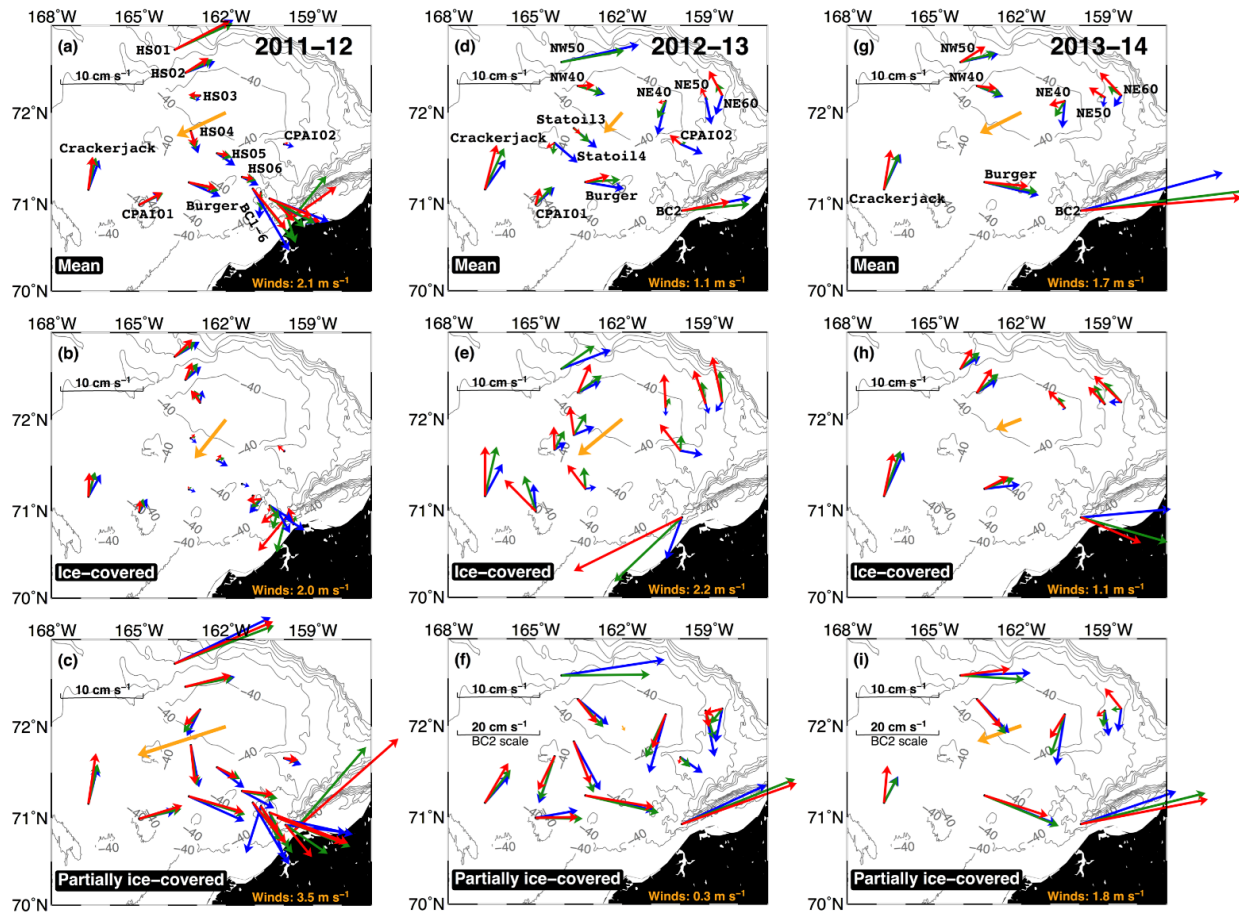
Figure 3.3. Mean velocity vectors of record length (top row), ice-covered season (middle row), and partially ice-covered season (bottom row). Each column represents a specific mooring deployment period. Red, green, and blue vectors denote currents near the surface, mid-depth, and bottom, respectively. The orange vector signifies the mean wind vector for each regime with its magnitude given in the lower right corner of each map. Note that the vector scales for Barrow Canyon (BC) currents in (f) and (i) are twice the size of the vector scale for other locations.
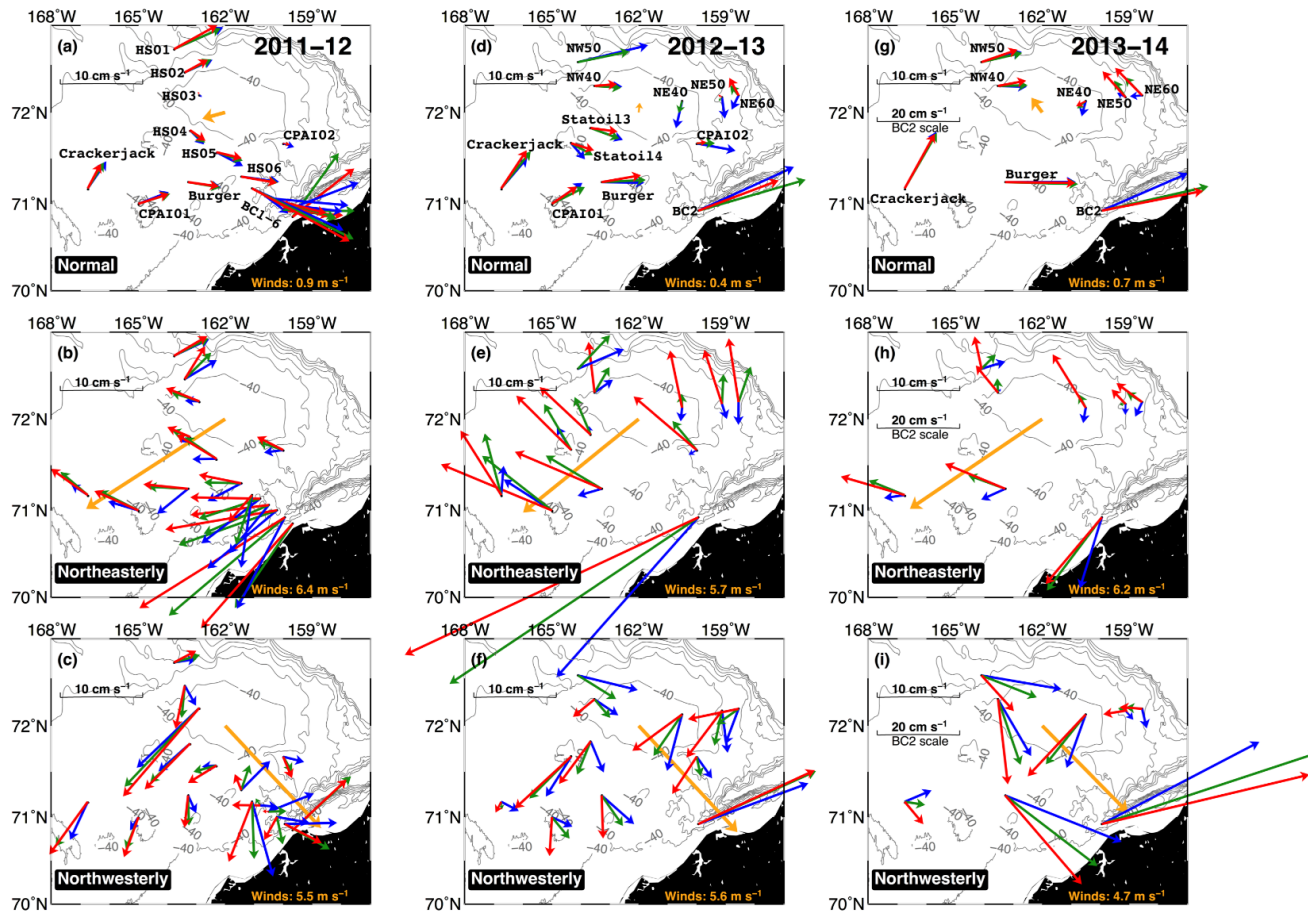
Figure 3.4. Maps of the mean velocity vectors near the surface (red), mid-depth (green), and bottom (blue) by year (columns) and by wind regime (rows). The orange vector signifies the mean wind vector for each regime with its magnitude given in the lower right corner of each map. The top row includes the various mooring names. Note that the vector scales for Barrow Canyon (BC) currents in (g)-(i) are twice the size of the vector scale for other locations.
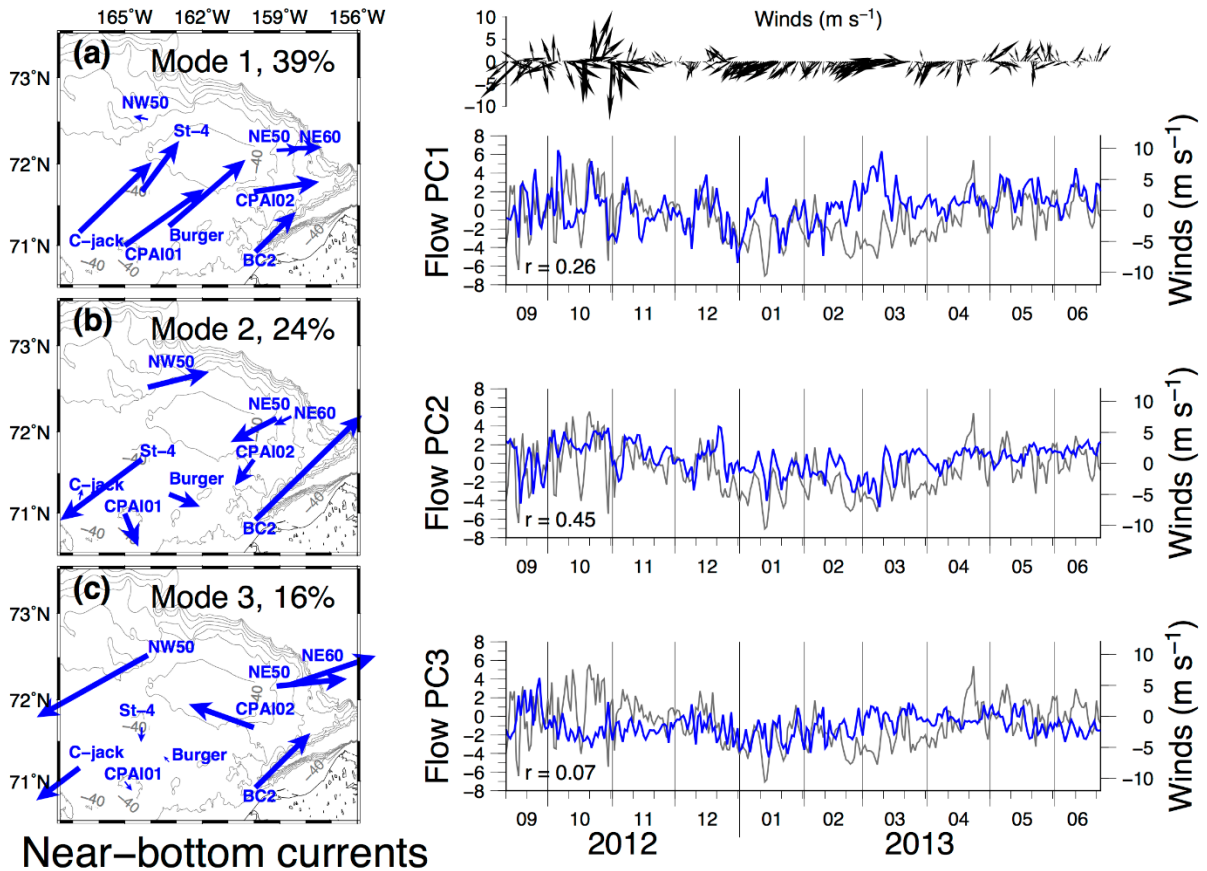
Figure 3.5. (a) Mode 1 eigenvectors and their temporal amplitude time series (to the right), along with the wind velocity along the principal axis (gray line). The correlation (r) between the time series is also shown. St-4 is for Statoil4 and C-jack is for Crackerjack. (b) as in (a), but for Mode 2. (c) as in (a), but for Mode 3. Note that the time series of wind vectors is presented above the temporal amplitude of Mode 1.
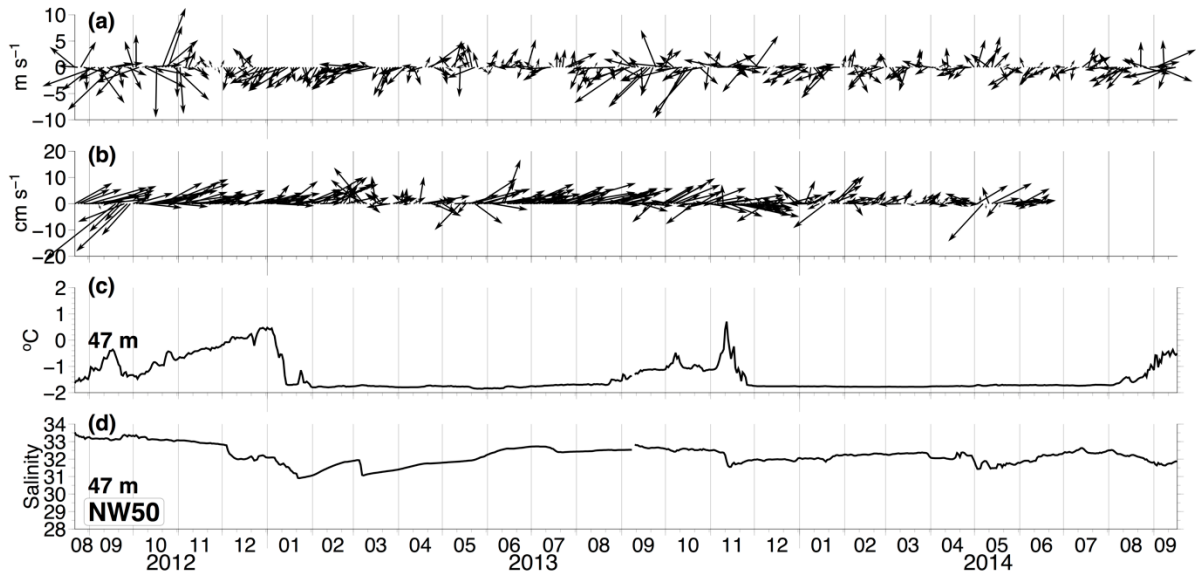
Figure 3.6. Time series of daily averaged (a) winds, (b) near-bottom currents, and (c) in situ temperature and (d) salinity at 47 m at NW50.

130
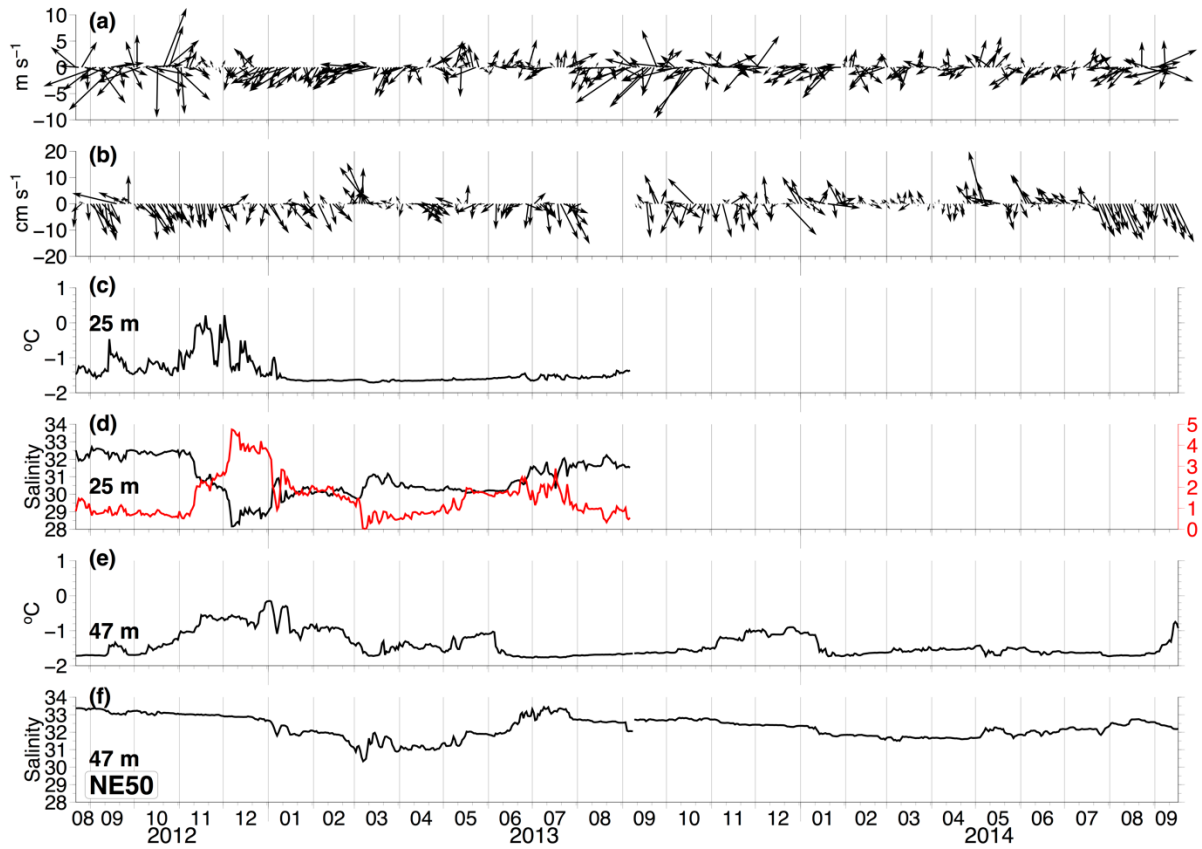
Figure 3.7. Time series of daily averaged (a) winds, (b) near-bottom currents, and (c) in situ temperature and (d) salinity at 25 m at NE50. (e)-(f) As in (c)-(d), but at 47 m. Red line in (d) denotes difference of salinity between 25 m and 47 m.
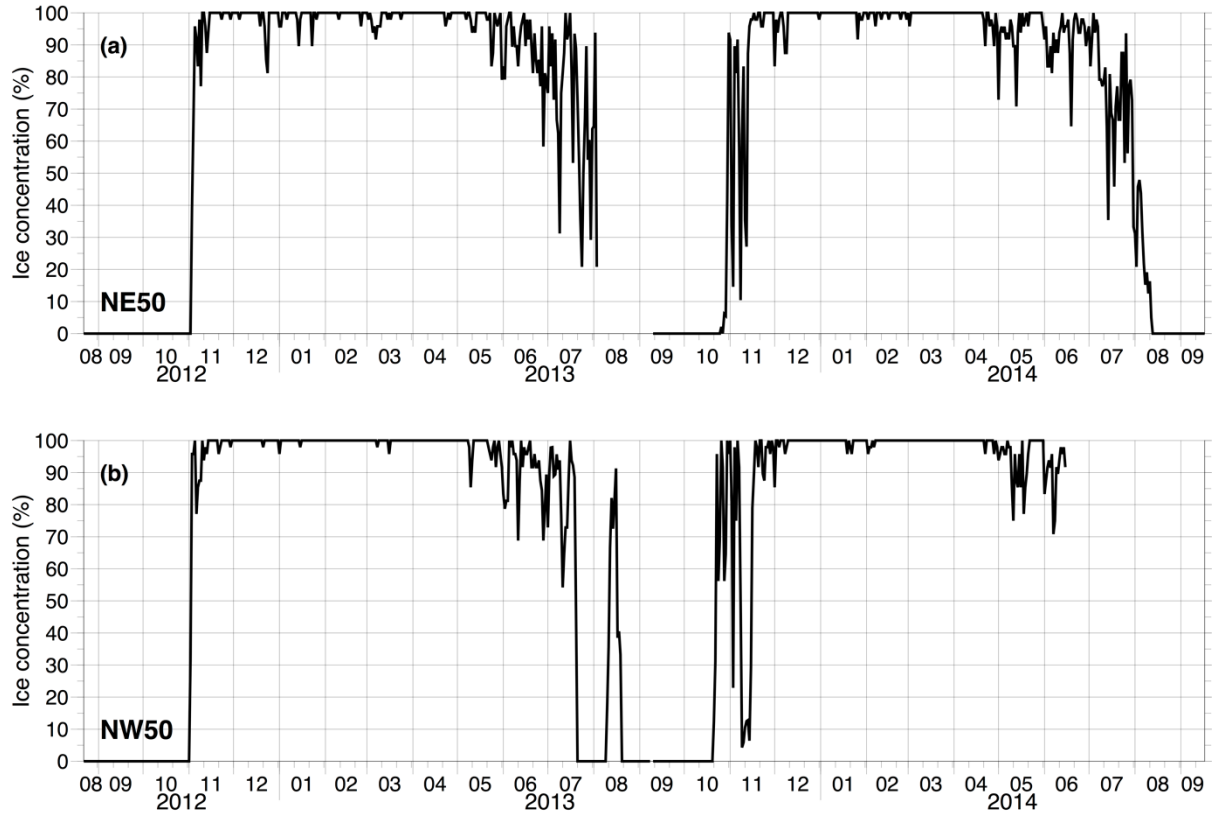
Figure 3.8. Time series of daily averaged ice concentration derived via ADCPs at (a) NE50 and (b) NW50.
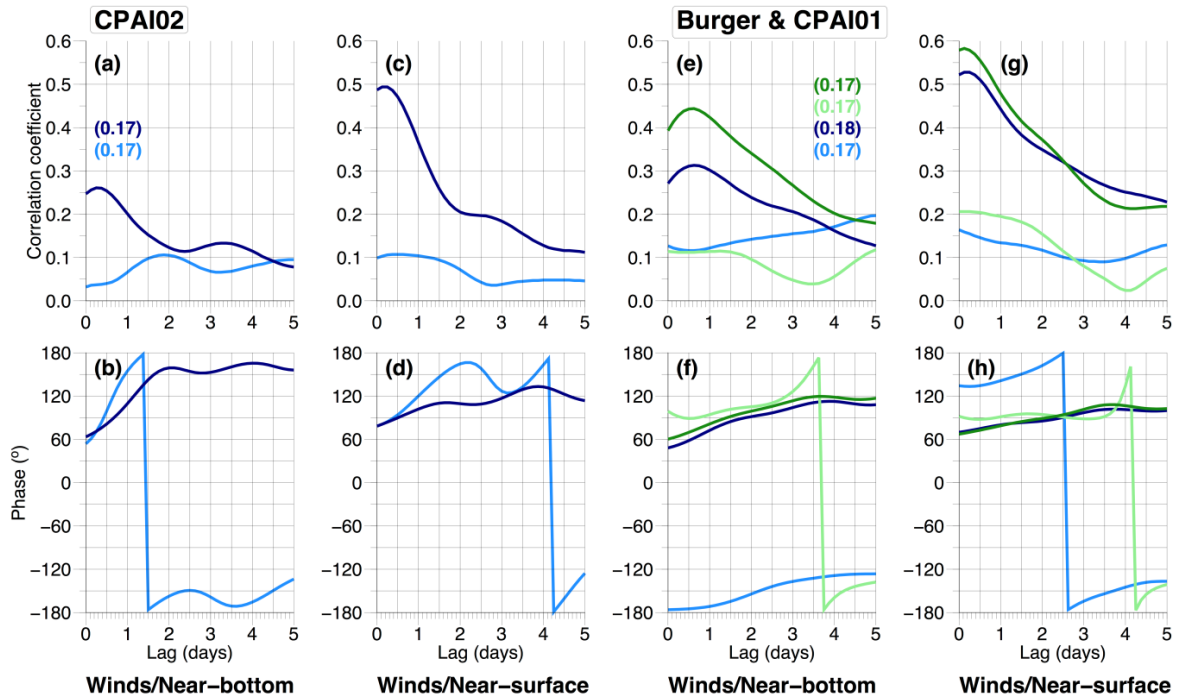
Figure 3.9. Lagged complex correlation results for 2011-12 and 2012-13 for near-bottom and near-surface currents. Top row shows the magnitude of the correlation, and bottom row shows the phase, both as a function of lag. (a)-(d) Results for CPAI02 in light blue for 2011-12 and dark blue for 2012-13. (e)-(h) Results for Burger (light blue 2011-12; dark blue 2012-13) and CPAI01 (light green, 2011-12; dark green 2012-13). Numbers in parentheses are the critical values at the 95% significance level of the correlation coefficient.
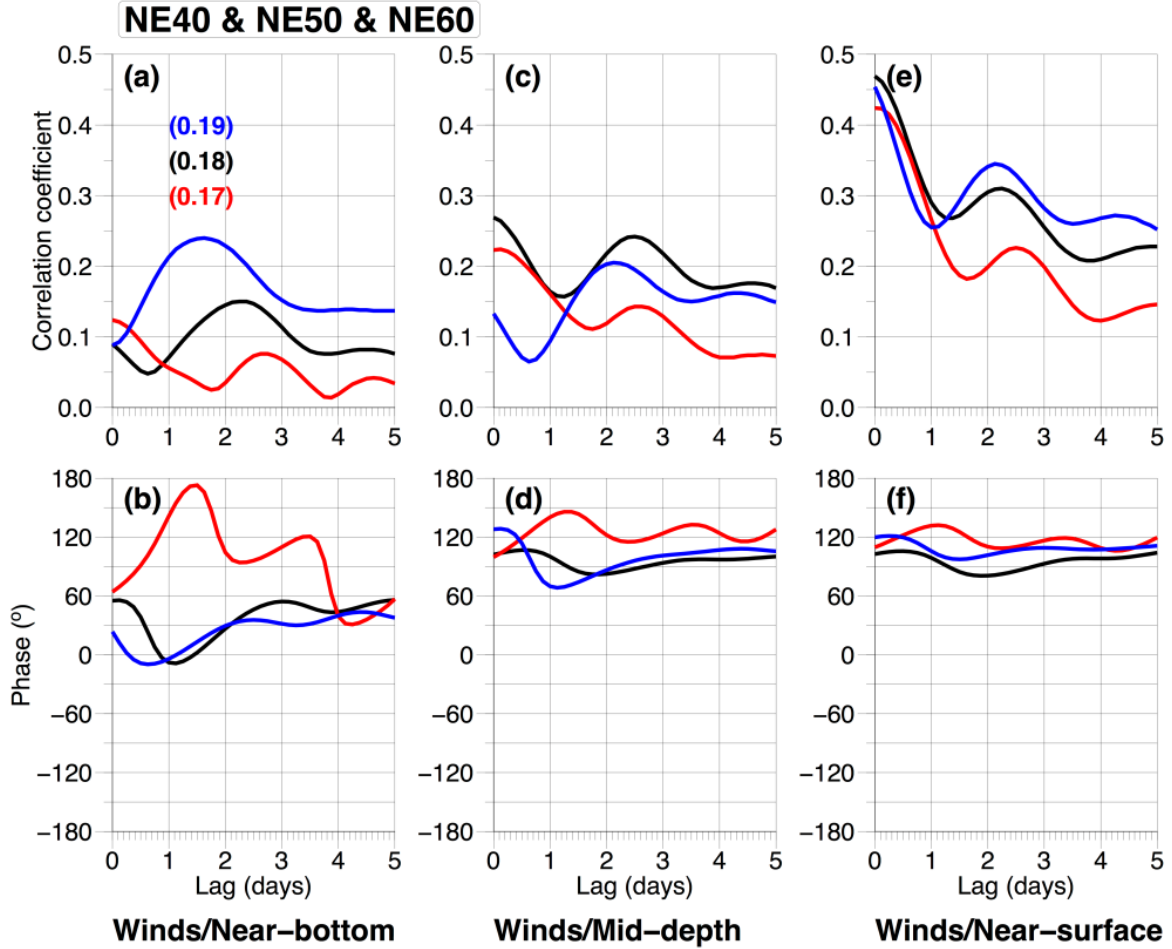
Figure 3.10. Lagged complex correlation results for 2012-13 for near-bottom, mid-depth, and near-surface currents at NE40 (red), NE50 (black), and NE60 (blue). Top row shows the magnitude of the correlation, and bottom row shows the phase, both as a function of lag. (a)-(b) For the near-bottom. (c)-(d) For the mid-depth. (e)-(f) For the near-surface. Numbers in parentheses are the critical values at the 95% significance level of the correlation coefficient.
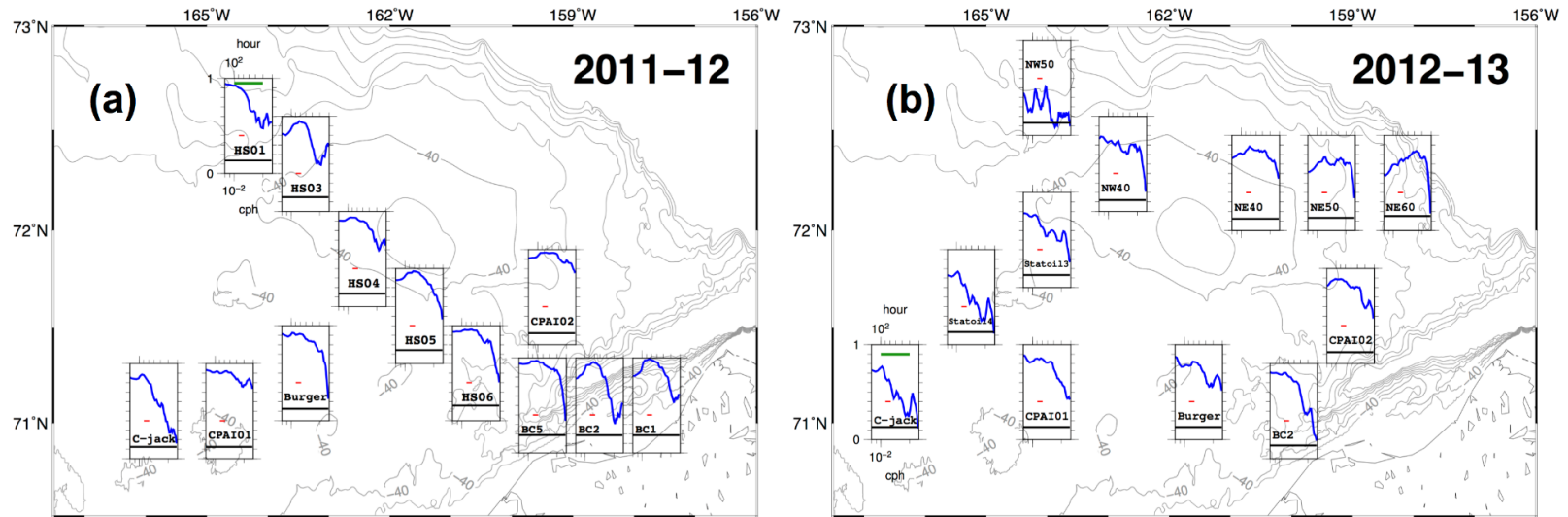
Figure 3.11. Maps of coherence spectra of the *u* components near the surface and bottom for (a) the 2011-12 period and (b) the 2012-13 period. The scales of the spectra are shown in HS01 in (a) and Crackerjack (C-jack) in (b), and the green line denotes the 50–100 hour band. Red lines in each spectra plot indicate the bandwidth over which a running mean averaging is applied to spectra.
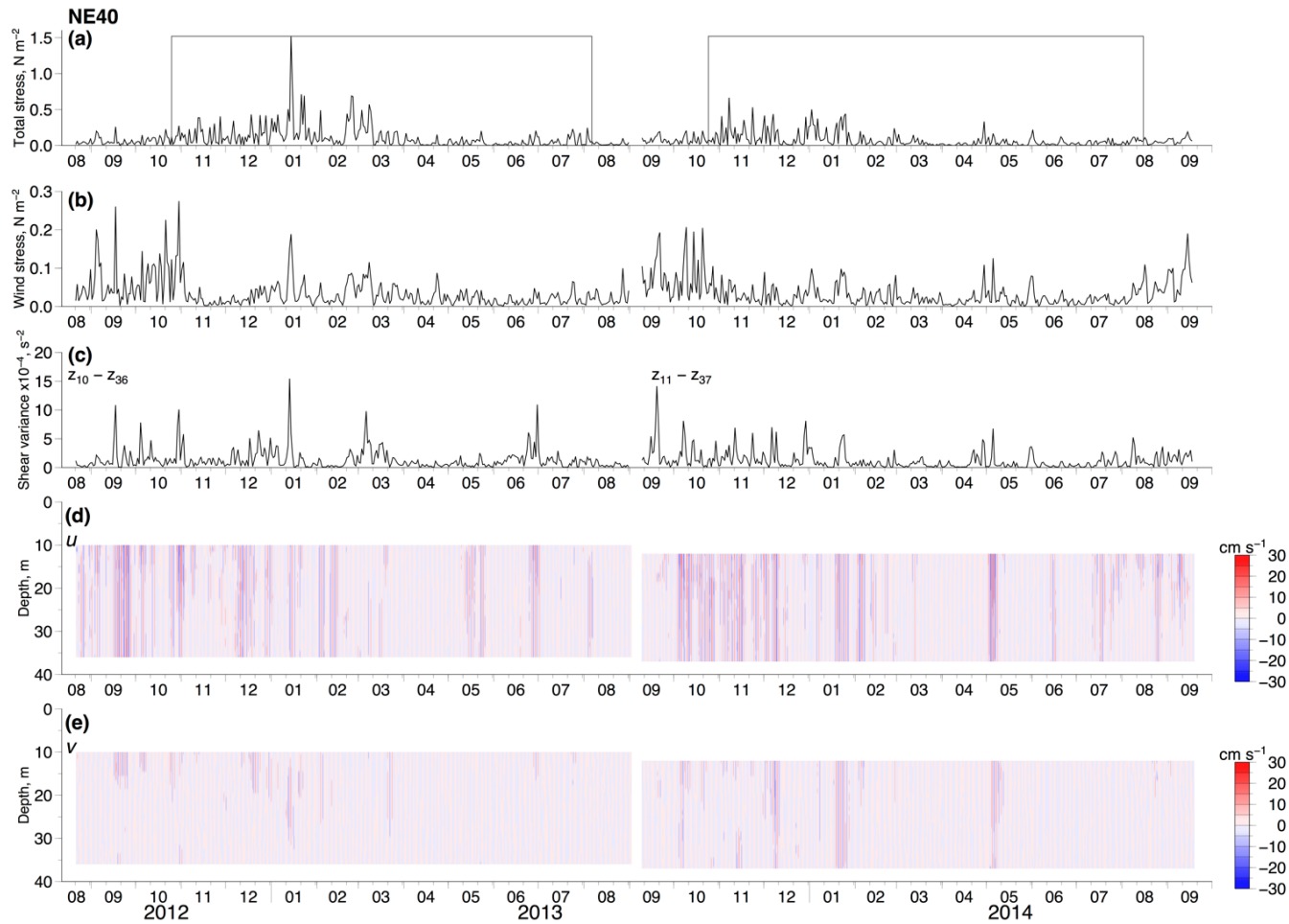
Figure 3.12. Time series at NE40 of (a) total stress, (b) wind stress, (c) velocity shear variances at near-surface and near-bottom depths, (d) profiles of *u* component filtered by a 50–100 hour passband, and (e) same as (d) but for *v* component. Rectangles shown in (a) denote times when ADCP-derived ice concentration is available.
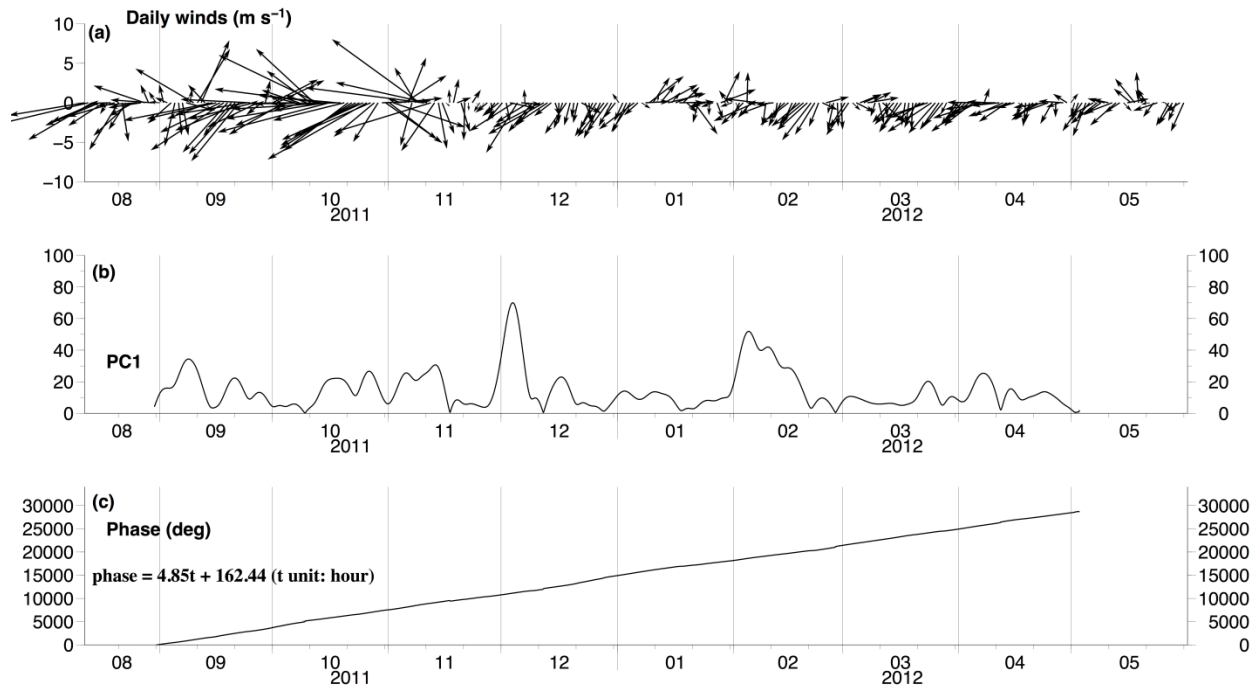
Figure 3.13. Time series of (a) daily winds, and (b)-(c) temporal amplitude (PC1) and phase of Mode 1 of the 2011-12 CEOF analysis.

137
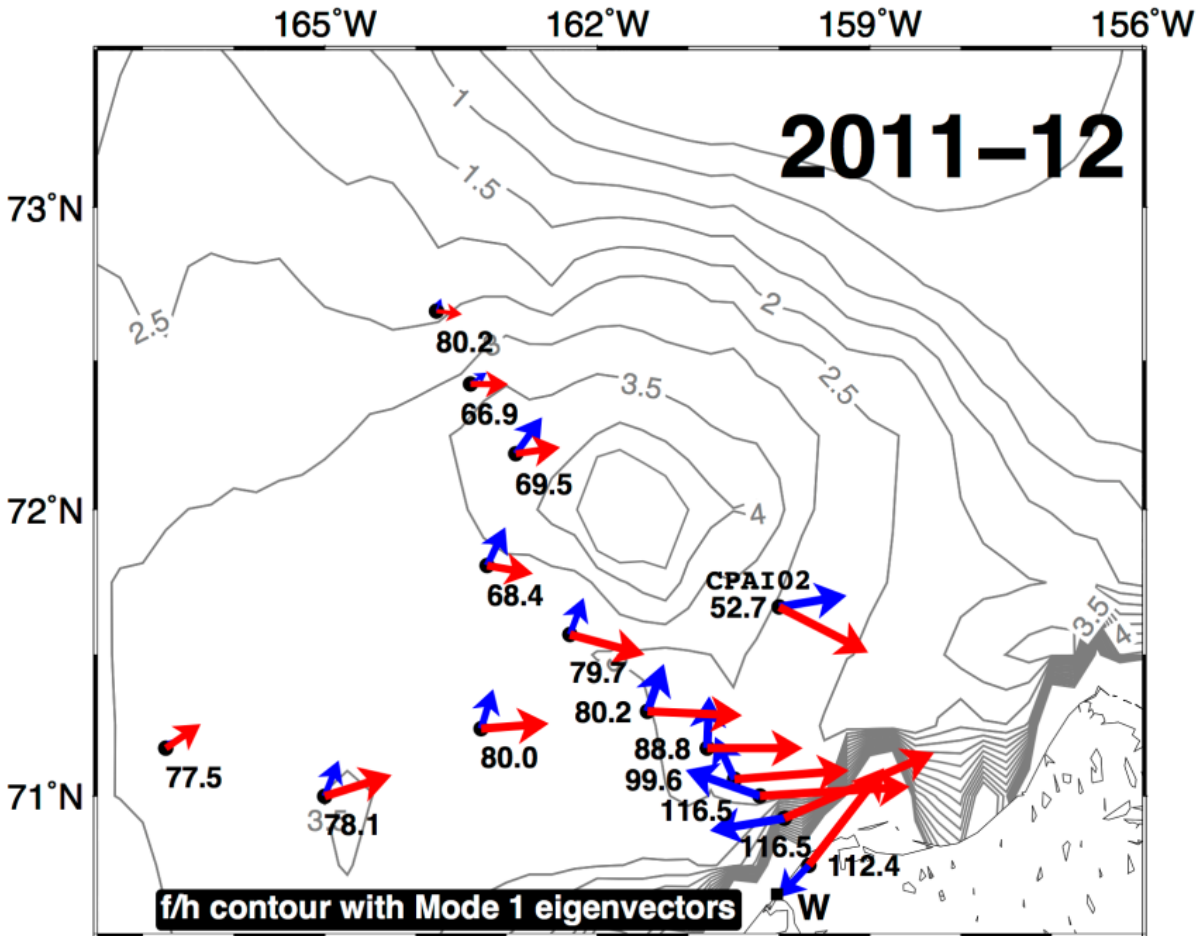
Figure 3.14. Eigenvectors of Mode 1 of the 2011-12 CEOF analysis. Currents at a reference time t_0 are in blue (real component of eigenvectors), whereas currents at $t_0 + \pi/2$ are in red (imaginary component of eigenvectors). Numbers are phases of the u components at each site. Gray lines denote contours of f/h (10^{-6} m^{-1}s^{-1}). Location of the CPAI02 mooring is labeled, and W on the land indicates Wainwright.
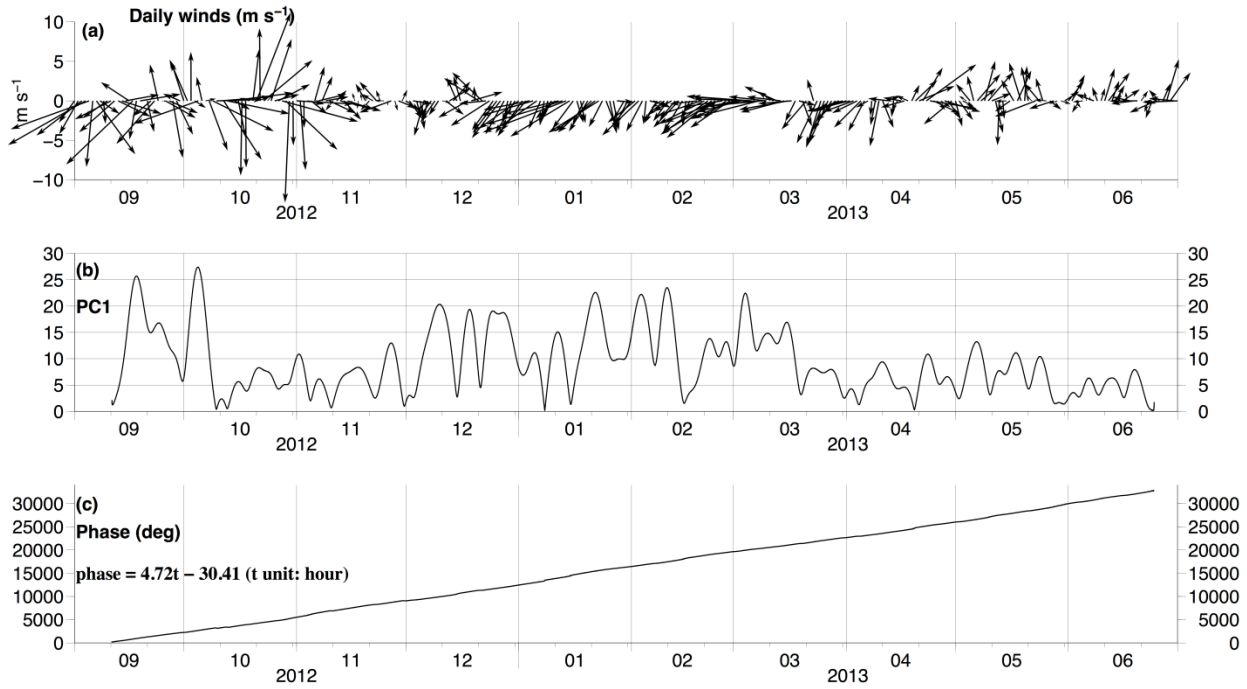
Figure 3.15. Time series of (a) daily winds, and (b)-(c) temporal amplitude (PC1) and phase of Mode 1 of the 2012-13 CEOF analysis.
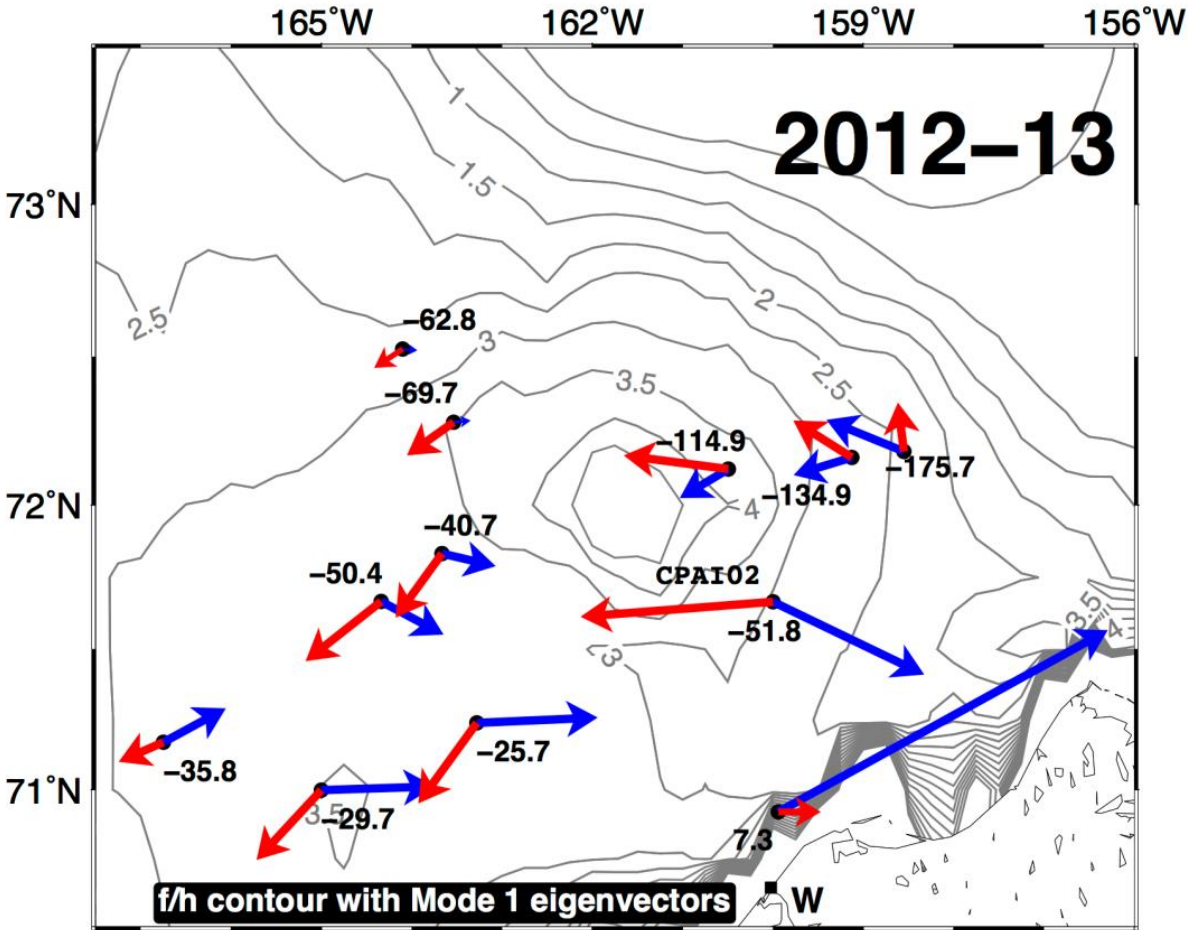
Figure 3.16. Eigenvectors of Mode 1 of the 2012-13 CEOF analysis. Currents at a reference time t_0 are in blue (real component of eigenvectors), whereas currents at $t_0+\pi/2$ are in red (imaginary component of eigenvectors). Numbers are phases of the u components at each site. Gray lines denote contours of f/h (10^{-6} m^{-1}s^{-1}). Location of the CPAI02 mooring is labeled, and W on the land indicates Wainwright.
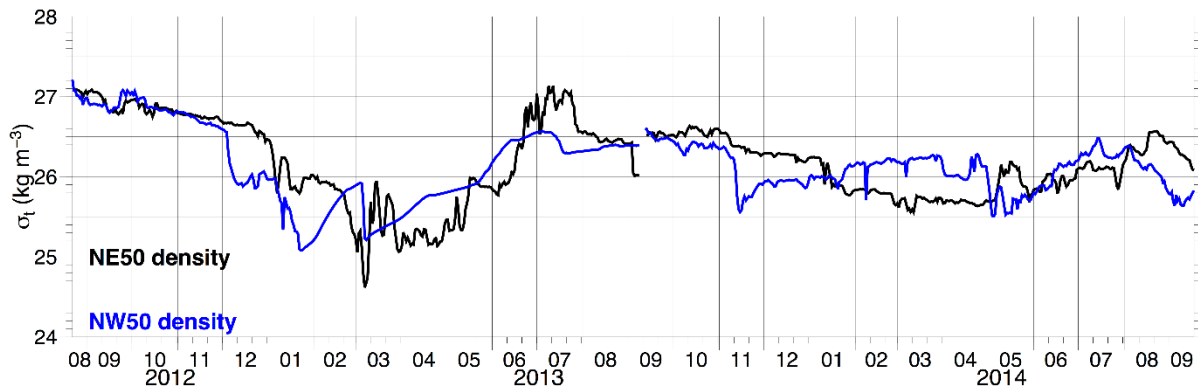
Figure 3.17. Time series of daily averaged density (σ_t) at 47 m at NE50 (black line) and at NW50 (blue line).
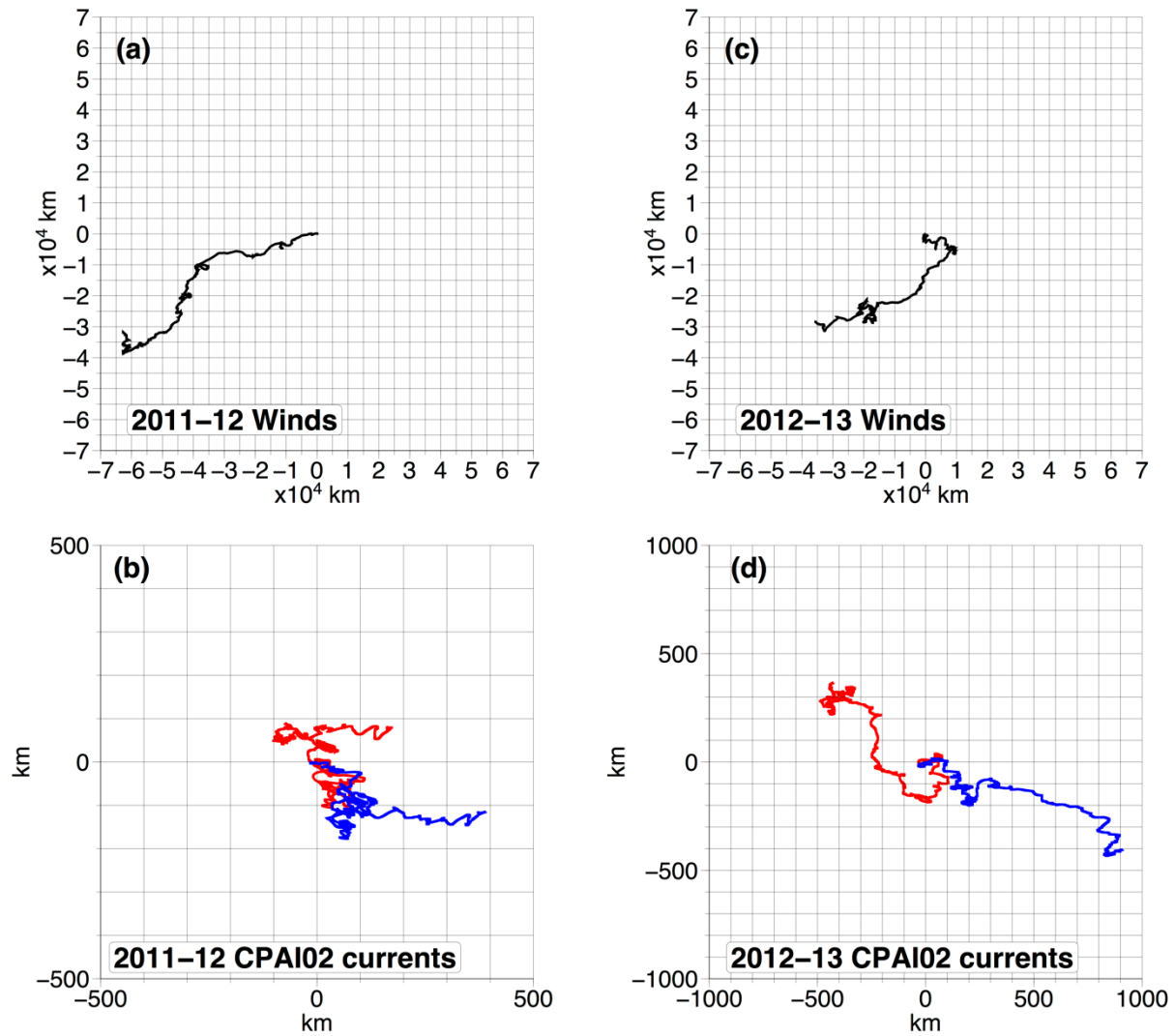
Figure 3.18. (a)-(b) Record-length progressive vector diagrams for winds and near-surface (red) and near-bottom (blue) currents at CPAI02 in the 2011-12 period. (c)-(d), same as (a)-(b) but for the 2012-13 period. Note that scales in (b) and (d) differ.

142

Table 3.1. Summary of mooring configurations.

Name	Group	Lat (ºW)	Lon (ºN)	Bottom Depth (m)	Instrument
2011–2012					
CPAI01	ASL	165.00	71.00	37	ADCP
CPAI02	ASL	160.00	71.67	45	ADCP
Burger	ASL	163.28	71.24	45	ADCP
Crackerjack	ASL	166.75	71.17	46	ADCP
HS01	ASL	163.77	72.66	58	ADCP
HS02	ASL	163.40	72.42	42	ADCP
HS03	ASL	162.90	72.19	40	ADCP
HS04	ASL	163.21	71.81	43	ADCP
HS05	ASL	162.30	71.57	45	ADCP
HS06	ASL	161.45	71.30	49	ADCP
BC1	BC	159.67	70.85	30	ADCP/TCP
BC2	BC	159.94	70.92	52	ADCP/TCP
BC3	BC	160.21	71.00	53	ADCP/TCP
BC4	BC	160.49	71.06	49	ADCP/TCP
BC5	BC	160.79	71.13	50	ADCP/TCP
BC6	BC	161.07	71.17	47	ADCP/TCP
2012–2013					
CPAI01	ASL	165.00	71.00	37	ADCP/TC
CPAI02	ASL	160.00	71.67	45	ADCP/TC
Burger	ASL	163.28	71.24	45	ADCP/TC
Crackerjack	ASL	166.75	71.17	46	ADCP/TC
Statoil3	ASL	163.67	71.83	44	ADCP/TC
Statoil4	ASL	164.34	71.67	38	ADCP/TC
NW40	COMIDA	163.53	72.28	41	ADCP/TCP
NW50	COMIDA	164.10	72.53	50	ADCP/TCP
NE40	COMIDA	160.50	72.12	40	ADCP/TCP
NE50	COMIDA	159.12	72.16	51	ADCP/TCP
NE60	COMIDA	158.55	72.18	56	ADCP/TCP
BC2	BC	159.94	70.92	52	ADCP/TCP
2013–2014					
Burger	ASL	163.28	71.24	45	ADCP/TC
Crackerjack	ASL	166.75	71.17	46	ADCP/TC
NW40	COMIDA	163.53	72.28	41	ADCP/TCP
NW50	COMIDA	164.10	72.53	50	ADCP/TCP
NE40	COMIDA	160.50	72.12	40	ADCP/TCP
NE50	COMIDA	159.12	72.16	51	ADCP/TCP
NE60	COMIDA	158.55	72.18	56	ADCP/TCP
BC2	BC	159.94	70.92	52	ADCP/TCP

Table 3.1 cont.

Name	[a]ADCP Range (m)	ADCP Period of record (mm/dd)	CTD Depth (m)	[b]Barotropic Fraction (%)
2011–2012				
CPAI01	S/15/27	07/28–08/12	N/A	N/A
CPAI02	S/23/41	08/03–08/24	N/A	N/A
Burger	S/17/35	08/02–08/12	N/A	N/A
Crackerjack	S/20/36	07/26–08/09	N/A	N/A
HS01	S/25/45	08/28–08/09	N/A	N/A
HS02	S/19/33	08/28–07/09	N/A	N/A
HS03	S/15/27	08/28–07/04	N/A	N/A
HS04	S/18/30	08/28–08/04	N/A	N/A
HS05	S/18/32	08/27–07/22	N/A	N/A
HS06	S/20/36	08/27–06/14	N/A	N/A
BC1	4–26	08/30–07/07	29	N/A
BC2	12–46	08/30–05/04	49	N/A
BC3	10–46	08/30–07/04	49	N/A
BC4	11–42	08/30–07/19	45	N/A
BC5	12–42	08/30–05/03	46	N/A
BC6	5–40	08/30–10/31(2011)	43	N/A
2012–2013				
CPAI01	S/17/27	08/13–07/31	31	N/A
CPAI02	S/22/40	09/11–10/07	43	N/A
Burger	S/16/34	08/12–07/31	N/A	N/A
Crackerjack	S/20/36	08/09–07/31	N/A	N/A
Statoil3	S/17/31	08/10–08/01	36	N/A
Statoil4	S/15/25	08/16–09/02	31	N/A
NW40	9–36	08/16–09/09	36	91.4
NW50	24–46	08/16–09/09	46	95.1
NE40	10–36	08/21–09/02	36	90.3
NE50	12–46	08/21–08/04	25/47	88.9
NE60	13–52	08/21–06/24	32/54	87.1
BC2	10–46	09/09–08/13	46	N/A
2013–2014				
Burger	S/17/35	08/01–08/05	N/A	N/A
Crackerjack	S/21/35	07/31–07/31	N/A	N/A
NW40	10–37	09/10–09/20	37	92.4
NW50	12–47	09/09–06/16	47	95.1
NE40	12–37	09/09–09/19	37	90.7
NE50	13–46	08/21–08/04	46	88.9
NE60	15–53	08/21–06/24	53	87.5
BC2	7–46	09/11–09/24	46	N/A

[a] Only three depths with velocity measurements in the ASL moorings. S denotes near-surface.
[b] Following Edwards and Seim (2008).

3.7 References

Aagaard, K., T. J. Weingartner, S. L. Danielson, R. A. Woodgate, G. C. Johnson, and T. E. Whitledge, 2006: Some controls on flow and salinity in Bering Strait. *Geophys. Res. Lett.*, **33**, doi:10.1029/2006GL026612.

Auad, G., and M. C. Hendershott, 1997: The low-frequency transport in the Santa Barbara Channel: description and forcing. *Cont. Shelf Res.*, **17**, 779–802, doi:http://dx.doi.org/10.1016/S0278-4343(96)00062-3.

Barnett, T. P., 1983: Interaction of the Monsoon and Pacific Trade Wind System at Interannual Time Scales Part I: The Equatorial Zone. *Mon. Weather Rev.*, **111**, 756–773, doi:10.1175/1520-0493(1983)111<0756:IOTMAP>2.0.CO;2.

Beckenbach, E., and L. Washburn, 2004: Low-frequency waves in the Santa Barbara Channel observed by high-frequency radar. *J. Geophys. Res. Ocean.*, **109**.

Beckers, J. M., and M. Rixen, 2003: EOF Calculations and Data Filling from Incomplete Oceanographic Datasets. *J. Atmos. Ocean. Technol.*, **20**, 1839–1856, doi:10.1175/1520-0426(2003)020<1839:ECADFF>2.0.CO;2.

Blanchard, A. L., R. H. Day, A. E. Gall, A.M. Aerts, J. Delarue, E. L. Dobbins, R. R. Hopcroft, J. M. Questel, T. J. Weingartner, and S. S. Wisdom, 2017: Ecosystem variability in the offshore Northeastern Chukchi Sea. *Prog. Oceanogr.*, doi:https://doi.org/10.1016/j.pocean.2017.08.008.

Chavanne, C. P., P. Flament, D. S. Luther, and K.-W. Gurgel, 2010: Observations of Vortex Rossby Waves Associated with a Mesoscale Cyclone*. *J. Phys. Oceanogr.*, **40**, 2333–2340, doi:10.1175/2010JPO4495.1.

Danielson, S. L., L. Eisner, C. Ladd, C. Mordy, L. Sousa, and T. J. Weingartner, 2017: A comparison between late summer 2012 and 2013 water masses, macronutrients, and phytoplankton standing crops in the northern Bering and Chukchi Seas. *Deep Sea Res. Part II Top. Stud. Oceanogr.*, **135**, 7–26, doi:https://doi.org/10.1016/j.dsr2.2016.05.024.

Dunton, K. H., J. M. Grebmeier, and J. H. Trefry, 2017: Hanna Shoal: An integrative study of a High Arctic marine ecosystem in the Chukchi Sea. *Deep Sea Res. Part II Top. Stud. Oceanogr.*, **144**, 1–5.

Dzwonkowski, B., K. Park, and L. Jiang, 2011: Subtidal across-shelf velocity structure and surface transport effectiveness on the Alabama shelf of the northeastern Gulf of Mexico. *J. Geophys. Res. Ocean.*, **116**, doi:10.1029/2011JC007188.

Edwards, C. R., and H. E. Seim, 2008: Complex EOF Analysis as a Method to Separate Barotropic and Baroclinic Velocity Structure in Shallow Water. *J. Atmos. Ocean. Technol.*, **25**, 808–821, doi:10.1175/2007JTECHO562.1.

Gong, D., and R. S. Pickart, 2015: Summertime circulation in the eastern Chukchi Sea. *Deep Sea Res. Part II Top. Stud. Oceanogr.*, **118**, 18–31, doi:10.1016/j.dsr2.2015.02.006.

Grantz, A., and S. Eittreim, 1979: *Geology and Physiography of the Continental Margin North of Alaska and Implications for the Origin of the Canada Basin U.S. Geological Survey, Open File Report 79-288*. 61 pp.

Grebmeier, J. M., B. A. Bluhm, L. W. Cooper, S. L. Danielson, K. R. Arrigo, A. L. Blanchard, J. T. Clarke, R. H. Day, K. E. Frey, R. R. Gradinger, M. Kędra, B. Konar, K. J. Kuletz, S. H. Lee, J. R. Lovvorn, B. L. Norcross, and S. R. Okkonen, 2015: Ecosystem characteristics and processes facilitating persistent macrobenthic biomass hotspots and associated benthivory in the Pacific Arctic. *Prog. Oceanogr.*, **136**, 92–114, doi:http://dx.doi.org/10.1016/j.pocean.2015.05.006.

Hirano, D., Y. Fukamachi, E. Watanabe, K. I. Ohshima, K. Iwamoto, A. R. Mahoney, H. Eichen, D. Simizu, and T. Tamura, 2016: A wind-driven, hybrid latent and sensible heat coastal polynya off Barrow, Alaska. *J. Geophys. Res. Ocean.*, **121**, 980–997, doi:10.1002/2015JC011318.

Itoh, M., S. Nishino, Y. Kawaguchi, and T. Kikuchi, 2013: Barrow Canyon volume, heat, and freshwater fluxes revealed by long-term mooring observations between 2000 and 2008. *J. Geophys. Res. Ocean.*, **118**, 4363–4379, doi:10.1002/jgrc.20290.

Johnson, W. R., 1989: Current response to wind in the Chukchi Sea: A regional coastal upwelling event. *J. Geophys. Res. Ocean.*, **94**, 2057–2064, doi:10.1029/JC094iC02p02057.

Kaihatu, J. M., R. A. Handler, G. O. Marmorino, and L. K. Shay, 1998: Empirical Orthogonal Function Analysis of Ocean Surface Currents Using Complex and Real-Vector Methods. *J. Atmos. Ocean. Technol.*, **15**, 927–941.

Kawaguchi, Y., S. Nishino, and J. Inoue, 2015: Fixed-Point Observation of Mixed Layer Evolution in the Seasonally Ice-Free Chukchi Sea: Turbulent Mixing due to Gale Winds and Internal Gravity Waves. *J. Phys. Oceanogr.*, **45**, 836–853.

Light, B., T. C. Grenfell, and D. K. Perovich, 2008: Transmission and absorption of solar radiation by Arctic sea ice during the melt season. *J. Geophys. Res. Ocean.*, **113**, n/a-n/a, doi:10.1029/2006JC003977.

Lu, K., T. Weingartner, S. Danielson, P. Winsor, E. Dobbins, K. Martini, and H. Statscewich, 2015: Lateral mixing across ice meltwater fronts of the Chukchi Sea shelf. *Geophys. Res. Lett.*, doi:10.1002/2015GL064967.

Martin, S., and R. Drucker, 1997: The effect of possible Taylor columns on the summer ice retreat in the Chukchi Sea. *J. Geophys. Res.*, **102**, 10410–10473.

Martini, K. I., H. L. Simmons, C. A. Stoudt, and J. K. Hutchings, 2014: Near-Inertial Internal Waves and Sea Ice in the Beaufort Sea*. *J. Phys. Oceanogr.*, **44**, 2212–2234, doi:10.1175/JPO-D-13-0160.1.

Mesinger, F., G. DiMego, E. Kalnay, K. Mitchell, P. C. Shafran, W. Ebisuzaki, D. Jović, J. Woollen, E. Rogers, E. H. Berbery, M. B. Ek, Y. Fan, R. Grumbine, W. Higgins, H. Li, Y. Lin, G. Manikin, D. Parrish, and W. Shi, 2006: North American Regional Reanalysis. *Bull. Am. Meteorol. Soc.*, **87**, 343–360, doi:10.1175/BAMS-87-3-343.

Miller, A. J., P. F. J. Lermusiaux, and P.-M. Poulain, 1996: A Topographic–Rossby Mode Resonance over the Iceland–Faeroe Ridge. *J. Phys. Oceanogr.*, **26**, 2735–2747, doi:10.1175/1520-0485(1996)026<2735:ATMROT>2.0.CO;2.

Moore, S. E., and H. P. Huntington, 2008: Arctic Marine Mammals and Climate Change: Impacts and Resilience. *Ecol. Appl.*, **18**, S157–S165, doi:10.1890/06-0571.1.

——, P. J. Stabeno, J. M. Grebmeier, and S. R. Okkonen, The Arctic Marine Pulses Model: linking annual oceanographic processes to contiguous ecological domains in the Pacific Arctic. *Deep Sea Res. Part II Top. Stud. Oceanogr.*, **in press**, doi:http://dx.doi.org/10.1016/j.dsr2.2016.10.011.

Mudge, T. D., A. Slonimer, J. Barrette, N. Milutinovic, D. Sadowy, and K. Borg, 2015: Analysis of Ice and Metocean Measurements, Chukchi Sea 2013-2014, for Shell. *Proj. Rep. Shell Int. Exporation Prod. Inc., Houston, Texas by ASL Environ. Sci. Inc., Victoria, B.C. Canada. xi + 108p,*.

Paduan, J. D., and L. K. Rosenfeld, 1996: Remotely sensed surface currents in Monterey Bay from shore-based HF radar (Coastal Ocean Dynamics Application Radar). *J. Geophys. Res.*, **101**, 20669, doi:10.1029/96JC01663.

Pedlosky, J., 1987: *Geophysical Fluid Dynamics*. Springer-Verlag, New York, 710 pp.

Pickart, R. S., L. J. Pratt, D. J. Torres, T. E. Whitledge, A. Y. Proshutinsky, K. Aagaard, T. A. Agnew, G.W.K Moore, and H. J. Dail, 2010: Evolution and dynamics of the flow through Herald Canyon in the western Chukchi Sea. *Deep Sea Res. Part II Top. Stud. Oceanogr.*, **57**, 5–26, doi:10.1016/j.dsr2.2009.08.002.

Pickart, R. S., G. W. K. Moore, C. Mao, F. Bahr, C. Nobre, and T. J. Weingartner, 2016: Circulation of winter water on the Chukchi shelf in early Summer. *Deep Sea Res. Part II Top. Stud. Oceanogr.*, **130**, 56–75, doi:http://dx.doi.org/10.1016/j.dsr2.2016.05.001.

Pisareva, M. N., R. S. Pickart, M. A. Spall, C. Nobre, D. J. Torres, G. W. K. Moore, and T. E. Whitledge, 2015: Flow of pacific water in the western Chukchi Sea: Results from the 2009 RUSALCA expedition. *Deep Sea Res. Part I Oceanogr. Res. Pap.*, **105**, 53–73, doi:https://doi.org/10.1016/j.dsr.2015.08.011.

Roach, A. T., K. Aagaard, C. H. Pease, S. A. Salo, T. Weingartner, V. Pavlov, and M. Kulakov, 1995: Direct measurements of transport and water properties through the Bering Strait. *J. Geophys. Res. Ocean.*, **100**, 18443–18457, doi:10.1029/95JC01673.

Shimada, K., T. Kamoshida, M. Itoh, S. Nishino, E. Carmack, F. McLaughlin, S. Zimmermann, and A. Proshutinsky, 2006: Pacific Ocean inflow: Influence on catastrophic reduction of sea ice cover in the Arctic Ocean. *Geophys. Res. Lett.*, **33**, L08605, doi:10.1029/2005GL025624.

Spall, M. A., 2007: Circulation and water mass transformation in a model of the Chukchi Sea. *J. Geophys. Res.*, **112**, C05025, doi:10.1029/2005JC003364.

Stigebrandt, A., 1984: The North Pacific: A Global-Scale Estuary. *J. Phys. Oceanogr.*, **14**, 464–470, doi:10.1175/1520-0485(1984)014<0464:TNPAGS>2.0.CO;2.

Stoudt, C. A., 2015: Sea ice near-inertial response to atmospheric storms. *(Order No. 1588390). Available from Diss. Theses @ Univ. Alaska Fairbanks. (1682267616). Retrieved from https//search.proquest.com/docview/1682267616?accountid=14470*, 76.

Visbeck, M., and J. Fischer, 1994: Sea Surface Conditions Remotely Sensed by Upward-Looking ADCPs. *J. Atmos. Ocean. Technol.*, **12**, 141–149, doi:10.1175/1520-0426(1995)012<0141:SSCRSB>2.0.CO;2.

Wang, D.-P., and C. N. K. Mooers, 1976: Coastal-Trapped Waves in a Continuously Stratified Ocean. *J. Phys. Oceanogr.*, **6**, 853–863, doi:10.1175/1520-0485(1976)006<0853:CTWIAC>2.0.CO;2.

Weingartner, T. J., D. J. Cavalieri, K. Aagaard, and Y. Sasaki, 1998: Circulation, dense water formation, and outflow on the northeast Chukchi Shelf. *J. Geophys. Res. Ocean.*, **103**, 7647–7661, doi:10.1029/98JC00374.

——, K. Aagaard, R. Woodgate, S. Danielson, Y. Sasaki, and D. Cavalieri, 2005: Circulation on the north central Chukchi Sea shelf. *Deep Sea Res. Part II Top. Stud. Oceanogr.*, **52**, 3150–3174, doi:10.1016/j.dsr2.2005.10.015.

——, E. Dobbins, S. Danielson, P. Winsor, R. Potter, and H. Statscewich, 2013a: Hydrographic variability over the northeastern Chukchi Sea shelf in summer-fall 2008–2010. *Cont. Shelf Res.*, **67**, 5–22, doi:http://dx.doi.org/10.1016/j.csr.2013.03.012.

——, P. Winsor, R. A. Potter, H. Statscewich, and E. L. Dobbins, 2013b: OCS Study BOEM 2012-079 Application of High Frequency Radar to Potential Hydrocarbon Development Areas in the Northeast Chukchi Sea. *Final Rep., U.S. Dept. Inter. Alaska Outer Cont. Shelf Reg. Contract M09AC15207, OCS Study BOEM 2012- 079, 162 pp. [Available online www.boem.gov/ESPIS/5/5266.pdf]*,.

Weingartner, T. J., Y.-C. Fang, and P. Winsor, 2016: Physical oceanography and circulation. *Chukchi Sea Offshore Monit. Drill. Area Hanna Shoal Ecosyst. Study Final Rep.*, K. H. Dunton (Ed.).

Weingartner, T. J., Y.-C. Fang, P. Winsor, E. Dobbins, R. Potter, H. Statscewich, T. Mudge, B. Irving, L. Sousa, and K. Borg, 2017a: The summer hydrographic structure of the Hanna Shoal region on the northeastern Chukchi Sea shelf: 2011–2013. *Deep Sea Res. Part II Top. Stud. Oceanogr.*, **144**, 6–20, doi:https://doi.org/10.1016/j.dsr2.2017.08.006.

——, R. A. Potter, C. A. Stoudt, E. L. Dobbins, H. Statscewich, P. R. Winsor, T. D. Mudge, and K. Borg, 2017b: Transport and thermohaline variability in Barrow Canyon on the Northeastern Chukchi Sea Shelf. *J. Geophys. Res. Ocean.*, **122**, doi:10.1002/2016JC012636.

Winsor, P., and D. C. Chapman, 2004: Pathways of Pacific water across the Chukchi Sea: A numerical model study. *J. Geophys. Res. Ocean.*, **109**, C03002, doi:10.1029/2003JC001962.

Wood, K. R., N. A. Bond, S. L. Danielson, J. E. Overland, S. A. Salo, P. J. Stabeno, and J. Whitefield, 2015: A decade of environmental change in the Pacific Arctic region. *Prog. Oceanogr.*, **136**, 12–31, doi:http://dx.doi.org/10.1016/j.pocean.2015.05.005.

Woodgate, R. A., 2005: Monthly temperature, salinity, and transport variability of the Bering Strait through flow. *Geophys. Res. Lett.*, **32**, L04601, doi:10.1029/2004GL021880.

——, K. Aagaard, and T. J. Weingartner, 2005: A year in the physical oceanography of the Chukchi Sea: Moored measurements from autumn 1990–1991. *Deep Sea Res. Part II Top. Stud. Oceanogr.*, **52**, 3116–3149, doi:10.1016/j.dsr2.2005.10.016.

——, T. J. Weingartner, and R. Lindsay, 2010: The 2007 Bering Strait oceanic heat flux and anomalous Arctic sea-ice retreat. *Geophys. Res. Lett.*, **37**, doi:10.1029/2009GL041621.

Woodgate, R. A., T. J. Weingartner, and R. Lindsay, 2012: Observed increases in Bering Strait oceanic fluxes from the Pacific to the Arctic from 2001 to 2011 and their impacts on the Arctic Ocean water column. *Geophys. Res. Lett.*, **39**, doi:10.1029/2012GL054092.

Yang, J., 2006: The Seasonal Variability of the Arctic Ocean Ekman Transport and Its Role in the Mixed Layer Heat and Salt Fluxes. *J. Clim.*, **19**, 5366–5387, doi:10.1175/JCLI3892.1.

Yankovsky, A. E., and D. C. Chapman, 1995: Generation of mesoscale flows over the shelf and slope by shelf wave scattering in the presence of a stable, sheared mean current. *J. Geophys. Res. Ocean.*, **100**, 6725–6742, doi:10.1029/94JC03339.

General Conclusion

This dissertation has examined both the circulation structure of the surface currents (Chapter 2) derived by HFR, and the subsurface currents (Chapter 3) measured by moored current meters in the northeastern Chukchi Sea. In order to analyze these data, I fine-tuned the OI technique to this unique arctic setting to produce a high quality HFR data set (Chapter 1). The main conclusions from this study are as follows.

1. The OI method is a robust alternative processing approach compared to the conventional least squares fit method. This method effectively reduces the influence of random noise and is able to fill data gaps. I offered several cautionary considerations for applying this method to processing HFR-derived surface current data. The OI method is a biased estimator and is fundamentally controlled by three factors. The first factor is the number of available measured radial velocities (AR). The second factor is determined by the ratio of overlapping radial velocities (ROR), and the third factor depends on the positive definiteness of the correlation matrix as determined by the condition number (CN). These three factors varied with one other, and I determined that the most important factor is ROR. The ROR significantly governs the resultant quality of OI-estimated two-dimensional currents. A high ROR means that most radial velocities are from one HFR site rather than being distributed between multiple sites, which will result in erroneous surface currents. From my investigation, an ROR = 5 (meaning one HFR site contributes 5 times more velocity measurements than the secondary contributor) appears to be a minimum threshold for resulting in a quality estimate (<~30% error, assuming no random noise) of the surface currents. The ideal distribution of ROR is solely a function of radar geometry and can be computed without data. In HFR applications, this can facilitate diagnosing resultant data quality before the HFR network is deployed. This approach could save resources and help avoid site locations that would cause biases. This finding should benefit those deploying HFR networks at suboptimal sites around the world.

2. I used SOM to extract significant surface circulation patterns during open water seasons in response to variable winds using HFR-derived surface current data from 2010–2014. Besides the commonly seen northeastward-flowing pattern driven by the

background Pacific-Arctic pressure gradient, I determined three other wind-driven patterns. Two are associated with northeasterly winds $>\sim6$ m s^{-1}. As northeasterly winds strengthen to ~6 m s^{-1}, the surface current field starts to shift into a wind-driven regime, and a transitional state, termed as the divergent mode, evolves containing two counterrotating circulation regions. Their development results from dynamically different regimes due to the local hydrography during summer and fall. The water column is strongly stratified north of 71.5°N and near the eastern side of Hanna Shoal, where a thin but strong pycnocline separates bottom winter waters and near-surface meltwaters, and surface currents in this region have a very Ekman-like response. Additionally, surface currents north of 71.5°N and in shallow waters (<40 m depth) respond to strengthening northeasterly winds faster than offshore regions and near Barrow Canyon where the surface current field is more strongly influenced by the Pacific-Arctic pressure gradient. As northeasterly wind speeds increase, the flow field adjusts to the wind-induced coastal setup and shelf-wide southwestward currents result. A similar evolution occurs under strong northwesterly winds with a faster response north of 71.5°N than the shelf area to the south. The winds will eventually force a shelf-wide southward-flowing current field, although this northwesterly wind pattern is infrequent compared to that with winds from the northeast.

3. I analyzed 23 moorings which collected velocity and hydrographic observations from 2011–2014 of the Hanna Shoal region. The most important finding is that I determined there is a zonal gradient in the thermohaline and velocity fields on the shelf north of Hanna Shoal. On the western side, the water column is weakly sheared with northeastward currents and includes annual mixing and cooling that leads to unstratified waters and the temperature collapsing to the freezing point throughout the water column. On the eastern side of the Shoal, the flow field is strongly sheared and stratified year-round, with upper layer currents flowing to the northwest and bottom waters flowing southward. The hydrography indicates large fluctuations in temperature and salinity consistent with the strong, thin pycnocline migrating vertically. In winter, a zonally-oriented baroclinic pressure gradient in the lower layer of the water column begins to form. This pressure gradient varies in magnitude and

154

sign and will force cross-isobath flow of bottom waters north of Hanna Shoal. My findings suggest there is zonal flow convergence along the north side of Hanna Shoal which could result in shelf-basin exchange of water masses.

4. I documented the formation and propagation of a barotropic topographic wave mode along the eastern side of Hanna Shoal. The wave has a period of ~3 days and is generated at times of strong wind and/or ice movement. The waves propagate clockwise around the Shoal but are not evident near Barrow Canyon or along the northwestern side of the Shoal, where wave blocking and scattering are hypothesized to obliterate the signal.

As a whole, I have thoroughly investigated the physical oceanography of the northeastern Chukchi Sea in terms of surface and subsurface currents, hydrography, and oceanic response to varied atmospheric forcing. These results provide further insights on the local circulation that should benefit local communities, resource managers, industry, and emergency responders. My findings suggest that several additional topics need investigation, which are described in the following paragraphs.

Current meter data indicates the flow along the northwestern side of Hanna Shoal behaves very differently from other places on the northeastern Chukchi shelf. The flow speed is several orders larger than those at the eastern side of Hanna Shoal and is relatively steady in direction to the east-northeast. Models indicate that this eastward flow may include contributions from the Central Channel as well as outflow from Herald Valley farther west. A future mooring array deployed longitudinally east of the Russian-U.S. Conventional Line is recommended to resolve the upstream nature of the flow northwest of Hanna Shoal.

Summer observations and thermohaline records have suggested the development of a counterclockwise baroclinic pressure gradient resultant from an across-shoal density gradient. Unfortunately, there are no available measurements to evaluate spatio-temporal variations in this pressure gradient. Dedicated field experiments using bottom pressure sensors (e.g., Brown et al. 1985) and a vertically-distributed array of temperature/conductivity recorders would be required to resolve how this pressure gradient responds to the background Pacific-Arctic pressure gradient and regional winds. Moreover, convergence along the northern side of Hanna Shoal inferred from present observations should be elucidated by a future mooring array to monitor the shelf-

basin exchange. These efforts are essential to fill the data gap where the flow from the Central Channel begins to interact with both Hanna Shoal and the eastward outflow from Herald Canyon.

My dissertation did not account for high-frequency motions such tides and internal waves. The data sets used in this dissertation are long-term, and some have very high temporal resolutions (≤1 hour), so these data are amenable for studying these high-frequency phenomena. Arctic tides are found to be important for vertical mixing, and the presence of sea ice appears to enhance their role in mixing (e.g., Lenn et al. 2011; Janout and Lenn 2014; Pnyushkov and Polyakov 2011). In the northeastern Chukchi Sea, the analytical challenge is in separating the semidiurnal tides from near-inertial motions. My preliminary investigations (not shown) indicate that there are wind-driven, near-inertial internal wave signals in the semidiurnal band, but these weaken as the sea ice cover is established. Kawaguchi et al. (2015, 2016) have conducted research along these lines, but their observations were limited in time and restricted to a fixed location. Understanding the temporal and geographical variations of internal waves on the Chukchi shelf, their interactions with a variable sea ice cover, and their role in mixing remain to be determined.

References

Aagaard, K., and A. T. Roach, 1990: Arctic ocean-shelf exchange: Measurements in Barrow Canyon. *J. Geophys. Res. Ocean.*, **95**, 18163–18175, doi:10.1029/JC095iC10p18163.

Aagaard, K., L. K. Coachman, and E. Carmack, 1981: On the halocline of the Arctic Ocean. *Deep Sea Res. Part A. Oceanogr. Res. Pap.*, **28**, 529–545, doi:http://dx.doi.org/10.1016/0198-0149(81)90115-1.

Barrick, D. E., 1978: HF radio oceanography — A review. *Boundary-Layer Meteorol.*, **13**, 23–43, doi:10.1007/BF00913860.

Barrick, D. E., J. M. Headrick, R. W. Bogle, and D. D. Crombie, 1974: Sea backscatter at HF: Interpretation and utilization of the echo. *Proc. IEEE*, **62**, 673–680, doi:10.1109/PROC.1974.9507.

Brown, W. S., N. R. Pettigrew, and J. D. Irish, 1985: The Nantucket Shoals Flux Experiment (NSFE79). Part II: The Structure and Variability of Across-Shelf Pressure Gradients. *J. Phys. Oceanogr.*, **15**, 749–771, doi:10.1175/1520-0485(1985)015<0749:TNSFEP>2.0.CO;2.

Coachman, L. K., K. Aagaard, and R. B. Tripp, 1975: *Bering Strait: The Regional Physical Oceanography*. University of Washington Press, Seattle, 172 pp.

Crombie, D. D., 1955: Doppler spectrum of sea echo at 13.56 Mc./s. *Nature*, **175**, 6810682.

Davis, R. E., 1985: Drifter observations of coastal surface currents during CODE: The method and descriptive view. *J. Geophys. Res. Ocean.*, **90**, 4741–4755, doi:10.1029/JC090iC03p04741.

Day, R. H., T. J. Weingartner, R. R. Hopcroft, L. A.M. Aerts, A. L. Blanchard, A. E. Gall, B. J. Gallaway, D. E. Hannay, B. A. Holladay, J. T. Mathis, B. L. Norcross, J. M. Questel, and S. S. Wisdom, 2013: The offshore northeastern Chukchi Sea, Alaska: A complex high-latitude ecosystem. *Cont. Shelf Res.*, **67**, 147–165, doi:https://doi.org/10.1016/j.csr.2013.02.002.

Dunton, K. H., J. M. Grebmeier, and J. H. Trefry, 2014: The benthic ecosystem of the northeastern Chukchi Sea: An overview of its unique biogeochemical and biological characteristics. *Deep Sea Res. Part II Top. Stud. Oceanogr.*, **102**, 1–8, doi:https://doi.org/10.1016/j.dsr2.2014.01.001.

Emery, W. J., C. Fowler, and C. A. Clayson, 1992: Satellite-Image-derived Gulf Stream Currents Compared with Numerical Model Results. *J. Atmos. Ocean. Technol.*, **9**, 286–304, doi:10.1175/1520-0426(1992)009<0286:SIDGSC>2.0.CO;2.

Frey, K. E., G. W. K. Moore, L. W. Cooper, and J. M. Grebmeier, 2015: Divergent patterns of recent sea ice cover across the Bering, Chukchi, and Beaufort seas of the Pacific Arctic Region. *Prog. Oceanogr.*, **136**, 32–49, doi:http://dx.doi.org/10.1016/j.pocean.2015.05.009.

Grantz, A., and S. Eittreim, 1979: *Geology and Physiography of the Continental Margin North of Alaska and Implications for the Origin of the Canada Basin U.S. Geological Survey, Open File Report 79-288*. 61 pp.

Grebmeier, J. M., 2012: Shifting Patterns of Life in the Pacific Arctic and Sub-Arctic Seas. *Ann. Rev. Mar. Sci.*, **4**, 63–78, doi:10.1146/annurev-marine-120710-100926.

——, C. P. Mcroy, and H. M. Feder, 1988: Pelagic-benthic coupling on the shelf of the northern Bering and Chukchi Seas . I . Food supply source and benthic biomass. *Mar. Ecol. Prog. Ser.*, **48**, 57–67.

——, L. W. Cooper, H. M. Feder, and B. I. Sirenko, 2006: Ecosystem dynamics of the Pacific-influenced Northern Bering and Chukchi Seas in the Amerasian Arctic. *Prog. Ocean.*, **71**, 331–361, doi:10.1016/j.pocean.2006.10.001.

——, B. A. Bluhm, L. W. Cooper, S. L. Danielson, K. R. Arrigo, A. L. Blanchard, J. T. Clarke, R. H. Day, K. E. Frey, R. R. Gradinger, M. Kędra, B. Konar, K. J. Kuletz, S. H. Lee, J. R. Lovvorn, B. L. Norcross, and S. R. Okkonen, 2015: Ecosystem characteristics and processes facilitating persistent macrobenthic biomass hotspots and associated benthivory in the Pacific Arctic. *Prog. Oceanogr.*, **136**, 92–114, doi:http://dx.doi.org/10.1016/j.pocean.2015.05.006.

Harlan, J., E. Terrill, L. Hazard, C. Keen, D. Barrick, C. Whelan, S. Howden, and J. Kohut, 2010: The integrated ocean observing system high-frequency radar network: status and local, regional, and national applications. *Mar. Technol. Soc. J.*, **44**, 122–132.

Hayes, D., 2001: *Historical Atlas of the North Pacific Ocean: Maps of Discovery & Scientific Exploration, 1500-2000*. Sasquatch Books, Seattle, WA, 224 pp.

Janout, M. A., and Y.-D. Lenn, 2014: Semidiurnal Tides on the Laptev Sea Shelf with Implications for Shear and Vertical Mixing. *J. Phys. Oceanogr.*, **44**, 202–219.

Kawaguchi, Y., S. Nishino, and J. Inoue, 2015: Fixed-Point Observation of Mixed Layer Evolution in the Seasonally Ice-Free Chukchi Sea: Turbulent Mixing due to Gale Winds and Internal Gravity Waves. *J. Phys. Oceanogr.*, **45**, 836–853.

——, ——, ——, K. Maeno, H. Takeda, and K. Oshima, 2016: Enhanced Diapycnal Mixing due to Near-Inertial Internal Waves Propagating through an Anticyclonic Eddy in the Ice-Free Chukchi Plateau. *J. Phys. Oceanogr.*, **46**, 2457–2481, doi:10.1175/JPO-D-15-0150.1.

Kim, S. Y., E. Terrill, and B. Cornuelle, 2007: Objectively mapping HF radar-derived surface current data using measured and idealized data covariance matrices. *J. Geophys. Res. Ocean.*, **112**, C06021, doi:10.1029/2006JC003756.

——, E. J. Terrill, and B. D. Cornuelle, 2008: Mapping surface currents from HF radar radial velocity measurements using optimal interpolation. *J. Geophys. Res. Ocean.*, **113**, C10023, doi:10.1029/2007JC004244.

Kohonen, T., 2001: Self-Organizing Maps. *Springer Ser. Inf. Sci., 3rd ed., Springer, New York*, **30**, 501 pp.

Lenn, Y.-D., T. P. Rippeth, C. P. Old, S. Bacon, I. Polyakov, V. Ivanov, and J. Hölemann, 2011: Intermittent Intense Turbulent Mixing under Ice in the Laptev Sea Continental Shelf. *J. Phys. Oceanogr.*, **41**, 531–547, doi:10.1175/2010JPO4425.1.

Martin, S., and R. Drucker, 1997: The effect of possible Taylor columns on the summer ice retreat in the Chukchi Sea. *J. Geophys. Res.*, **102**, 10410–10473.

Maury, M. F., 1855: *Physical Geography of The Sea*. Harper & Brothers, New York, 288 pp.

Moore, S. E., and H. P. Huntington, 2008: Arctic Marine Mammals and Climate Change: Impacts and Resilience. *Ecol. Appl.*, **18**, S157–S165, doi:10.1890/06-0571.1.

Mountain, D. G., L. K. Coachman, and K. Aagaard, 1976: On the Flow Through Barrow Canyon. *J. Phys. Oceanogr.*, **6**, 461–470, doi:10.1175/1520-0485(1976)006<0461:OTFTBC>2.0.CO;2.

Paquette, R. G., and R. H. Bourke, 1974: Observations on the coastal current of arctic Alaska. *J. Mar. Res.*, **32**, 195–207.

Peacock, N. R., and S. W. Laxon, 2004: Sea surface height determination in the Arctic Ocean from ERS altimetry. *J. Geophys. Res. C Ocean.*, **109**, 1–14, doi:10.1029/2001JC001026.

Pickart, R. S., L. J. Pratt, D. J. Torres, T. E. Whitledge, A. Y. Proshutinsky, K. Aagaard, T. A. Agnew, G.W.K Moore, and H. J. Dail, 2010: Evolution and dynamics of the flow through Herald Canyon in the western Chukchi Sea. *Deep Sea Res. Part II Top. Stud. Oceanogr.*, **57**, 5–26, doi:10.1016/j.dsr2.2009.08.002.

Pnyushkov, A. V, and I. V Polyakov, 2011: Observations of Tidally Induced Currents over the Continental Slope of the Laptev Sea, Arctic Ocean. *J. Phys. Oceanogr.*, **42**, 78–94, doi:10.1175/JPO-D-11-064.1.

Sakshaug, E., 2004: Primary and Secondary Production in the Arctic Seas BT - The Organic Carbon Cycle in the Arctic Ocean. R. Stein and R.W. MacDonald, Eds., Springer Berlin Heidelberg, Berlin, Heidelberg, 57–81.

Schonberg, S. V, J. T. Clarke, and K. H. Dunton, 2014: Distribution, abundance, biomass and diversity of benthic infauna in the Northeast Chukchi Sea, Alaska: Relation to environmental variables and marine mammals. *Deep Sea Res. Part II Top. Stud. Oceanogr.*, **102**, 144–163, doi:https://doi.org/10.1016/j.dsr2.2013.11.004.

Spall, M. A., 2007: Circulation and water mass transformation in a model of the Chukchi Sea. *J. Geophys. Res.*, **112**, C05025, doi:10.1029/2005JC003364.

Stewart, R. H., and J. W. Joy, 1974: HF radio measurements of surface currents. *Deep Sea Research and Oceanographic Abstracts*, Vol. 21 of, Elsevier, 1039–1049.

Stigebrandt, A., 1984: The North Pacific: A Global-Scale Estuary. *J. Phys. Oceanogr.*, **14**, 464–470, doi:10.1175/1520-0485(1984)014<0464:TNPAGS>2.0.CO;2.

Weingartner, T. J., K. Aagaard, R. Woodgate, S. Danielson, Y. Sasaki, and D. Cavalieri, 2005: Circulation on the north central Chukchi Sea shelf. *Deep Sea Res. Part II Top. Stud. Oceanogr.*, **52**, 3150–3174, doi:10.1016/j.dsr2.2005.10.015.

——, E. Dobbins, S. Danielson, P. Winsor, R. Potter, and H. Statscewich, 2013: Hydrographic variability over the northeastern Chukchi Sea shelf in summer-fall 2008–2010. *Cont. Shelf Res.*, **67**, 5–22, doi:http://dx.doi.org/10.1016/j.csr.2013.03.012.

——, Y.-C. Fang, P. Winsor, E. Dobbins, R. Potter, H. Statscewich, T. Mudge, B. Irving, L. Sousa, and K. Borg, 2017: The summer hydrographic structure of the Hanna Shoal region on the northeastern Chukchi Sea shelf: 2011–2013. *Deep Sea Res. Part II Top. Stud. Oceanogr.*, **144**, 6–20, doi:https://doi.org/10.1016/j.dsr2.2017.08.006.

Winsor, P., and G. Björk, 2000: Polynya activity in the Arctic Ocean from 1958 to 1997. *J. Geophys. Res. Ocean.*, **105**, 8789–8803, doi:10.1029/1999JC900305.

——, and D. C. Chapman, 2004: Pathways of Pacific water across the Chukchi Sea: A numerical model study. *J. Geophys. Res. Ocean.*, **109**, C03002, doi:10.1029/2003JC001962.

Wood, K. R., N. A. Bond, S. L. Danielson, J. E. Overland, S. A. Salo, P. J. Stabeno, and J. Whitefield, 2015: A decade of environmental change in the Pacific Arctic region. *Prog. Oceanogr.*, **136**, 12–31, doi:http://dx.doi.org/10.1016/j.pocean.2015.05.005.

Woodgate, R. A., K. Aagaard, and T. J. Weingartner, 2005: A year in the physical oceanography of the Chukchi Sea: Moored measurements from autumn 1990–1991. *Deep Sea Res. Part II Top. Stud. Oceanogr.*, **52**, 3116–3149, doi:10.1016/j.dsr2.2005.10.016.

Woodgate, R. A., T. J. Weingartner, and R. Lindsay, 2012: Observed increases in Bering Strait oceanic fluxes from the Pacific to the Arctic from 2001 to 2011 and their impacts on the Arctic Ocean water column. *Geophys. Res. Lett.*, **39**, doi:10.1029/2012GL054092.